Kinetic Studies of Non-equilibrium Plasma-assisted Ignition and Combustion

A Thesis

Submitted to the Faculty

of

Drexel University

by

Liang Wu

in partial fulfillment of the degree

of

Doctor of Philosophy

August 2013

Dedication

To my family

Acknowledgements

Throughout my study, research and live at Drexel University, I am grateful to every individual who offered help.

First and foremost, I would like to express my greatest gratitude to my advisors Prof. Alexander Fridman, Prof. Nicholas P. Cernansky and Prof. David L. Miller for providing such a free and dreamed research environment. Their continuous motivation, guidance and support have been invaluable in the success of this study. I would like to convey my deepest appreciation to Dr. Andrey Starikovskiy, with whom I had pleasure to work with on all these projects. I feel thankful for his patience, guidance and detailed explanations for almost every question I asked. I am always amazed at the depth and breadth of his expertise in this area. I would like to extend my gratitude to my thesis committee members, Dr. Alexander Rabinovich and Dr. Gary Friedman, for their time and valuable advice during the process of assembling my dissertation. I would also like to thank Dr. Alan C.W. Lau for his counsel and encouragement throughout my graduate studies.

I would like to extend my sincere appreciation to my friends and colleagues, Jamie Lane and Mike Stichter, in the laser diagnostics lab for their help. I would also like thank Anatoliy Polevich and Gary Nirenberg in Drexel Plasma Institute for their expertise and support. I would like to acknowledge my other friends from both Hess Lab and Drexel Plasma Institute, including: Kirill Gutsol, Mike Gallagher, Yong Yang, Hyoungsup Kim, Tom Nunnally, Julius Corrubia and Farinaz Farid. Also, I would like to

recognize the knowledgeable staff of the Drexel Machine Shop, including Mark Shiber and Paul Velez.

Most of all, I would like to thank my parents and my wife. Without their love, support, encouragement and understanding over these years, this doctoral thesis would not have been possible.

Finally, my work was supported by the National Science Foundation (CBET-0755632) and U.S. Air Force Office of Scientific Research (FA9550-09-1-0602). Their funding for this research and my studies is greatly appreciated.

Table of Contents

List of Tables

List of Figures

Abstract

Kinetic Studies of Non-Equilibirum Plasma-assisted Ignition and Combustion

Liang Wu

Dr. Alexander Fridman, Dr. Nicholas P. Cernansky and Dr. David. L. Miller

The application of thermal plasmas in combustion has a long history which dates back at least as far as the early spark ignition engines for automobile applications. In recent decades, a great amount of experimental data has demonstrated promising results for non-thermal plasma application in high speed flow and automotive engines. However, the mechanisms of plasma assisted combustion still remain unclear.

The first part of this thesis presents a computational study in understanding the physics and chemistry of plasma-assisted combustion at temperatures above the auto-ignition threshold. The energy costs in generation of chemically active species by different discharges were calculated. The optimal physical parameters were determined in terms of the energy efficiency. The role of singlet oxygen molecules was numerically studied in promoting ignition of a hydrogen-oxygen mixture. The major reaction pathways have been identified.

The second portion of this study, which is the major emphasis of this thesis, shifted the research focus to the investigation of plasma chemical kinetics at temperatures below auto-ignition threshold. An experimental installation was designed, fabricated and calibrated for this purpose. Three types of laser-based optical diagnostics were applied to

investigate the hydroxyl (OH) radical dynamics in the afterglow of a pulsed nanosecond discharge. Experiments were carried out using a premixed lean fuel-air mixture (φ=0.1) at atmospheric pressure for temperatures ranging from 300 K to 800 K (below the auto-ignition threshold). The fuels were methane, ethane, propane, butane, hydrogen and hydrogen-carbon monoxide. The nanosecond pulsed discharge was formed in a pin to pin electrode system. During the discharge, atomic oxygen and hydrogen are generated by direct electron impact and dissociative quenching of excited nitrogen. The results from laser induced fluorescence (LIF) have shown that after generation by the plasma the OH persists at significant levels for a long time that lengthens with increasing temperature. The ~100 μs-long plateau clearly indicates the existence of chain reactions at low temperature (starting at 500 K for alkanes mixtures, 400 K for hydrogen mixtures), which are not predicted in current kinetic models.

The results from the planar laser-induced fluorescence (PLIF) study have confirmed the unique phenomena and also demonstrated uniform OH radical distribution along the discharge channel. Comparison of OH radical emission dynamics with discharge emission dynamics from excited nitrogen revealed a close similarity in spatial distribution and allowed clarification of the mechanisms of atomic oxygen formation. The third laser diagnostics, Cavity Ring-Down Spectroscopy (CRDS), which is an absorption spectroscopy, demonstrated consistent results and further validated the unpredicted results.

The temperature measurements through Optical Emission Spectroscopy (OES) of the second positive nitrogen system revealed no significant heating by the plasma. Further

studies were focused on identifying the key reaction pathways to reveal the chemical mechanism of the unpredicted phenomena. The roles of nitric oxide and vibrationally excited nitrogen have been experimentally studied. The results have ruled out the possibility of nitric oxide as the key species and have provided support suggesting that vibrationally excited nitrogen could play a major role in the observed OH plateau effect.

Chapter 1 Introduction

The term “plasma” is traditionally associated with blood, where it stands for the liquid component in which blood cells are suspended. It was not until 1928 that Irving Langmuir named ionized gas as plasma, where he compared the suspended blood cells to free electrons and ions in a plasma discharge [1-3]. It is formed by adding energy to a gas (typically electrically), which separates electrons from neutral gas molecules and atoms. Plasma consists of charged particles including free electrons, as well as negative and positive ions, which respond to applied electric and magnetic fields. Plasma is a distinct state of matter containing a significant number of electrically charged particles that affect its electrical properties and behavior. In physics, plasma is often termed the “fourth state of matter”, the other three being solid, liquid, and gas.

The interactions between the charged particles and the neutral particles are important in determining the behavior and usefulness of the plasma. The type of atoms in plasma, the ratio of ionized to neutral particles and the particle energies all result in a broad spectrum of plasma types, characteristics and behaviors. These unique behaviors cause plasmas to be useful in a large and growing number of applications important to our lives and to the world around us.

Plasma discharges come in two main varieties, thermal and non-thermal [2-3]. Thermal kinds are typically equilibrium systems with temperatures in excess of 10,000K. Non-thermal types, in contrast, are in a thermodynamic and chemical non-equilibrium with the

temperature of the electrons (>10,000K) greatly in excess of the gas translational temperature (<< 10,000 K, can be as low as 300K).

Non-equilibrium plasmas at atmospheric pressure are the focus of this research. Their non-equilibrium nature allows for the creation of active species without generating excessive heat, which can potentially promote reactivity at low temperatures which may allow complete combustion at lower peak temperatures (lowering certain emissions). Also, the use of non-equilibrium plasmas seems to give a unique opportunity to guide the energy input into a gas. Non-thermal plasmas thus find many potential applications in automobile and aircraft engine industry. However, in order to fully utilize this technology, there are two key questions that need to be answered: (i) what kind of discharge is proper to provide high effectiveness of ignition and combustion; and (ii) if there are any new or unique kinetic mechanisms responsible for plasma-assisted ignition (PAI)/ plasma-assisted combustion (PAC). Answering these questions requires efforts involving both numerical modeling and experiments [4-5].

1.1 Plasma Discharges

Plasma discharges exist in a wide range of conditions, and their particular properties depend on a variety of parameters including pressure, temperature, and gas number density. These temperatures can vary from room temperature to the temperature of the fusion reactor within stars, such as the sun. As a result, plasma discharges can exist both naturally and can be created in the laboratory (Figure 1.1) [6].

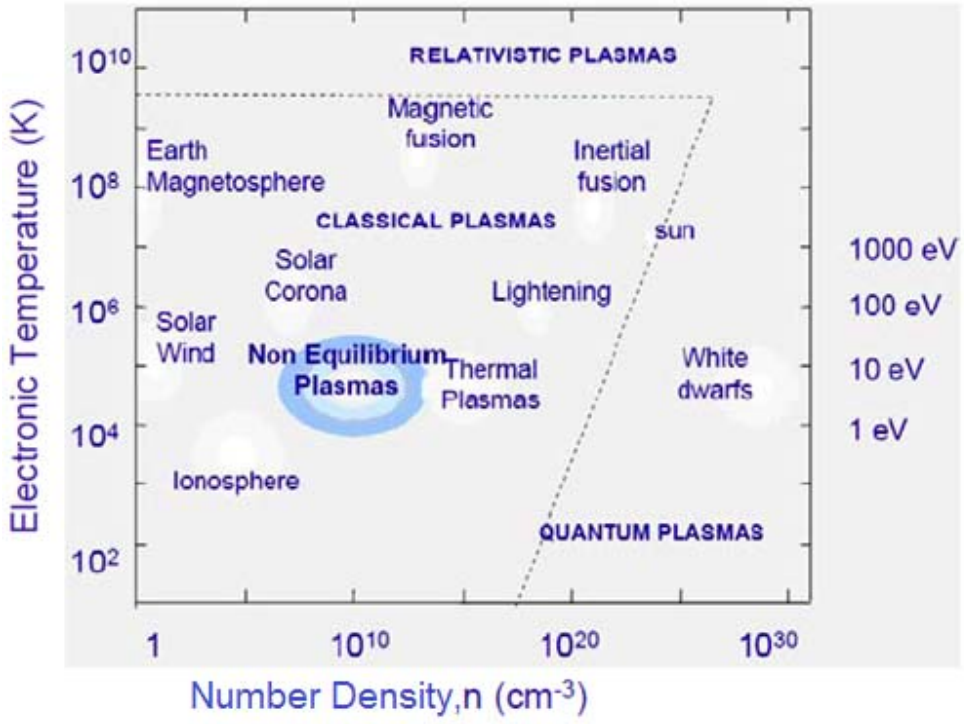

Figure 1.1 Density-temperature plasma diagram. The x-axis is the gas number density, *n*, and the y-axis is the electron temperature [6].

1.1.1 Plasma in Nature

Nature provides many examples of plasma. Although very weakly ionized, the air around us is an ionized gas. In addition, solar plasma, the sun, provides humans with light and heat that are necessary to survive. Undoubtedly, these two examples indicate the important role that plasma plays in our lives.

Some other examples of naturally occurring plasmas are the solar corona, solar wind, and the earth's ionosphere. Certainly, the most well-known naturally occurring plasma is lightning. In the case of lightning, a thundercloud forms over the ground, and an electric

charge equal to but opposite the charge of the thundercloud is induced in the ground below. Then, a path of ionized air forms in a negatively charged region in the thundercloud. When ionized air approaches the ground, the presence of opposite charges increases the electric field. Once the electric field is sufficiently strong, a conductive discharge develops. Once a complete path or channel of ionized air is established between the cloud and ground, a greater amount of current can propagate from the Earth back up the into the cloud. This is the "return stroke," and it is the most luminous and noticeable part of the discharge.

1.1.2 Plasma in the Laboratory

Due to the great variety of parameters that can influence plasma properties, manmade plasmas have become the main topic of interest in universities and industry. The traditional way to create a plasma discharge is to establish a voltage between two electrodes (called the breakdown voltage, V_b). This magnitude of V_b is dependent primarily upon the factors, pressure p and distance d between the electrodes. The dependence of V_b on pd varies depending upon the gas that is present. These dependences have been studied in detail and are summarized via Paschen curves (Figure 1.2) [1].

The simplest way to create a discharge is using two metal electrodes. Once the breakdown voltage is applied, the particular discharge that is created will depend upon voltage V and current I values. Generally, if current values greater than 10 Amperes (A) are used, a thermal arc will be generated. Thermal arcs were first studied in the early 1800's by Humphry Davy, and received their name because the very hot plasma discharge appeared arc shaped because of buoyant forces.

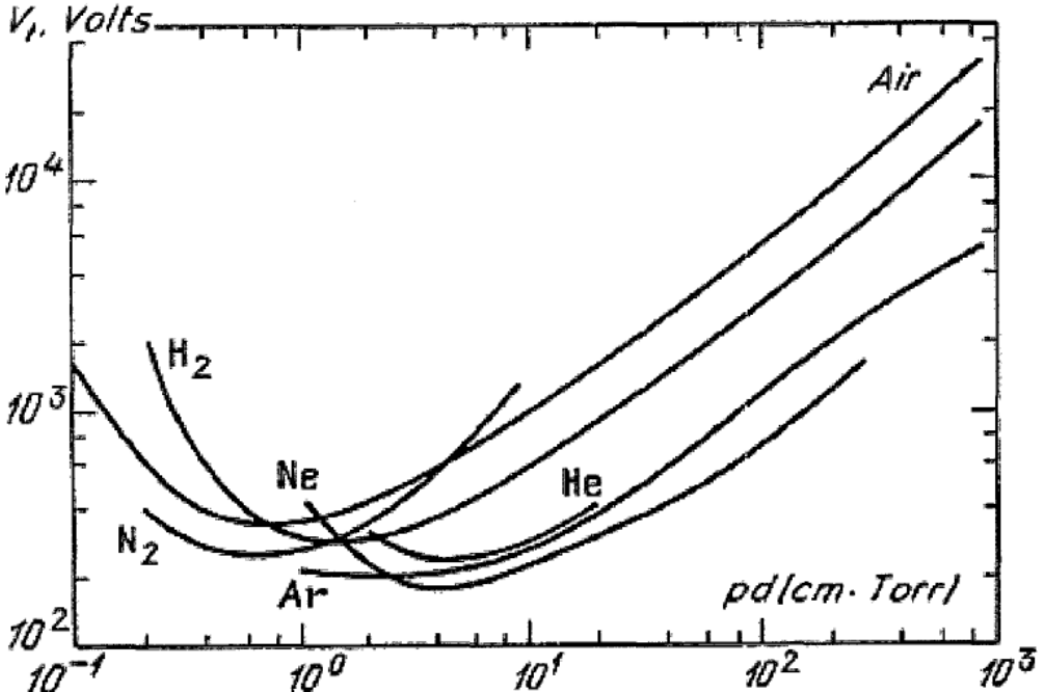

Figure 1.2 Breakdown potentials in various gases over a wide range of *pd* values [1].

Varying *V* and *I* values will result in changes in discharge properties. In general, lowering current will gradually reduce the thermal properties of the discharge. Power input (and hence cost) will be reduced; however, the usefulness of the discharge for particular applications will change. For instance, thermal arcs are very effective for welding and melting, but when current is decreased to a few Amperes, the ability to melt quickly for welding is greatly reduced. Different names were given to the different regimes of plasma discharges, and these regimes and some discharge types are summarized in Figure 1.3 [7].

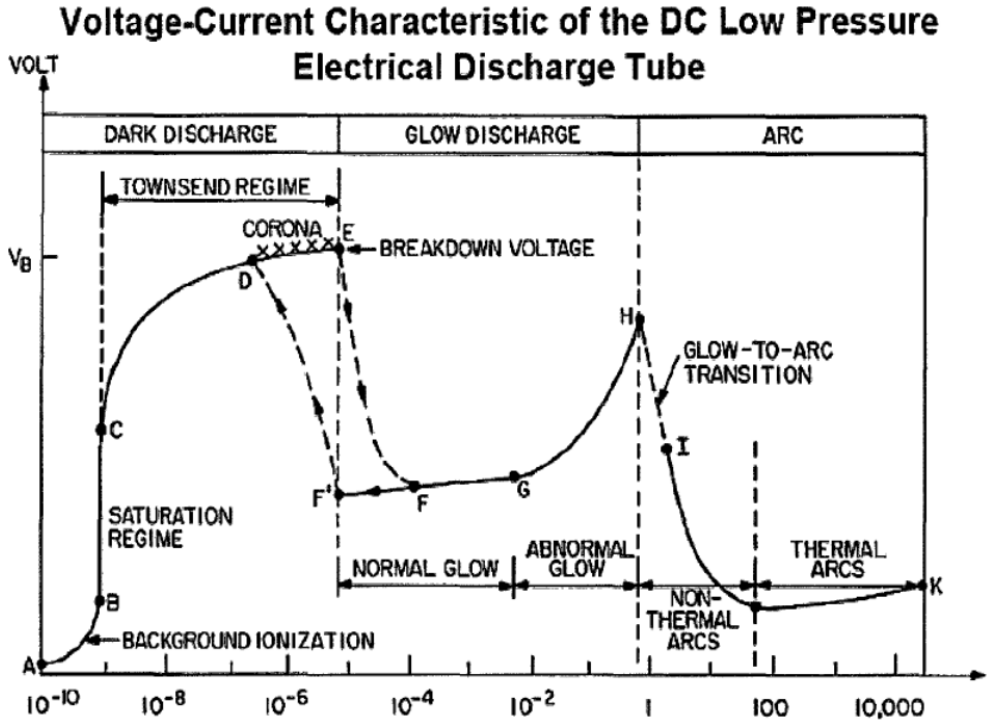

Figure 1.3 Voltage-current characteristics of DC low pressure electrical discharge tube [7].

1.2 Plasma Discharge Temperature

Before detailing specific types of plasma discharges, the terminology of "plasma temperature" needs to be developed. Generally, plasma is separated into two main temperature regimes, non-thermal and thermal. Plasma gas temperature is largely dependent upon average energies of plasma particles and their degrees of freedom (translational, rotational, vibrational, and electronic). Such energies are achieved via electron collisions and electron collisions with heavy particles, which result in ionization of the heavy particles. Depending on the frequency of collisions, the energy (and hence

temperature) of plasma components (electrons and heavy particles) can be different. As a result, the plasma can exist in non-equilibrium. Regardless of whether plasma is non-equilibrium or quasi-equilibrium, the temperature required for chemical processes is typically 10% of the total energy for ionization, which is also the Arrhenius activation energy.

1.2.1 Non-Thermal Plasma

Many types of plasma are characterized by multiple different temperatures in different plasma particles, and some, which will be mentioned later in this study, will be more fully described in the next section. In general, this temperature difference is greatest between electron temperature (T_e) and heavy particle temperature (T_o). Electron temperature often exceeds heavy particle temperature. In this case, ionization and chemistry are mainly determined by electron temperature, and strongly thermal processes will not exist. This type of non-equilibrium plasma is termed non-thermal plasma.

When thinking in terms of degrees of freedom and particle energy levels, non-thermal plasma is often characterized as $T_e > T_v > T_r \cong T_i \cong T_o$. Electron temperature is highest (usually 10,000 K or 1 eV), followed by the temperature of vibrational excitation. In general, rotational excitation temperature, ion temperature, and heavy particle are all quite low (room temperature). High energy electrons produced in non-thermal plasma lead to the formation of active chemical species and radicals, such as atomic oxygen (O) and hydroxyl (OH), and electronically excited oxygen ($O_2(a^1\Delta_g)$). Plasma-generated radicals and ions are available to participate in chain reactions that may promote or

accelerate reaction pathways. As a result, non-thermal plasma can induce chemical reactions, even though the overall gas temperature is low.

In order to create a non-thermal system with these properties, low pressure, low power, or pulsing is usually required. Some examples of non-thermal plasma are glow discharge and corona discharge.

1.2.2 Thermal Plasma

In the case that the temperature of electrons is nearly equal to the temperature of heavy particles, plasma will fulfill the basic requirements for local thermodynamic equilibrium. As a result, the discharge will follow the laws of equilibrium thermodynamics and can be characterized by a single temperature at each point of space. In such a plasma discharge, ionization and chemistry are determined by temperature. The plasma discharge is considered to be quasi-equilibrium and is termed thermal plasma.

Thermal plasma is often characterized by $T_e \cong T_v \cong T_r \cong T_i \cong T_o$. The temperature of all energy modes and components are nearly equal. Thermal plasmas are usually constant, high power, high pressure (equal or larger than 1 atmosphere) discharges. The joule heating effect is responsible for high gas temperatures in thermal plasmas where power is initially transferred from the electric field to electrons and then to the background neutral gas species by way of a large number of electron-neutral collisions [3]. In thermal plasmas, energy is used to heat the entire gas, and temperatures often range from 10,000-100,000K (10-100 electron volts (eV)). Some examples of thermal plasma are arc discharge and spark discharge.

1.3 Examples of Electrical Discharges

There are a number of thermal and non-thermal plasma discharges that have been used for combustion applications. Historically, the most common thermal plasma used for these applications is the spark discharge. Other, less common, discharges have been tested, and two such examples are radio frequency inductively coupled plasma (RF ICP) and thermal microwave plasma. In addition, many types of non-thermal plasma have been investigated for plasma-assisted combustion. Most researchers have focused on using nanosecond pulsed discharge, dielectric barrier discharge (DBD), glow discharge, microwave discharge and corona discharge. In the section that follows, a brief introduction of each type of discharge mentioned herein will be provided to highlight its properties.

1.3.1 Arc Discharge

An atmospheric pressure arc is the most typical and widespread example of dense equilibrium plasma supported by an electric field. This kind of discharge is characterized by high-current (30A - 30kA), low-voltage (10 - 100V), and very high gas temperatures (10,000 - 100,000 K or 10- 100 eV). The high gas temperature is due to the high degree of joule heating from the discharge current. Their initial high temperature also contributes to sustaining high current by influencing the mechanism by which electrons are supplied to the discharge, namely the thermionic and field emission mechanism. Thermionic emission is electron emission from a high temperature metal surface due to the high thermal energy of electrons in the metal. For this process to occur, a combination of high metal surface temperature must be coupled with sufficient external electric field in the

cathode vicinity. This permits a large number of electrons to escape the metal surface and provides a high flux of current into the discharge [1].

1.3.2 Spark Discharge

The spark discharge, widely used for ignition in automobile engines, occurs when the high voltage is applied to a discharge gap which is typically a few millimeters in length. Lightning is the typical example in nature: it may be several kilometers in length and is the electrical breakdown between a cloud and the ground, or between two clouds. A spark created in laboratory is just "miniature lightning", which is usually accompanied with a characteristic cracking sound, just as lightning produces thunder. The sound is caused by a shock wave. It is generated by a sharp rise in pressure due to an intensive release of Joule heat in the spark channel when a high discharge current passes through it.

The spark discharge is a multifaceted and complicated phenomenon. Its initial stage (1–10 ns at atmospheric pressure) is the process of the streamer breakdown[*]. After the conducting channel has been formed, the discharge occurs. The capacitor is discharged with the charge being transferred by the large current which flows across the gap that closes the circuit.

[*] In higher electric fields, the electrons gain more energy between collisions, and are more likely to ionize the neutrals. At the breakdown field, there is a balance between the production of new electrons (due to impact ionization) and the loss of electrons (due to attachment). Above the breakdown field, the number of electrons starts to grow exponentially, and an electron avalanche forms. The electron avalanches leave behind positive ions, so in time more and more space charge is building up. (Of course, the ions move away in time, but this is a relatively slow process compared to the avalanche generation). Eventually, the electric field from all the space charge becomes comparable to the background electric field. This is sometimes referred to as the avalanche to streamer transition. In some regions the total electric field will be smaller than before, but in other regions it will get larger, which is called electric field enhancement. New avalanches predominantly grow in the high field regions, so a self-propagating structure can emerge: a streamer.

1.3.3 Corona Discharge

The corona discharge is a very well known, man-made and naturally (St. Elmo's Fire - a haunting phenomenon highlighted in the movie Moby Dick) occurring plasma discharge. It can be described as a weakly luminous, non-uniform discharge, which appears at atmospheric pressure near sharp points, edges, and along thin wires. Strong electric field and ionization along with some luminosity are located near one electrode. The charged particles are then carried by weak electric fields from one electrode to another. Corona discharges can be both positive and negative.

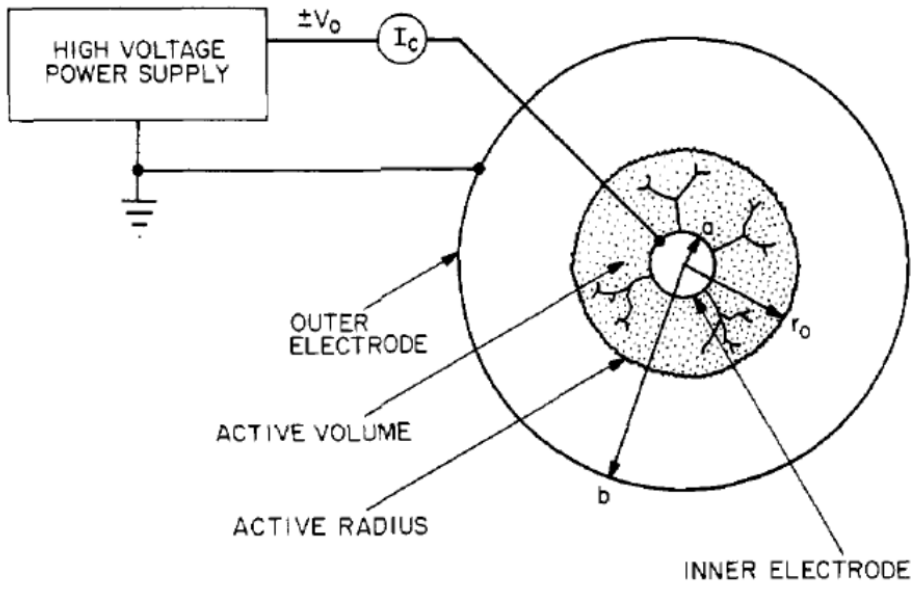

Figure 1.4 Schematic of corona discharge generated by a fine wire [7].

Another form of corona discharge is the pulsed corona discharge. Continuous corona discharges are limited to low current and power, which is conducive for application to materials and gas stream processing (environmental and fuel conversion applications included). It is possible to increase power in a corona discharge (without transition to the spark regime) by using pulse-periodic voltage. Pulsed corona can be relatively powerful (10 kW) and luminous.

1.3.4 Glow Discharge

The glow discharge is the most well-known type of non-thermal plasma and has been widely used for over 100 years. It can be described as a self-sustained continuous DC discharge with a cold cathode, which emits electrons as a result of secondary emission. Glow discharge has distinct features such as: a cathode layer (a positive charge space with strong electric field), the positive column (a quasi-neutral plasma with low electric field located between the cathode and anode), and the anode layer (a negative charge space with slightly elevated electric field). The operation of the modern fluorescent lamp is an example of this behavior. A normal glow discharge operates in a current regime of 10^{-4} - 0.1 A. Any increase in current above this regime will result in a transition to an abnormal glow discharge. Increasing current further (1 A) will result in a transition to an arc discharge.

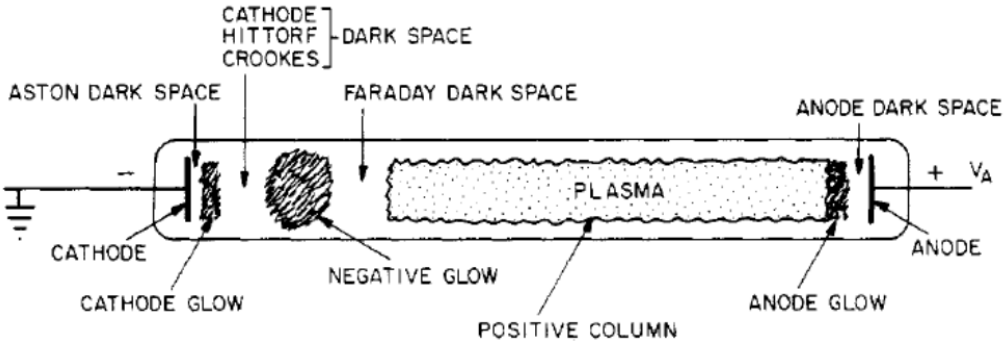

Figure 1.5 A schematic drawing of the visible regions of the normal glow discharge [7].

1.3.5 Dielectric Barrier Discharge

The principle idea of dielectric barrier discharge (DBD) is to limit the formation of sparks and current growth by placing a dielectric barrier in the discharge gap. Sometimes it is referred to as either a silent discharge, since it operates noiselessly, or a corona discharge with dielectric according to the physics of the process.

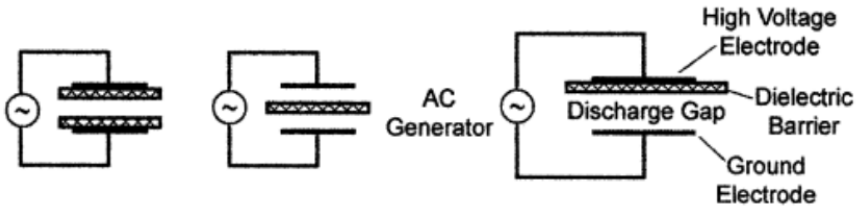

Figure 1.6 A schematic drawing of the typical setup of the dielectric barrier discharge [3].

The DBD configuration was first reported in 1857 by Siemens for the purpose of "ozonizing" air [8]. The process of ozone production by DBD has been studied in detail and has been widely applied in industry [9]. They are stable high pressure gas discharges capable of producing large densities of radical atomic and molecular species. The barrier discharges are suitable for a wide range of applications, including surface treatment, pollution control, sterilization, UV and VUV light sources for pumping lasers.

As a rule, this discharge is generated in either a plane-to-plane or a coaxial geometry. The gap between electrodes is no larger than a few millimeters. An alternating voltage (hundreds of Hz to several kHz) is applied to the electrodes. When the applied voltage exceeds the breakdown value, electron avalanches occur, resulting in a “forest” of microdischarges forming conductive channels between the plates. Charge build-up on the dielectric during the current pulse reduces the net voltage across the gap. Eventually, the electric field in the plasma is unable to sustain the microdischarges, and the plasma at that location is extinguished. The area density of the randomly distributed microdischarges is sufficiently large that on the average, the entire gas is processed.

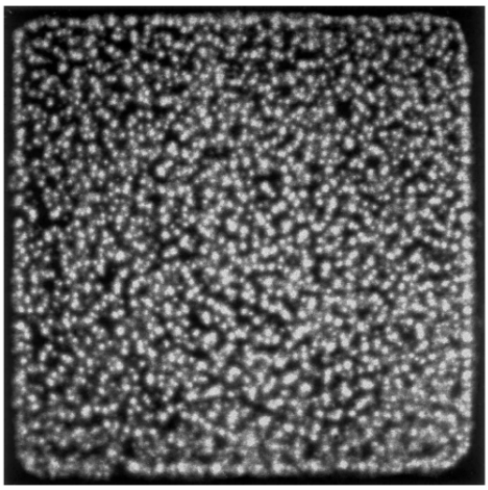

Figure 1.7 End-on view of microdischarges [9].

1.3.6 Microwave Discharge

Microwave discharges have the great advantage of being capable of operation without electrodes. Instead of utilizing a potential difference between electrodes, a microwave discharge is sustained by a high frequency electromagnetic field. Operation without electrodes is often preferred for high temperature applications because it can eliminate the need for complicated electrode cooling.

Initiating high frequency plasmas, however, is more challenging than traditional DC plasmas because creation of the microwave requires more complex, expensive power supplies along with additional components such as a frequency generator (magnetron head), a circulator, a tuner, a directional coupler, and a waveguide. In addition, the plasma must be coupled as a load in a power circuit. In general, this coupling is

accomplished via waveguides, where a quartz tube is inserted into the waveguide. The plasma is ignited and confined to the quartz tube.

Microwave discharges can exist as both thermal and non-thermal discharges. Thermal microwave plasma discharges operate at atmospheric pressure, while non-thermal microwave operates at low pressure. The thermal properties of microwave plasma will generally increase as pressure is increased.

1.3.7 Radio Frequency (RF) Discharge

Radio frequency (RF) discharges share many similar properties with microwave discharges. RF discharges operate without electrodes (only in the 0.1 to 100 MHz region) and can exist in both thermal and non-thermal regimes (again, pressure dependent). Thermal plasma generation is provided via inductively coupled plasma (ICP) at atmospheric pressure. In this case, high frequency current passes through a solenoid coil, providing a magnetic field (primary). This allows for the formation of a vortex electric field, which sustains the RF ICP discharge. Again, expensive power supplies and additional components are required, and the plasma should be coupled as a load with an RF generator. Effectiveness of coupling the electromagnetic field to the plasma discharge is crucial because the plasma is sustained by the energy absorbed by the field. Poor coupling will result in low efficiency of the power supply.

At low pressures, RF plasma can exists in a strongly non-equilibrium regime. In this regime, the capacitively coupled plasma (CCP) can be utilized. RF CCP operates with

higher electric fields (primary). As a result, RF CCP discharges are more non-thermal than ICP and can generate non-thermal plasma at moderate to high pressures.

1.3.8 Nanosecond Pulsed Discharge

A pulsed uniform nanosecond gas discharge was first observed more than 100 years ago in 1893 by Thomson 0. There exist two kinds of discharges when a high voltage short duration pulse is applied to a gas at atmospheric pressure and ambient temperature. That is either a non-equilibrium streamer discharge for short pulse duration (units and tens of ns) or an equilibrium pulsed arc for longer pulses (tens and hundreds of ns).

Initiation of the discharge with an abrupt increase of voltage (about 1 $kV \cdot ns^{-1}$) at moderate gas densities is of great interest. Modern high voltage generators characterized by pulse amplitudes of tens and hundreds of kilovolts, voltage rise time in ns, pulse duration of tens of ns and repetitive frequency up to tens of kHz make it possible to create a spatially uniform discharge [4].

The use of nanosecond pulsed discharges has formed the basis for several recent studies of oxygen-containing plasmas for Plasma Assisted Combustion (PAC) [4-5], Electric Discharge Chemical Oxygen Iodine Laser (E-COIL or DOIL) development [11, 12], and MHD supersonic flow control [1, 13].

1.4 Plasma-assisted Combustion

The development of the world's industry has been driven by the combustion of fossil fuels over the past century. Today in U.S., the consumption rate of petroleum is 19.6

million barrels each day. Moreover, the combustion of fossil fuels results in air pollution, for example, nitrogen oxides (NO_x). Recently, there has been increasing interest in plasma assisted combustion (PAC) as a way to potentially improve the efficiency of high speed (for example, supersonic) combustion systems, as well as to reduce the production of pollutants in gas turbines and reciprocating SI and CI engines.

Recent studies report that PAC may produce volumetric ignition, reduce ignition delay time, improve flame stability and expand flammability limit of mixtures [4]. Low temperature PAC provides combustion researchers the capability of initiating combustion in high speed flows [14], and of stimulating combustion with fuel lean mixtures [15], to name a few advantages. With increasing interest in pollution control, these advantages are also attractive for low emission combustion systems such as lean burn engines which may reduce harmful NO_x emissions as well as fuel consumption.

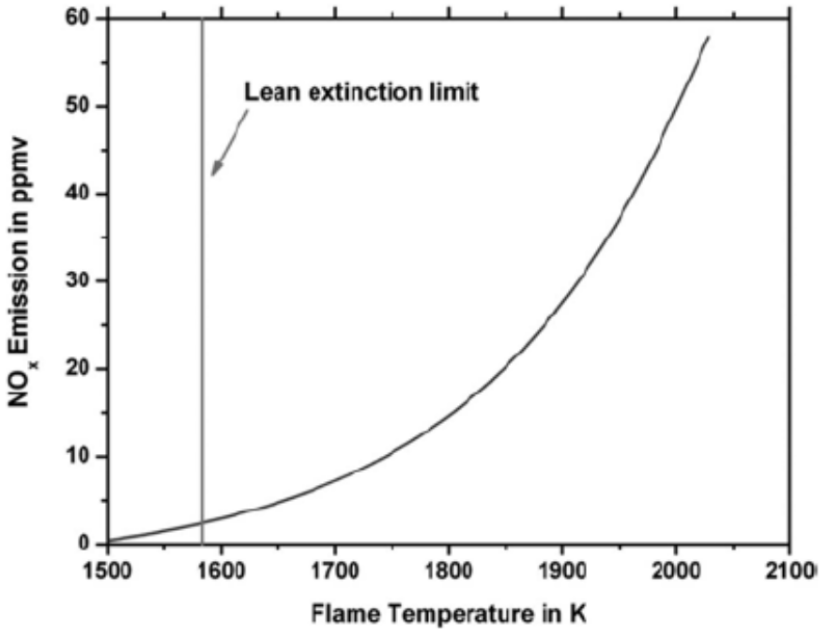

Figure 1.8 NO_x emission as a function of the flame temperature [6].

1.4.1 Plasma-assisted Flame Stabilization

Reducing NO_x emissions from combustion systems is a major challenge. One approach has been to operate at lean mixtures in order to reduce flame temperature, which in turn, reduces the production of NO_x (Figure 1.8). However, lean burning can lead to serious combustion instabilities, which can result in flame extinction [16]. Various stabilization methods have been implemented for both diffusion and premixed flames. These include pilot flames, recirculation flow via bluff bodies, swirl, electric fields, and plasmas.

The first technique concerns the use of a rich pilot flame to reattach the combustion process. To attach a hydrocarbon flame to a burner lip, Han and Mungal [17], Muñiz and

Mungal [18] and Carter et al. [19] used a hydrogen pilot flame in a coflow jet diffusion flame. Moreover, Prakash et al. [20] increased premixed flame stability by controlling the flow rate split between a bypass line and the main fuel line. Tachibana et al. [21] investigated the effect of secondary fuel injection location on premixed combustion instability. Typical examples of bluff body and swirl stabilization can be found in [22-24]. However, these methods have an intrinsic limit in that the main energy transfer occurs predominantly in the form of thermal energy, which implies that a portion of energy is lost. Moreover, this technique significantly increases the level of NO_x generated.

Flame stability can be obtained by controlling flow convection in the flame reaction zone with electric fields. The stabilization effect is caused by an "ionic wind" between the applied electric field and the "chem-ionized" species in the flame reaction zone. In particular, Calcote [25] and Calcote and Berman [26] observed flame deflection and blowout limit extension of a Bunsen burner exposed to a DC electric field. The blowout limit of a premixed methane/air flame is then increased by a factor of 4. More marginal in comparison to studies with DC fields, investigations of blowout limit and burning velocity under alternating current (AC) were also reported in [27-30].

Details of the interaction between flames and plasma discharges are reviewed in Reference [31-33]. Within these papers, plasma jets are used to increase flame speed and expand the flammability limit of premixed flames.

Finally, an alternative possibility is the use of an electric discharge (in the form of an arc [16]) to reattach a flame and to reduce the production of NO_x.

Recent activity to investigate novel flame stabilization approaches has included the use of non-equilibrium discharges for combustion enhancement (extended flammability limits and reduced ignition delay times), such as dielectric barrier discharges (DBDs) and nanosecond pulsed discharges for premixed flames [34-46]. In this case, the typical added energy is 0.1-1% compared to that of typical hydrogen pilot flames. Corresponding studies on the stability of diffusion flames are relatively rare. Kim et al. [47] found that a co-flow lifted methane jet flame is stable under application of a nanosecond pulsed discharge in co-flow velocities of up to 20 times the laminar flame speed. They also determined the optimal discharge placement in a methane jet in cross flow [48].

Furthermore, the use of pulsed and continuous plasma jets for the ignition of a lean mixture and the stabilization of the flame in a supersonic flow is promising. An example of such an application is the flame stabilization in a gas turbine under conditions which tend to extinguish the flame. Another application relates to the ignition in diesel engines in extremely cold climates: a small plasma jet was used. In the study of Warris and Weinberg [49], pulsed and continuous plasma jets were used to stabilize fast (5-30 m/s) lean propane/air mixture flames. The results clearly show a large extension of flame stabilization and flame holding in the presence of plasma jets. Moreover, the mixture ignition and the flame holding occur at values well below the lower flammability limits.

Plasma-assisted combustion and stabilization of a turbulent premixed flame using nanosecond repetitively pulsed discharges is studied in [50, 51], respectively. A related study of Galley et al. [36] examined the extension of the flammability of a lean mixture. Moreover, pulsed nanosecond plasma has been shown to stabilize lean premixed

atmospheric pressure propane-air flames [3]. A nanosecond repetitively pulsed plasma generator capable of delivering an electric pulse of 10 kV during 10 ns at a frequency of up to 30 kHz is used to stabilize and improve the efficiency of a 25 kW lean premixed propane/air flame at atmospheric pressure. The plasma significantly extended the region of flame stability, over a much wider range of fuel equivalence ratios and flow rates. This example demonstrated the possibility of increasing the combustion efficiency with the addition of a 75 W discharge (0.3%). Also, the spontaneous emission of OH and CH radicals increases by at least 40% in the presence of the discharge.

With the same goal, but with a different electric discharge, Choi et al. [16] studied the stabilization of lean propane/air premixed flames. Low power arcs and high frequency sparks were used. Low power arcs significantly lowered the lean limits of flammability. The results showed that the lean flammability limit decreases from equivalence ratios of 0.62 to 0.55 at a flow rate of 330 cm^3/s. Similar effects were observed with a spark discharge. In this study, the minimum equivalence ratio dropped from 0.58 to 0.43 (~25% decrease) at a flow rate of 240 cm^3/s. Finally, it is worth noting that similar reductions in the lean limit of combustion were observed at higher flow rates.

Unfortunately most plasmas generate NO_x directly from the air. The decrease combustion generated NO_x through the use of lower equivalence ratios, permitted by the presence of the discharge, may be negated by the NO_x production in the plasma [16]. However, in larger burners, this balance should be in favor of NO_x reduction.

1.4.2 Plasma-assisted Ignition

The influence of non-equilibrium plasma created by a pulsed discharge above the ignition thresholds of a combustible mixture at various pressures and temperatures has been studied by an installation consisting of a discharge cell connected to a shock-tube. It allowed the study of fast homogeneous ignition of supersonic flows. In the study of Bozhenkov et al. [52], the ignition delay time decreases significantly in the case of the simultaneous action of the shock wave and the nanosecond discharge. Moreover, Klimov et al. [53] succeeded in ignition and stable burning of very lean propane/argon (1:9) mixtures in a supersonic air flow. A high frequency streamer discharge and a high frequency torch plasma discharge were used.

References [38, 52, 54] reported the possibility of the acceleration of combustion (characterized by the ignition delay) by application of a nanosecond pulsed barrier discharge to (H_2-air), (CH_4-air) and (C_3H_8-air). The application of a discharge, which develops in the form of a fast ionization wave, in the system (H_2-air), was studied by Starikovskii [54]. In the case of the mixtures with 29.6% of H_2 in air, a significant part of energy was spent for the direct dissociation of O_2 and H_2 by electronic impact, generating a great quantity of O and H atoms. The high degree of dissociation led to a rapid development of ignition. Thus, the induction time until ignition was decreased under the action of the gas discharge. At temperatures of ~2500 K, there was a difference by a factor of 1.5 between a “thermal” and a “non-thermal” ignition. This difference increased in a monotonic way with a temperature decrease. Also, experiments on ignition of non-flowing preheated hydrogen-air and hydrocarbon-air mixtures by a single-pulse fast

ionization wave discharge demonstrated that it can substantially reduce ignition delay time [39]. In addition, the ignition threshold was reduced by 300 K to 500 K with the pulsed discharge (high intensity and contribution of energy < 0.1 J/cm^3).

It is worth noting that the most critical process for high voltage ignition is the production of atomic oxygen and atomic hydrogen, which ensures the evolution of the flame. Auto-ignition of (CH_4-air) mixtures non-diluted at high pressure (P$\leqslant$ 500 atm) was studied by Zhukov et al. [55] using the shock tube technique. The authors showed that in the process of ignition, initiated by the action of a pulsed discharge in CH_4-air at high temperature, its main role concerns the direct dissociation reactions of the gas by electron impact and the dissociative quenching of excited electronic states of N_2 by oxygen. The production of additional “active centers” results from the acceleration of the chemical kinetic process.

An important characteristic of plasma assisted combustion is the proper organization of the energy deposited in the medium. Energy must be provided in the discharge space and be employed for the production of radicals (instead of the ionization of gas or the thermal heating): the “streamer” discharge mode corresponds well to these conditions. Indeed, the active particles are produced at the streamer "discharge head” (which measures typically 0.05 cm for voltages of 10-20 kV).

In addition, Chintala et al. [56] studied experimentally the application of non-equilibrium plasma created by a RF discharge, arc DC and “spark” in flows of CH_4-air, C_2H_4-air and CO-air. For the CH_4-air and C_2H_4-air stoichiometric flows, the flow rates (u) and the studied pressures (P) are: $u \leq 4.3$ m/s, $P \geq 350$ Torr and $u \leq 6.3$ m/s, $P \geq 240$ Torr,

respectively. Results obtained with DC, arc and spark discharges, showed that no ignition is obtained for pressures lower than 300 Torr for the CH_4-air flows and below 200 Torr for C_2H_4-air and this for the same mass flow rate of 1.2 g/s.

Finally, recent experiments of Lou et al. [57] on ignition of premixed hydrocarbon-air flows using transverse RF discharge demonstrate that volume ignition can be produced at plasma temperature significantly lower than the auto-ignition temperature (300 – 400 °C). The propane dissociation by electron impact mechanism is described in Reference [58].

2D images of OH emission under ignition of the propane–air mixture by a sequence of nanosecond pulses were obtained in using an ICCD camera [59]. The authors compared them with the ICCD images for ignition by conventional spark discharge. At the same energy deposited in the discharges (30 mJ) the emission from combustion initiated by the conventional spark is less intense and the flame expansion rate for the conventional spark is slower too.

Mintoussov et al. [35] suggested a model for the influence of radicals. According to their results, the main channels of production of the active particles (O, H, and OH) in the mixtures with air (N_2/O_2) are: the N_2 excitation by electronic impact, which generates the production of molecules in an excited electronic state; the kinetics of the excited states, mainly the N_2^* quenching on O_2 ($N_2^* + O_2$) with the formation of atomic oxygen O; followed by the combustion of this mixture with concentrations of highly non equilibrium radicals and the production of excited radicals (OH^*). Finally, the authors of [60] replaced N_2 by Ar to remove the main channel of formation of active particles: the result is a deceleration of the flame speed.

1.5 Closure

Combustion processes have made great impact in modern life. It is of vital interest to maximize the efficiency of combustion processes and to overcome technical challenges in combustion, especially in high speed flow system (e.g., high speed aircraft). Non-thermal plasma discharges have been demonstrated the possibility and capability to satisfy such needs. Recent progress has been made to understand the mechanisms of plasma enhanced chemical reactions, energy redistribution in plasmas and non-equilibrium initiation of combustion.

There are several possible mechanisms in plasma-assisted combustion. Among them, two types of plasma effects are usually considered of primary importance: 1) local gas heating due to energy release leads to an increase of the chemical reaction rates; 2) excitation, dissociation and ionization of the gas by plasma lead to radical production, and in turn, change the kinetic mechanisms. In order to better apply plasma technology into combustion, it is of great importance to identify the major mechanism, so that we can maximize the utilization of the plasma enhanced chemical effect to increase the combustion efficiency.

1.6 Dissertation Overview

The primary goal of this research was to understand the kinetics of non-thermal plasma assisted fuel ignition and combustion. This work and the organization of this dissertation, is organized into two major parts:

1) A computational study to analyze the physics and chemistry of plasma assisted ignition at temperatures above auto-ignition threshold. Chapter 2 focuses on the physics of non-equilibrium plasma-assisted combustion and Chapter 3 presents associated kinetic studies of non-equilibirum plasma-assisted combustion above the auto-ignition threshold. These numerical studies provided the optimal plasma parameters to efficiently apply plasma in combustion, based on the calculation of energy cost for plasma discharges to produce chemically active species. In addition, the chemical model presented in Chapter 3 facilitated the analysis of the role of singlet oxygen in promoting ignition. The major reaction pathways associated with singlet oxygen were identified.
2) An experimental study of plasma-assisted ignition at temperatures below the auto-ignition threshold. This effort, which represents a major portion of this thesis, is presented in Chapter 4. An experimental facility was built specifically for this study. Three types of laser diagnostics (including laser-induced fluorescence, planar laser-induced fluorescence and cavity ring-down spectroscopy) were applied to measure the OH dynamics in the afterglow of the discharge. The extended OH lifetime at low temperatures was discovered, which was not predicted in any currently available models. Further investigations have

ruled out the plasma caused thermal effect and have provided support for identification of the key species.

Finally, to wrap things up, a brief summary, conclusions and recommendations are presented in Chapter 5.

Chapter 2 Physics of Non-equilibrium Plasma-assisted Combustion[†]

2.1 Introduction

This chapter is devoted to introduce and characterize, from the physics point of view, the non-equilibrium plasma which is applied to the combustion zone or region. To fully utilize plasma technology, it is necessary and important to understand the fundamental physics of plasmas [5].

2.2 Physics of Plasma-assisted Combustion: An Introduction

2.2.1 Energy Branching in Plasma Discharge

The major feature that differentiates plasma-assisted combustion from traditional combustion processes is the creation of a localized region with an extremely non-equilibrium excitation of the combustible mixture. Inside the plasma, the directed energy does not interact with all of the particles but only couples with the electrons and the ions. The neutral atoms essentially do not interact with the electric field while the charged particles are accelerated by it. A flow diagram indicating the flow of the energy in plasma sustained by an electric field is shown in Figure 2.1.

[†] The results presented in this chapter can be found in the paper:
L. Wu, A.A. Fridman, A. Yu. Starikovskiy, "Kinetics of plasma assisted combustion at low reduced electric fields", AIAA-Paper 2010-1593, 48th AIAA Aerospace Sciences Meeting, January 4-7, 2010.

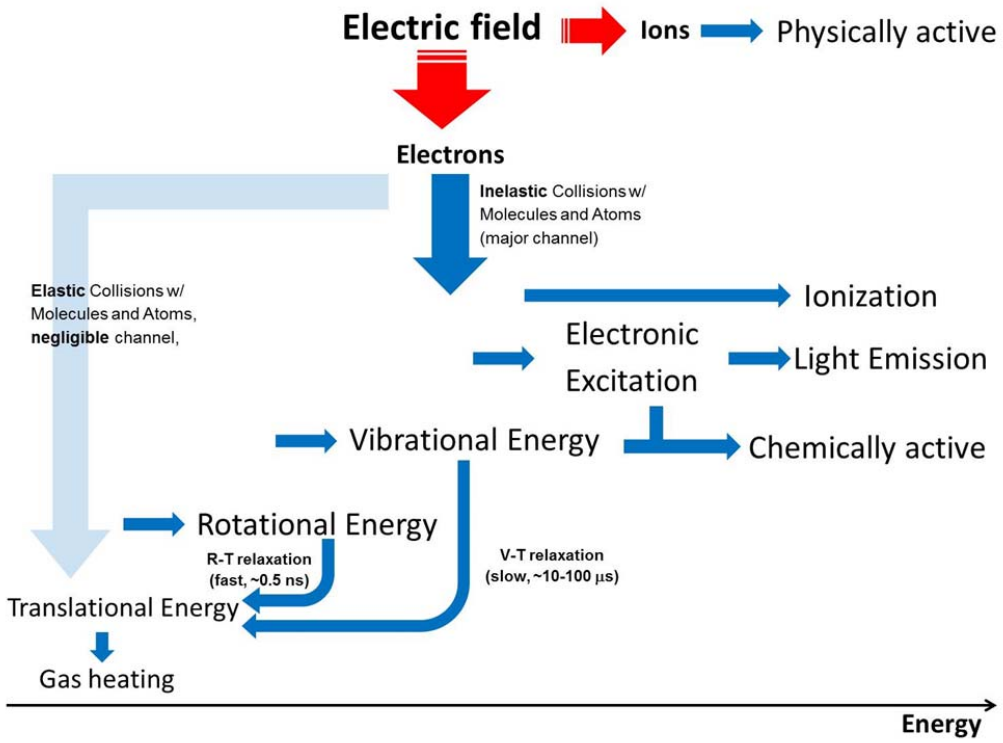

Figure 2.1 Energy Flow Diagram in Non-equilibrium Plasma.

The charged particles gain kinetic energy from the electric field through the Lorentz Force,

$$F = qE \tag{2.1}$$

where F is the Lorentz force on the particle, q is the charge and E is the local electric field. The energy imparted to the particle is given as

$$\varepsilon = \frac{q^2 E^2}{2m} t^2 \tag{2.2}$$

where m is the mass of the particle, t is the time the particle is influenced by the electric field. Considering the great mass difference between electrons and ions

$$m_{ion}/m_e = 5.1 \times 10^4 \tag{2.3}$$

the energy from the external field influences primarily the electrons. The electrons in turn collide with the neutral molecules and atoms. Various type of collisions occur which affect the energy distribution inside the system, including momentum transfer, rotational excitation, vibrational excitation, electronic excitation, ionization, dissociation and attachment. Atoms do not have internal degrees of freedom and so do not experience rotational excitation, vibrational excitation or dissociation. With the great disparity in mass between the electron and the bulk gases, essentially heavy neutral particles, the momentum transfer between them through elastic collisions is very inefficient. Therefore, the majority of electron energy is spent on the excitation of internal energy of molecules. In case the rate of internal energy relaxation process is not high, the population of the excited states of the particles is far from the equilibrium. Overpopulation of excited states leads to an increase in the system reactivity and facilitates ignition and flame propagation. From this point of view, the most important question for plasma-stimulated chemistry is the energy branching rates for different energy modes, rates of relaxation processes and chemically-active system response to this non-equilibrium excitation.

The rate of molecular excitation by electron impact in the discharge depends on the electron energy. The lowest energy is needed to excite the rotational modes of the

molecules. The characteristic energy of rotational modes is only ~10-100 K and electron energy ~300 K (~0.03 eV) is large enough for efficient rotational excitation. The characteristic energy of vibrational modes typically requires 1000 K to 3000 K, which means, for efficient vibrational excitation, the average electron energy should be comparable with or higher than this amount (in air it should be in the range of 0.2-2 eV). Electronic Excitation and molecule dissociation require energies of 3-10 eV. When the average electron energy exceeds 10 eV, ionization becomes one of the dominant electron impact processes. Thus, the possibility to control the electron energy means the capability to control the direction of energy deposition and selective excitation of desired energy modes of molecules.

Average electron energy in gas discharge is determined by a reduced electric field E/n, where E is the electric field and n is the gas number density [1]. Figure 2.2 illustrates the deviation of the characteristic electron energy, D/μ, from the temperature of molecules, T, in different gases [62]. Here, D is the diffusion coefficient of electrons and μ is their mobility. The critical E/n for the noticeable difference between D/μ and T and, consequently, for the formation of a non-equilibrium electron energy distribution is close to E/n ~ 0.1 Td for atomic gases and to E/n ~ 1 Td for molecular gases (1 Td = 10^{-17} V×cm^2).

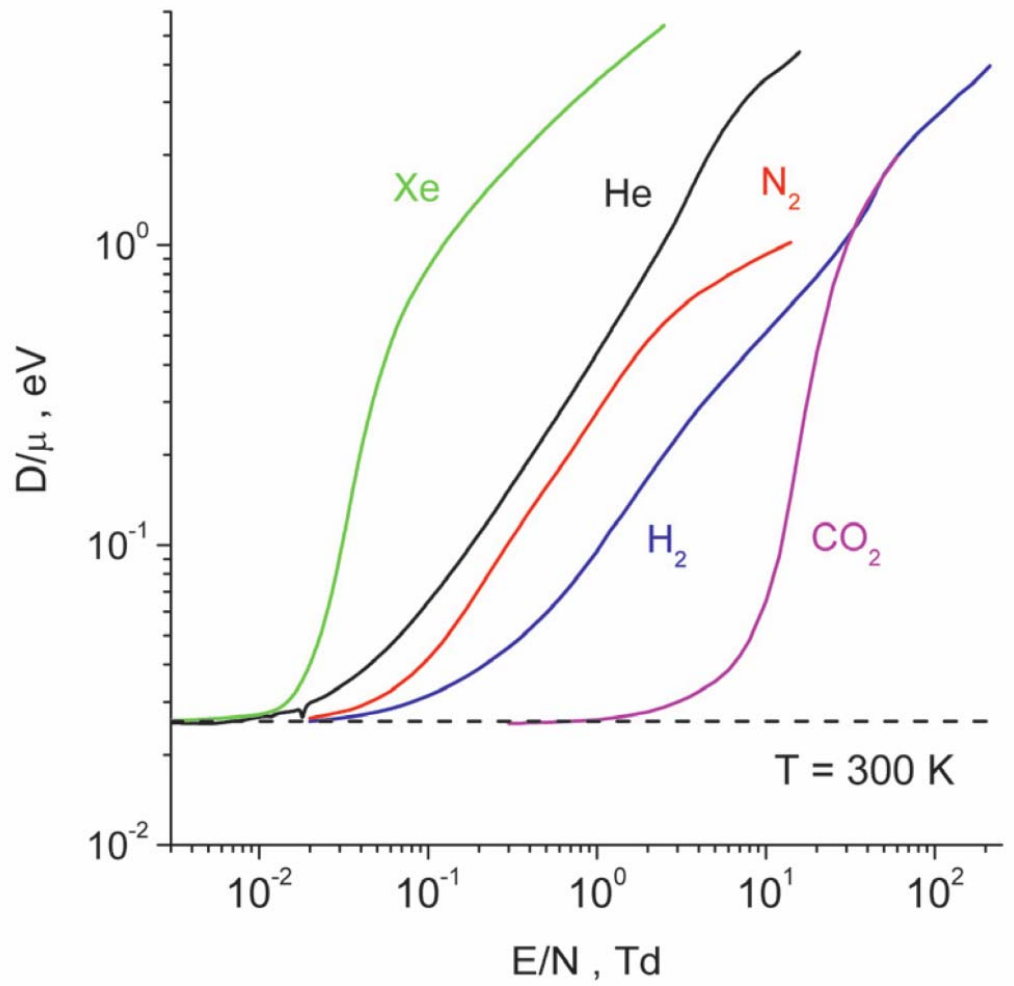

Figure 2.2 Characteristic electron energy. He and Ar [61]; H_2, N_2 and CO_2 [62]

The non-equilibrium electron energy distribution function (EEDF) can be found from a solution of the Boltzmann equation. In the simplest case, the EEDF is time- and space-independent and depends only on the local reduced electrical field, E/n, and gas composition [63]. Further simplification is possible using the so-called two-term approximation in which the EEDF is presented in the form $f(v) = f_0(v) + f_1(v)\cos\theta$

[1], where v is the electron velocity and θ is the angle between the electron velocity and the ambient electric field. The input data for a solution of the electron Boltzmann equation are the cross-sections of elastic and inelastic collisions between electrons and neutral particles. Figure 2.3 shows self-consistent sets of electron cross-sections for CH_4, O_2 and Ar; electron transport and rate coefficients calculated using these data agree well in the pure gases with available measurements.

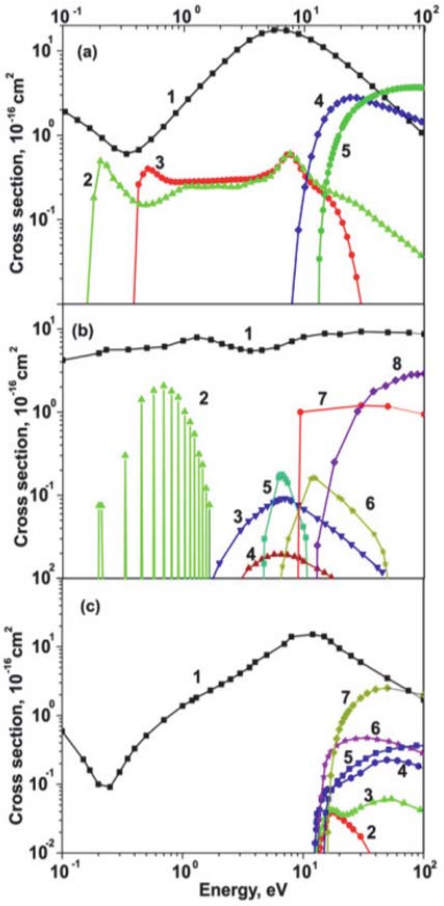

Figure 2.3 Electron collision cross sections for (a) CH_4 [64], (b) O_2 [65], and (c) Ar [66] as a function of electron energy.

CH_4: (1) momentum transfer in elastic collisions, (2)–(3) vibrational excitation,

(4) electronic excitation, and (5) ionization.

O_2: (1) momentum transfer in elastic collisions, (2) vibrational excitation, (3) excitation of the $a^1\Delta_g$ electronic state, (4) excitation of the $b^1\Sigma_g^+$ electronic state, (5) excitation of the electronic states with $\Delta E = 4.5$ eV, (6) excitation of the electronic state with $\Delta E = 6$ eV,

(7) excitation of the electronic state with $\Delta E = 8.4$ eV, and (8) ionization.

Ar: (1) momentum transfer in elastic collisions, (2) excitation of the $^1s_5$ electronic state,

(3) excitation of the $^1s_4$ electronic state, (4) excitation of the $^1s_2$ electronic state,

(5) excitation of other allowed electronic states, (6) excitation of other forbidden electronic states, and (7) ionization.

Using the EEDF, it is possible to calculate the energy branching ratios for the different degrees of freedom of neutral particles. Figure 2.4 demonstrates the calculated fractional power dissipated by electrons into different internal degrees of freedom in various gas mixtures as a function of E/n in discharge plasma.

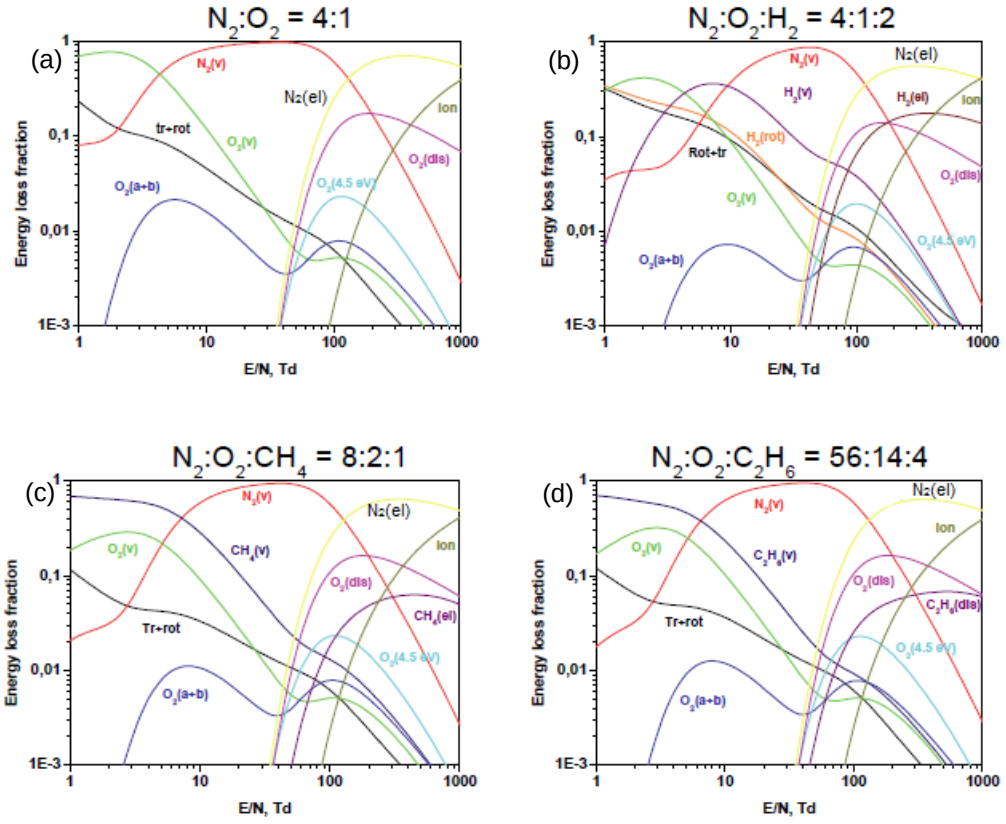

Figure 2.4 Fractional power dissipated by electrons into molecular degrees of freedom as a function of E/n. (a) Air; (b) Hydrogen-Air; (c) Methane-Air; (d) Ethane-Air stoichiometric mixtures [5].

At very low E/n (~ 0.1 Td) rotational excitation is dominated; here up to 85% of the discharge energy goes to this excitation. Fast energy exchange between rotational and translational degrees of freedom leads to equilibrium gas heating in this case. An increase

of the E/n value to 0.4 Td changes the priorities. Above this point the main channel of electron energy dissipation becomes vibrational excitation of oxygen. For reduced electric filed 4 Td < E/n < 110 Td, the most efficient channel of electron energy dissipation in air is vibrational excitation of nitrogen (Figure 2.4,a). Vibrational-translational (VT) relaxation is a rather slow process at low gas temperatures and the vibrational temperature in discharge plasma could be much higher than the translational one. In the same region of E/n, excitation of the lowest electronic level of oxygen, $O(a^1\Delta)$ state, takes place. The efficiency of this electronic excitation is very small (~2%) in the presence of nitrogen. But a low rate of $O(a^1\Delta)$ state oxygen quenching leads to its concentration increase under some conditions. It should be noted that an electric field value E/n ~ 120 Td is a very important threshold in air. Above this point the electric filed is enough to ionize the gas and the discharge can propagate in self-sustained regime. Below this value the discharge can exist only in the presence of external source of ionization. At E/n from 140 to 500 Td the main channel of energy losses is excitation of electronic triplet states of nitrogen. Because of high electrons energy in this range of E/n (from 3 to 10 eV, correspondingly) ionization of the gas in discharge gap is very fast. Between 500 and 1000 Td the excitation of nitrogen singlet states becomes most important, and above 1000 Td the main portion of the electron's energy goes to ionization of the gas.

Fuel addition in stoichiometric ratio (Figure 2.4 (b, c, d)) does not change this picture dramatically. The main reason is relatively small concentration of fuel molecules in the mixtures under typical combustion conditions. Figure 2.4(b) demonstrates the effect of hydrogen on the electron energy branching. The stoichiometric mixture H_2-air (H_2:O_2:N_2

= 29:14.5:56.5) contains about 30% of hydrogen. It follows from the calculations that these additives only slightly change the energy distribution at moderate and high E/n > 20 Td. Excitation of molecular nitrogen remains the main process. Vibrational and electronic excitation and ionization of hydrogen only slightly change the electron energy branching (Figure 2.4(b)). At low E/n < 10 Td, the effect of hydrogen addition becomes more significant. Vibrational excitation of hydrogen is the main channel of energy dissipation for E/n = 5-10 Td. The role of rotational excitation of hydrogen is also important and increases the energy flux into rotational and translational degrees of freedom at low *E/n* (Figure 2.4 (b)). Almost the same picture is obtained in the stoichiometric mixtures with hydrocarbon fuels, methane (Figure 2.4 (c)) and ethane (Figure 2.4 (d)).

Thus, the reduced electric field is an important parameter for plasma assisted combustion. The *E/n* value controls the direction of energy deposition in discharge and governs the composition of active particles produced in the discharge plasma.

In the simplest case, *E/n* is a function of the gas density, applied voltage and geometry of the discharge cell. Ignition and flame stabilization in different engines require different initial conditions. Gas temperature can vary from T~220 K (high-altitude re-light of an aircraft engine) to the value at the end of a typical compression process (T~700-800 K) and temperatures corresponded to the combustion stage (1000-2500 K). Typical gas density varies from 10^{17}-10^{18} cm^{-3}, which corresponds to conditions of hypersonic flight, and may be as high as (1-3)×10^{20} cm^{-3} for high pressure turbines or in typical automobile engines. At ambient temperature, this corresponds to a pressure range from a few Torr to tens of bar.

Precise control of the direction of energy deposition to specific energy modes in the plasma is possible over relatively short time scales when electron multiplication (when the reduced electrical field *E/n* is above the breakdown threshold, the electron multiplication dominates) or recombination (when below breakdown threshold, the recombination dominates) does not have enough time to change the concentration of electrons and plasma conductivity significantly. When plasma conductivity is not very high it is possible to maintain a desired value of *E/n* within the inter-electrode gap. This approach together with combination of short high-voltage pulse and constant bias produces a selective and extremely non-equilibrium excitation of the gas. Critical high-voltage pulse duration depends on the gas parameters (density, composition) but for the range of parameters encountered in practical systems it is restricted to few nanoseconds.

Therefore, the possibility of selective excitation of the gas by electric discharge critically depends on the generation of ultra-short high-voltage pulses. In modern pulsers the pulse rise time is as short as 80 *p*s, voltage rise rate reaches 1 MV/*n*s, maximal voltage 2-10 MV, and maximal current up to 100 *k*A. The wide range of possibilities ingenerated by current progress in solid-state electronics will lead to the increase of our abilities of non-equilibrium plasma generation with predicted properties.

2.2.2 Elementary Processes in Non-Equilibrium Plasma

For efficient production of a large number of active particles in the gas discharge it is necessary for both efficient generation in the gas discharge plasma and slow

recombination in subsequent collisions with major mixture components. Mechanisms to achieve these characteristics will be discussed in this section.

2.2.2.1 Rotational Excitation and Relaxation

Due to fast rotational-translational (RT) relaxation, excited rotational degrees of freedom of molecules are quenched rapidly. This process requires only a few collisions. For example, for rotational relaxation in air ($O_2(rot) + M \rightarrow O_2 + M$ and $N_2(rot) + M \rightarrow N_2 + M$), the typical relaxation time is comparable with gas-kinetics time. This means that typical period for rotational states relaxation is $\tau \sim 0.5$ ns under normal conditions. That is why rotationally-excited molecules cannot be considered as active particles for non-thermal acceleration of chemical reactions. Another important point is that the energy of excitation of rotational states is very small and is significantly lower than typical chemical reaction's thresholds. However, it is possible to heat the gas through the excitation of the rotational degrees of freedom excitation.

2.2.2.2 Vibrational Excitation and Relaxation

In contrast to excited rotational states, the relaxation (termed quenching) of the vibrationally excited states of N_2 and O_2 (vibrational-translational (VT) relaxation) is a very slow process. The VT relaxation time under low-temperature conditions is usually longer than the typical time scale required for plasma-assisted ignition (~10-100 μs). These times become comparable when the mixture contains significant amounts of H_2 or hydrocarbons. Therefore, vibrationally excited N_2 and O_2 molecules can be accumulated

in discharges with intermediate E/n values. Let us analyze the possibility for the acceleration of a chemical reaction by vibrationally excited reagents. The non-equilibrium vibrational excitation of reagents can significantly accelerate reactions if the thermal equilibrium reaction path includes a significant energy barrier [67].

Under conditions of incomplete vibrational relaxation, chemical reactions between vibrationally excited molecules play an important role. There are several theoretical models used to calculate the rate coefficients of the reactions that occur between excited species. Almost all of these models were developed as an engineering substitute for time-consuming ab initio calculations [68-71]. A model of vibrational energy usage [72] assumes a decrease in the reaction activation energy threshold by αE_{vib}. The efficiency of the vibrational excitation, α, can be estimated using the activation energy and the free energy of the reaction.

2.2.2.3 Excitation and Relaxation of Electronic Levels

At an E/n of ~100-500 Td, the primary mechanism of gas excitation is through the population of the electronic degrees of freedom by electron impact and the energy exchange between excited states. An important exception to this is the singlet state of molecular oxygen $O_2(a^1\Delta_g)$ (SDO). This state requires low excitation energy and has a relaxation time (also called long radiative lifetime).

A number of different electronically excited particles exist in low-temperature plasmas. Unfortunately, the reaction rate constants, the quenching rates and the products are

known for only a limited number of these excited states. For this reason, we mention only those levels most important from the point of view of plasma-assisted combustion.

The efficiency of electronic-state energy usage for plasma chemistry depends on the ratio between the mechanisms (radiation, collisional quenching, etc.) of the depopulation of a state. For example, if the radiative lifetime of the state is too short, some photon flux will exist, but no reactions can occur with this state. The efficiency of collisional quenching depends on the products of the reaction. The quenching of the triplet states of nitrogen molecules by molecular oxygen leads to oxygen dissociation and to atomic oxygen production. Another example is the quenching of singlet oxygen molecules by hydrogen or by hydrocarbons, which leads primarily to heat release without the formation of active radicals.

2.3 Numerical Study on Singlet Oxygen Production by Non-equilibrium Discharge: Low-energy Electronic States Excitation

The excitation thresholds of SDO and singlet sigma oxygen (O_2 ($b^1\Sigma^+_g$)) (SSO) molecules are very low. Nevertheless, the actual energy needed for excitation in the discharge is always higher than the theoretical value due to electron energy losses in other processes. In this section a simulation of the yield of singlet oxygen molecules for different electric discharge conditions is presented. The most important discharge parameter from the point of view of efficiency of energy deposition is the reduced electric field value, E/n. The electron energy distribution function (EEDF) is calculated as a local approximation using

the two-term spherical harmonic expansion of the Boltzmann equation. The set of cross-sections is used from BOLSIG+ package [73] for oxygen and nitrogen.

Figure 2.5 shows the energy distribution for different processes at different E/n in the discharge zone in an O_2-Ar (15%:85%) mixture. At E/n = 5 Td, 74% of the energy goes toward excitation of singlet oxygen. Approximately 53% goes to excitation of the singlet delta state $O_2(a^1\Delta_g)$, whereas about 21% goes to excitation of the singlet sigma state $O_2(b^1\Sigma_g)$. Thus, the discharge optimization could lead to efficient excitation of singlet states. It can be concluded that for the oxygen-argon mixture, the energy cost of radical generation is ~5 eV per radical, taking into account the mixing with hydrogen and collisional quenching of singlet oxygen molecules by H_2. At lower E/n, the main channel of energy losses is vibrational excitation in the O_2-Ar mixture. For E/n between 15 Td and 40 Td, the main source of energy loss is excitation of electronic levels at 4.5 and 6 eV, for E/n between 40 Td and 200 Td it is excitation at 8.4 eV, and for E/n > 200 Td it is ionization (Figure 2.5). Channels at 6 and 8.4 eV lead to molecular oxygen dissociation, producing two radicals per event. It is clear that in this case optimal E/n for radical production through dissociation by direct electron impact is about 70 Td, where the energy price per radical is ~6 eV (one dissociation event requires ~12 eV and yields two oxygen atoms). Thus, direct production of radicals using dissociation by electron impact has almost the same efficiency as radical productions by singlet states excitation, due to quenching of SDO molecules by fuel in the O_2-Ar mixture.

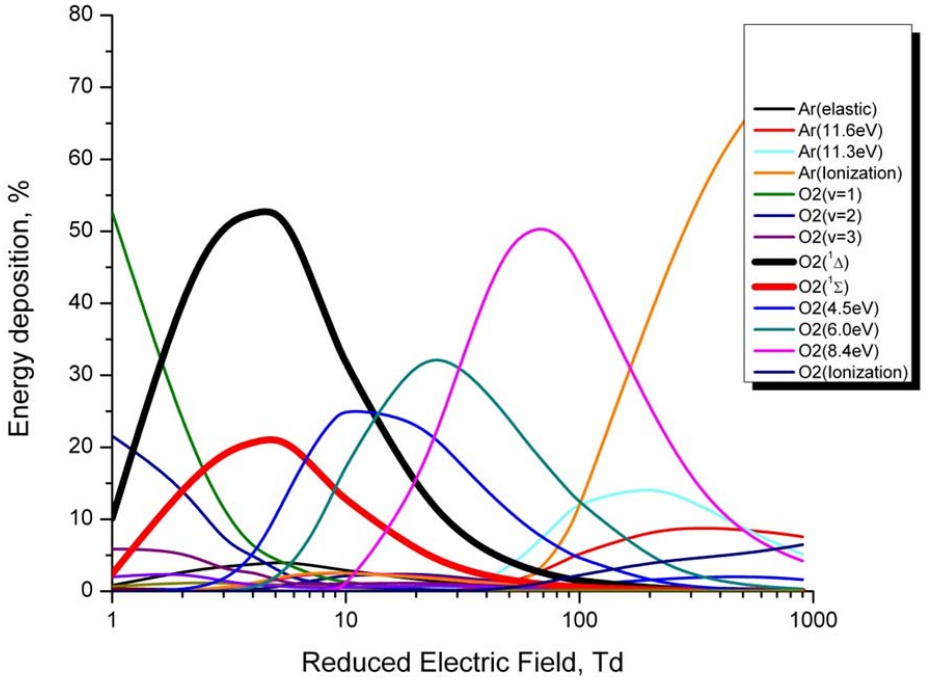

Figure 2.5 Energy Distribution in O_2-Ar (15%:85%) Mixture.

In the case of the O_2-N_2 mixtures, the efficiency of radical formation decreases at low E/n. The energy efficiency of SDO molecule production in air by optimized discharge is only 2.2% at 6 Td, as shown in Figure 2.6. The efficiency of SDO formation has a strong peak. Low E/n leads to energy deposition into rotational and translational degrees of freedom.

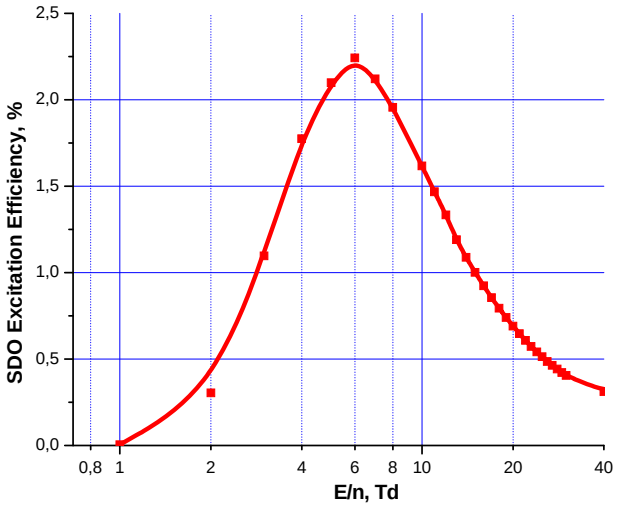

Discharge energy distribution, E/n = 6 Td

N_2 Elastique	1.8%
N_2(ROT)	4 %
N_2 (V=1)	49 %
N_2 (V=2)	7.3 %
N_2 (V=3)	1.4 %
N_2 (V=4)	0.2 %
O_2 Elastique	0.3 %
O_2 (ROT)	0.2 %
O_2 (V=1)	17 %
O_2 (V=2)	11 %
O_2 (V=3)	4.1 %
O_2 (V=4)	1.4 %
O_2 ($a^1\Delta_g$)	2.2 %
O_2 ($b^1\Sigma_g$)	0.1%

Figure 2.6 Efficiency of the SDO excitation in gas discharge

The main difference between discharge in oxygen and in air from the point of view of radical generation is the energy distribution to molecular degrees of freedom. In discharge in oxygen, there is a wide range of parameters from 2 to 20 Td where excitation of the singlet states is the most important process of energy deposition. In air, this region is occupied by excitation of vibrational levels of nitrogen (Table 2.1).

Table 2.1 Discharge energy distribution in air, *E/n* = 6 Td

Process	Energy deposited	Process	Energy deposited
N_2 Elastic N_2(ROT)	1.8% 4%	O_2 Elastic O_2 (ROT)	0.3% 0.2%
N_2 (V=1) N_2 (V=2) N_2 (V=3) N_2 (V=4)	49% 7.3% 1.4% 0.2%	O_2 (V=1) O_2 (V=2) O_2 (V=3) O_2 (V=4)	17% 11% 4.1% 1.4%
		O_2 ($a^1\Delta_g$) O_2 ($b^1\Sigma_g$)	2.2% 0.1%

Vibrational excitation of nitrogen depopulates the electron energy distribution function in the 2-3 eV region. Decrease of the oxygen concentration and EEDF decay leads to a significant decrease in the singlet oxygen (SO) molecule excitation rate. It should be noted that the vibrational temperature increase will decrease the energy deposition into vibrational degrees of freedom. However, this process will also lead to an increase in the electron temperature due to super-elastic collisions and will not increase the efficiency of oxygen excitation.

For a better understanding of the energy deposition difference between air and oxygen plasma, the energy distribution calculation was performed here by varying the concentration of nitrogen in the oxygen-nitrogen mixture. Figure 2.7 shows the energy distribution for the most important processes of the radical's formation. Two different regimes were considered. The first was optimized for excitation of oxygen singlet states (E/n ~ 5-10 Td, squares and circles), while the second was optimized for direct dissociation of oxygen by electron impact and atomic oxygen production by the quenching of nitrogen triplet states (E/n ~ 200-300 Td, triangles). Without the presence of nitrogen, much of the energy goes into singlet oxygen excitation, including the delta

and sigma states. This leads to low energy radical formation (~ 5 eV/radical) in the first regime. However, by raising the amount of nitrogen in the mixture, the energy distribution is changed significantly. The addition of 20% nitrogen into the mixture leads to an order of magnitude decrease in the energy deposition into singlet states of the oxygen (~7%, Figure 2.7).

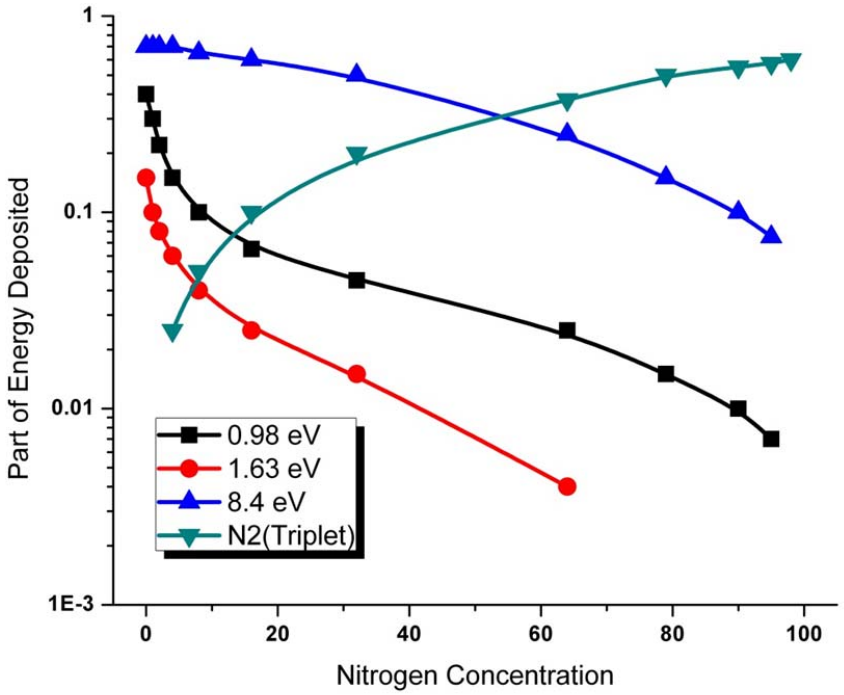

Figure 2.7 Energy distribution with different nitrogen concentrations

When the nitrogen concentration reaches the level of air (79%), the efficiency of SO excitation drops to 2.3%.

The regime that is optimized for direct oxygen dissociation and triplet nitrogen state quenching demonstrates a different behavior. In pure oxygen, the most important channel of oxygen dissociation through the 8.4 eV state absorbs about 70% of the energy in optimal conditions. Energy cost per radical remains relatively low (~6 eV/radical) but it is higher than the value for non-self-sustained discharge at low *E/n* (~5 eV/radical). An increase in the nitrogen concentration in the mixture leads to a decrease in the efficiency of the direct dissociation channel but activates another channel of atomic oxygen production through the quenching of nitrogen electronic states by molecular oxygen. The most interesting process from the point of view of radical production is the excitation of triplet states. The energy deposition into this process is very high (Figure 2.7). Under atmospheric pressure conditions, the main channel of depopulation is collisional quenching by molecular oxygen. The products of this process are two oxygen atoms, one in the ground state $O(^3P)$ and one in an excited state $O(^1D)$. Both have very high reactivity and $O(^1D)$ can react with all hydrocarbons and molecular hydrogen, even at room temperature conditions. At conditions of high E/n, when the mixture contains a high concentration of nitrogen, more than 60% of the energy goes into excitation of nitrogen electronic degrees of freedom and the process remains very effective up to very small oxygen concentrations in the mixture.

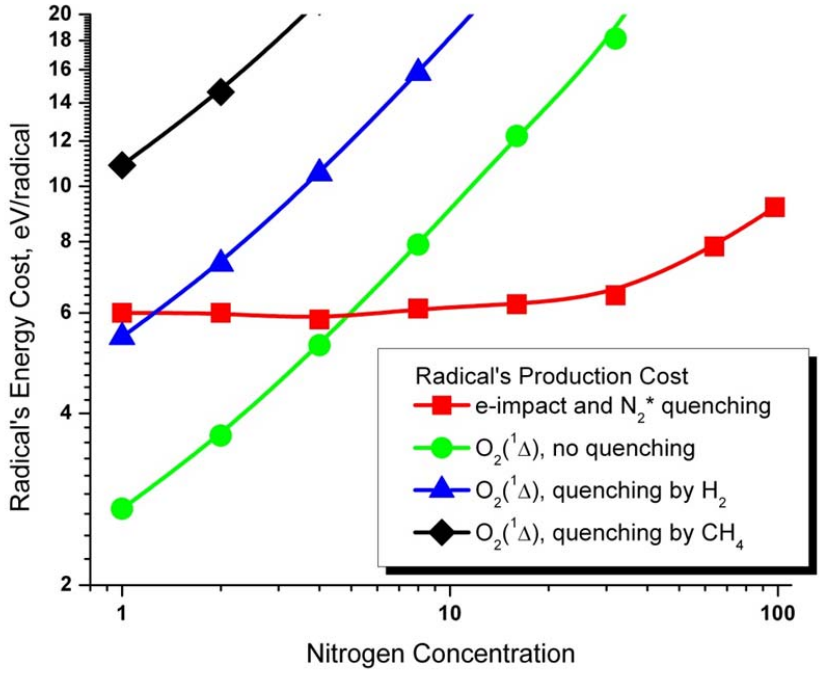

Figure 2.8 Energy cost of radicals production at different nitrogen concentrations

Figure 2.8 summarizes the energy cost of two different modes of radical production (through excitation of singlet oxygen at low *E/n* and through direct dissociation by e-impact and N_2 triplet states excitation at high *E/n*) for different concentrations of nitrogen. Similar to Figure 2.7, at low nitrogen concentration the cost of radical formation through singlet oxygen excitation is less than the cost of radical production at high *E/n* conditions. If we disregard the collisional quenching of SO molecules, the energy price per radical at low *E/n* in pure oxygen is less than 3 eV. However, taking into account the presence of quenching in the process, the situation changes significantly, even at low nitrogen concentrations (the energy price increases up to 5 eV/radical, vs. 6 eV/radical in

the case of excitation by discharge at high *E/n*). Moreover, by increasing the nitrogen concentration (for example, using a mixture that contains 10% nitrogen), the energy price for the "high *E/n*" channel becomes much lower than the energy cost of radical formation through the excitation of singlet states of oxygen molecules. In air, the difference between these two channels reaches an order of magnitude and makes the "low *E/n*" channel completely unsuitable as a radical source for plasma-assisted ignition and flame control. The "high *E/n*" channel shows a slow increase in the energy price per radical as nitrogen concentration increased (we stop the calculations at an N_2:O_2 ratio of 95:5). Of course, approaching pure nitrogen conditions causes the price of atomic oxygen production to go to infinity because of the absence of direct dissociation and the radiative depopulation of nitrogen excited states. In calculations using fuel-air stoichiometric conditions, we demonstrate that the energy price is about 8 eV/radical.

In summary, an analysis of the energy efficiency of radical production at different E/n has been performed. Two different mechanisms of radical formation were analyzed: 1) at low E/n - through oxygen singlet state excitation with subsequent quenching and conversion into radicals in reactions with fuel molecules, and 2) at high E/n – through direct dissociation of molecular oxygen by electron impact and quenching of nitrogen triplet states in collisions with molecular oxygen. It was shown that the first channel is more efficient in pure oxygen, whereas the second is significantly more efficient for mixtures containing more than 10% of nitrogen.

The typical energy price per radical for these two mechanisms was determined. For oxygen-fuel mixtures, the discharge at low E/n leads to an energy price of about 5

eV/radical, while the discharge at high E/n yields a price of ~ 6 eV/radical. In air, the discharge optimization at high E/n gives an energy price close to 8 eV/radical. The radical's price in the case of non-self-sustained discharge at low E/n in air reaches a value of about 100 eV/radical. This decrease in efficiency is explained by energy losses to vibrational excitation of nitrogen and quenching of SO molecules in collisions with hydrogen or hydrocarbons.

Thus, in order to minimize the radical's energy price, the discharge at low electric field values (E/n ~5-10 Td, singlet oxygen excitation) could be used in pure oxygen, while a high reduced field regime (E/n ~200-300 Td, molecular oxygen dissociation) is recommended to increase the efficiency of plasma assisted ignition in all nitrogen-oxygen mixtures, including air.

2.4 Closure

The physics of plasma-assisted combustion was reviewed and studied in this chapter. The elementary processes in non-thermal plasma were reviewed and different energy mode excitations were analyzed. A numerical study based on EEDF calculation provided the optimal plasma parameters to efficiently generating the chemically active species (atomic oxygen and singlet oxygen), which are of great importance in the enhancement of combustion.

Chapter 3 Kinetic Studies of Non-thermal Plasma-assisted Ignition above Auto-ignition Threshold[‡]

3.1 Introduction and Research Background

For gas temperature above the auto-ignition threshold, the use of singlet oxygen molecules as a tool for ignition and combustion control was proposed in the literature 0. The effect of exciting oxygen molecules to the $O_2(a^1\Delta_g)$ and $O_2(b^1\Sigma^+_g)$ electronic states in an electrical discharge on the velocity of laminar flame propagation in an H_2-O_2 mixture was analyzed. The calculations indicate that the excitation of the O_2 molecules to the $a^1\Delta_g$ and $b^1\Sigma^+_g$ electronic states causes a significant increase (by a factor of 2.5) in the velocity of the flame propagation for a lean hydrogen-oxygen fuel mixture. For stoichiometric and fuel-rich mixtures, the increase in the flame velocity due to an abundance of singlet oxygen molecules in the mixture was found to be significantly smaller (approximately a factor of 1.1). Later, it was proposed to use laser radiation at a λ = 762.346 nm for the excitation of O_2 molecules to the $b^1\Sigma^+_g$ electronic state.

Experimental observations of the shortening of the induction zone length in a premixed mode of combustion in a subsonic H_2-O_2 low-pressure flow due to the presence of oxygen molecules excited to the singlet $a^1\Delta_g$ electronic state were reported in [74]. A low-pressure electric glow discharge was used to produce singlet oxygen molecules. The analysis found that the presence of ~1% $O_2(a^1\Delta_g)$ molecules in the H_2-O_2 mixture

[‡] The results presented in this chapter can be found in the paper:
L. Wu, A.A. Fridman, A. Yu. Starikovskiy, "Kinetics of plasma assisted combustion at low reduced electric fields", AIAA-Paper 2010-1593, 48th AIAA Aerospace Sciences Meeting, January 4-7, 2010.

noticeably reduces the length of the ignition delay and allows the mixture to ignite at a lower temperature. The results demonstrate the potential to intensify the combustion of a hydrogen-oxygen mixture at a low pressure (P = 10-20 Torr) by applying an electrical discharge to increase the excitation of the O_2 molecules.

In this chapter, a brief introduction to singlet oxygen will be presented first. After that, a computational study on the kinetic analysis of the experiments [74] is presented in order to analyze the efficiency of radical generation through $O_2(a^1\Delta_g)$ and $O_2(b^1\Sigma^+_g)$ (singlet delta oxygen, SDO, singlet sigma oxygen, SSO or in general, singlet oxygen, SO) molecules. The analysis takes into account both the efficiency of the generation SO molecules in the discharge and the efficiency of the conversion of SO molecules into radicals.

3.2 Electronically Excited Oxygen: An Introduction

3.2.1 Excited Oxygen in Nature

Oxygen is important not only as the "normal" diatomic molecule O_2, but also in its excited molecular states, singlet delta oxygen, $a^1\Delta_g$, and singlet sigma oxygen, $b^1\Sigma^+_g$. Singlet oxygen has been known since 1924. In 1979, Michael Kasha relates the accidental way in which singlet oxygen was re-discovered in 1960 by means of the reaction [75]:

$$ClO^- + H_2O_2 \rightarrow H_2O + Cl^- + O_2^* \tag{3.1}$$

Singlet oxygen is quite reactive and is responsible for oxidative damage in a number of systems, even in biological area. Excited states and other active species of oxygen are

important to the world's carbon cycle because of their contribution to the degradation of organic substances. Furthermore, species such as singlet oxygen ($a^1\Delta_g$ and $b^1\Sigma^+_g$), excited hydroxyl radical (OH^*), superoxide (O_2^-), and alkyl peroxy radicals (ROO^*) are among the most important species in the aquatic environment. They are formed primarily by the action of sunlight on surface waters and are responsible for the indirect photochemical degradation of a wide variety of organic species [76].

Electron collisions with oxygen molecules are an important energy loss mechanism in the earth's ionosphere [77] and in the plasmas produced by electron beams. Additionally, $O_2(b^1\Sigma^+_g)$ excited state is of considerable importance in atmospheric processes. In the thermosphere, it is a strong radiation source by this main reaction:

$$O(^1D) + O_2 \rightarrow O(^3P) + O_2(b^1\Sigma^+_g) \rightarrow O_2 + h\nu \text{ (761.8 nm)}. \quad (3.2)$$

Lastly, the $a^1\Delta_g$ state of O_2 is of great interest as reagent of possible importance in atmospheric chemistry [78]. In the earth's upper atmosphere $O_2(a^1\Delta_g)$ is produced primarily from the photolysis of ozone, and its concentration reaches a maximum of about $4 \cdot 10^{10}$ cm^{-3} at 50 km during the day time [79]. Atmospheric airglow has been measured from the ground, aircraft, balloons, and rockets and using a high-resolution spectrometer on a telescope. The 1.27 μm emission from $O_2(a^1\Delta_g)$ and the 762 nm emission of $O_2(b^1\Sigma^+_g)$ are major components in airglow. These species can be formed by direct absorption of UV radiation, e.g.:

$$O_2 + h\nu \rightarrow O_2^* \quad (3.3)$$

and by photo-dissociation of ozone:

$$O_3 + h\nu \rightarrow O_2^* + O^* \quad (3.4)$$

where O^* is an excited oxygen atom.

Another pathway is through recombination of oxygen atoms:

$$O + O + M \rightarrow O_2^* + M \quad (3.5)$$

where M is a third body collision partner. The complete analysis of airglow spectra is very complicated and many other reactions are taken into account.

3.2.2 Approaches in Production of Excited Oxygen Molecules

Singlet oxygen can be generated via multiple methods, including thermal excitation, optical excitation, electrical excitation, or a combination of these approaches. It can also be produced through reactions of a chemical fuel additive or a laser-excited chemical additive [80, 81].

3.2.2.1 Laser Production of Singlet Oxygen

The most common ways to produce singlet oxygen is through photosensitization, or more precisely, energy transfer to O_2^* from an excited state of a sensitizer, which is formed by the absorption of light in a specific wavelength region. Singlet oxygen photosensitization is highly favored in nature. This is due to the very special electronic configuration of molecular O_2. Energy transfer quenching of both excited singlet and triplet states is spin allowed, in contrast to many competing deactivation processes. Moreover, the excitation energies for both $O_2(b^1\Sigma^+_g)$ and $O_2(a^1\Delta_g)$ are lower than the energy state of many organic triplets, and in most cases, the energy difference is small enough to make the process

irreversible. In addition, due to the small size of the O_2 molecule, it allows for rapid diffusion in many media, where other intermolecular process cannot compete with oxygen reaction.

Singlet oxygen photosensitization takes place in the chemical system where light is absorbed in the presence of molecular oxygen. In many cases, energy transfer results in the formation of both $O_2(a^1\Delta_g)$ and $O_2(b^1\Sigma^+_g)$. However, the spin-allowed $b^1\Sigma^+_g \rightarrow a^1\Delta_g$ deactivation process occurs at an extremely high rate in the condensed phase. Thus, eventually all $O_2(b^1\Sigma^+_g)$ will be converted to $O_2(a^1\Delta_g)$.

Another approach to produce singlet oxygen molecules is through laser-induced excitation. A gaseous mixture containing oxygen is exposed to a laser pulse at a wavelength in resonance with the transitional wavelength of $X^3\Sigma^-_g \rightarrow b^1\Sigma^+_g$ and $X^3\Sigma^-_g \rightarrow a^1\Delta_g$ for molecular oxygen [82].

3.2.2.2 Chemical Production of Singlet Oxygen

Singlet oxygen can be generated via reaction with Cl_2 in a basic H_2O_2 solution. Exothermic chemical reactions generate singlet oxygen as a product, illustrated by the well-established hypochlorite-peroxide reaction (3.1).

Moreover, a purely chemical and very effective way of generation of O_2^* exploits the following reaction (in liquid phase):

$$Cl_2 + HO_2^- \rightarrow H^- + 2Cl^- + O_2^* \qquad (3.6)$$

This reaction takes place in a thin near-surface liquid layer, and the yield can be close to unity (because the production of O, O_3 and other excited species are not encountered with possible quenchers in the pure chemical system).

Furthermore, energy-rich compounds that generate $O_2(a^1\Delta_g)$ by thermal decomposition include phosphate ozonides : $(RO)_3PO_3 \rightarrow (RO)_3PO + O_2(a^1\Delta_g)$ and endoperoxides such as 9,10- diphenylanthracene peroxide (DAP) :

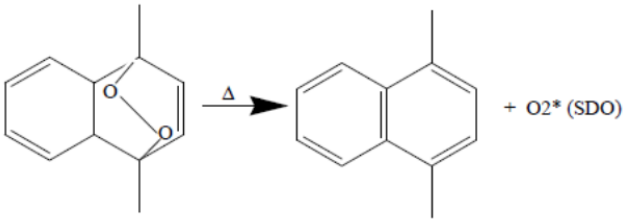

(3.7)

3.2.2.3 Plasma Generation of Singlet Oxygen

An alternative procedure for singlet oxygen production is by electrical discharge [65]. First observation of singlet oxygen produced by an electrical discharge was made by Foner and Hudson [83] in a very long, typically 1 m, U-shaped discharge tube with hollow electrodes, operating at a pressure of several *k*Pa in an AC glow regime. In recent decades, plasma generation of singlet oxygen has been mainly used for laser gain application [84]. Researchers have tested a variety of plasma discharges in production of singlet oxygen, including DC glow discharge, microwave discharge, and RF discharges.

3.3 Kinetic Model of Plasma-assisted Ignition above auto-ignition threshold

Having highlighted the multiple roles of SO in nature, the focus is now shifted back to its role in promoting fuel ignition and combustion. Recent experimental results [74] have shown that the presence of singlet oxygen molecules in a hydrogen-oxygen mixture decreases the ignition delay time. Experiments with lifted flame stabilization confirm the possibility of ignition and combustion control using this approach. In this section, a chemical model is assembled to analyze the influence of singlet oxygen on combustion and to identify the key pathway which is associated with it.

The ignition process was numerically simulated using the kinetic scheme described in 0, which includes 12 reactive species (H_2, H, O_2, O, O_3, $O(^1D)$, $O_2(a^1\Delta_g)$, $O2(b^1\Sigma^+_g)$, OH, HO_2, H_2O_2, H_2O) and 80 reactions. Calculations were carried out in zero-dimensional approximation at a fixed gas pressure.

In the kinetic calculations, the ignition delay time is defined as the interval between the instant at which singlet oxygen molecules are injected and the onset of an abrupt increase in gas temperature. To validate the calculated results, the simulation is compared to the experimental data [74]. The main goal of the comparison was to analyze the influence of reactions not included in the mechanisms [85]. In particular, we were looking for mechanisms of excited species re-generation (so-called “energy back-coupling mechanisms”):

$$A^* + B = C + D^*$$

$$D^* + A = D + A^*$$

If A* is an SO molecule, we can expect long reactive chains. The potential length of the chains generated by this mechanism is limited only by reactions of quenching:

$$A^* + M = A + M$$

In the case of SO molecules, the probability of excited species formation in reactions with hydrogen and hydrocarbons has not been previously analyzed. Thus, the energy back-coupling mechanism could, in principle, lead to an increase in the production of radicals from a single SO molecule. Comparison with the results described in 0 will allow us to analyze the existence of energy back-coupling in this specific chemical system.

Experimentally, the length of the induction zone was measured by Smirnov, et al. [74] in a plug-flow reactor (Figure 3.1). In order to calculate the ignition delay time based on the induction zone length [74], two approaches are used: the average gas velocity and velocity corrected for the laminar velocity profile (parabolic shape). Gas parameters in the experiment [74] using the H_2:O_2=5:2 mixture were T = 775 K, P = 10 Torr.

The ignition delay times under different conditions (including autoignition and ignition with different doses of singlet oxygen) were calculated and demonstrated in Table 3.1.

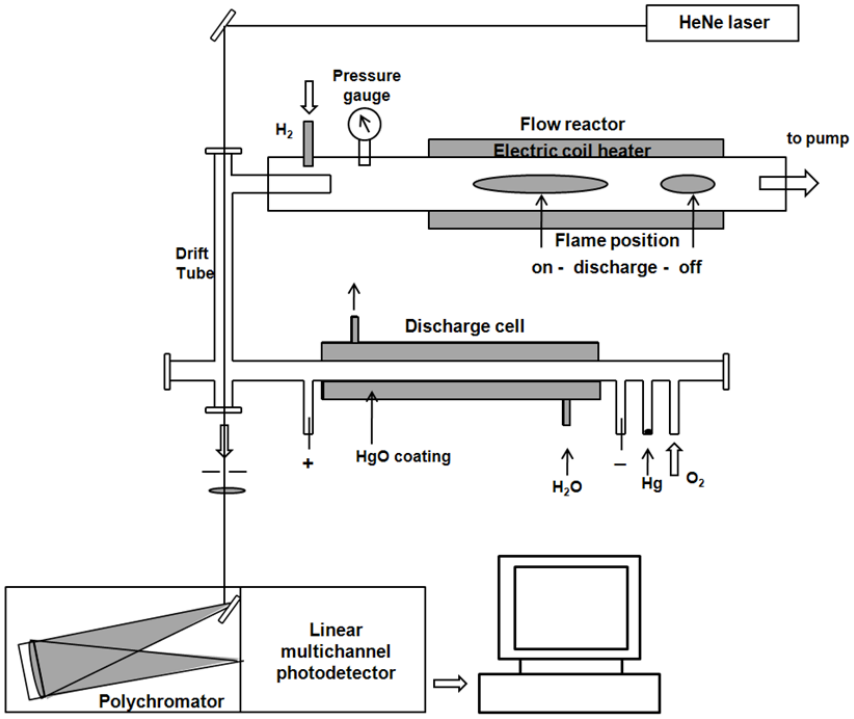

Figure 3.1 Schematic of experimental installation [74].

Table 3.1 Measured ignition delay time for different concentrations of SDO

Mole fraction of SDO (%)	**0**	**1.2**	**4**	**6**
Induction Zone Length, L_{in} (cm), [74]	51	27	18.6	16.8
Ignition delay time τ_e (ms) =L_{in}/v_0 , [74]	***12.9***	***6.8***	***4.7***	***4.2***
Calculated ignition delay time τ_c (ms) corrected for laminar velocity profile, and deviation of calculated τ_c from the experimental value,%	***12.3*** ***4.6%***	***5.8*** ***14.7%***	***4.7*** ***0%***	***4.4*** ***4.8%***

Based on the 0-D kinetic model, the ignition delay times for different mole fractions of SDO were calculated. The results of this comparison are shown in Figure 3.2. It can be clearly seen that the calculated ignition delay time predicted by the 0-D model is approximately 4 times longer than the values measured experimentally. This is the result that would be predicted, due to the 2-D nature of the gas flow in the experimental installation used in [74]. Low gas pressure (P = 10 Torr) leads to the fast boundary layer formation and Poiseuille's flow field development. This flow is characterized by parabolic velocity distribution across the tube and leads to a significant difference in the residence time for different flow lines. Usually it is very difficult to calculate 2-D flow when taking into account unknown surface properties (rate of radical recombination, heat transfer rate, etc.) but the experiment [74] gives a very important point of the mixture auto-ignition with zero initial concentration of SDO molecules. Taking into account the fact that, up to the point of ignition, the gas dynamics of the flow are not affected by the addition of small amounts of SDO, we are able to correct the calculations using auto-ignition data (Figure 3.2). Good agreement between experiment and our calculations has been achieved for the entire range of initial concentrations of SDO.

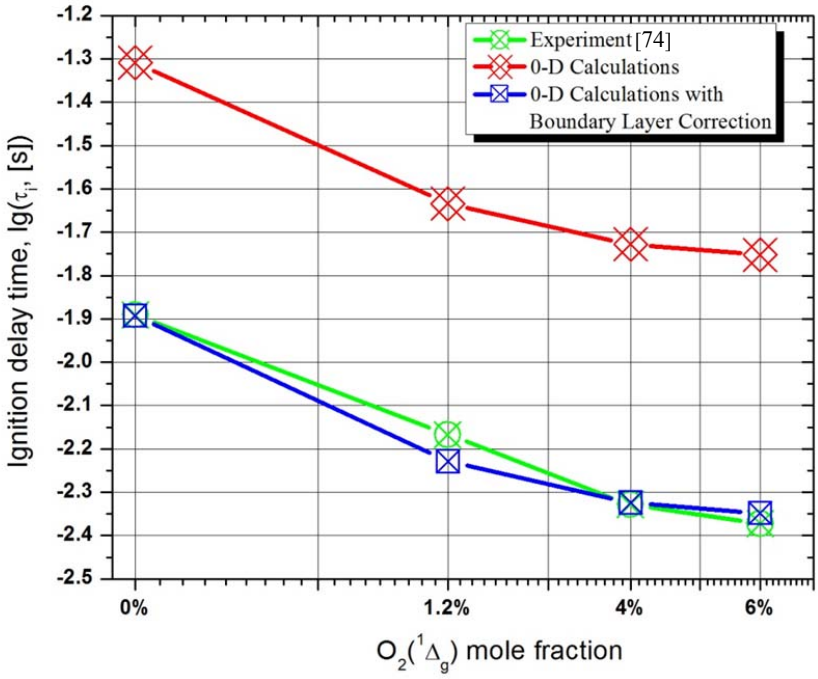

Figure 3.2 The ignition time in the H_2:O_2=5:2 mixture as a function of singlet delta oxygen mole fraction in oxygen. Comparison between experiment results [74] and calculations.

To demonstrate the mechanism of the influence of SDO on the ignition process, Figure 3.3 compares the evolution in time of the rates of dominant chemical reactions for auto-ignition and plasma-assisted ignition modes. The calculations show that the injection of sufficient singlet delta oxygen molecules leads to efficient ignition initiation. Indeed, the rates of the reactions are low during the induction phase of auto-ignition and rise by several orders of magnitude only immediately before ignition. In the case of plasma-assisted ignition, the active singlet delta oxygen produces a sufficient amount of OH

radicals during the earliest initial stage of the process. Due to the high density of OH radicals, the rate of the reaction $H_2 + OH = H_2O + H$ is high. Consequently, the rates of chain branching reactions increase dramatically. As a rule, during the induction period of SDO-assisted ignition, the role of radical-radical reactions becomes more important than the role of reactions between radicals and molecular reagents.

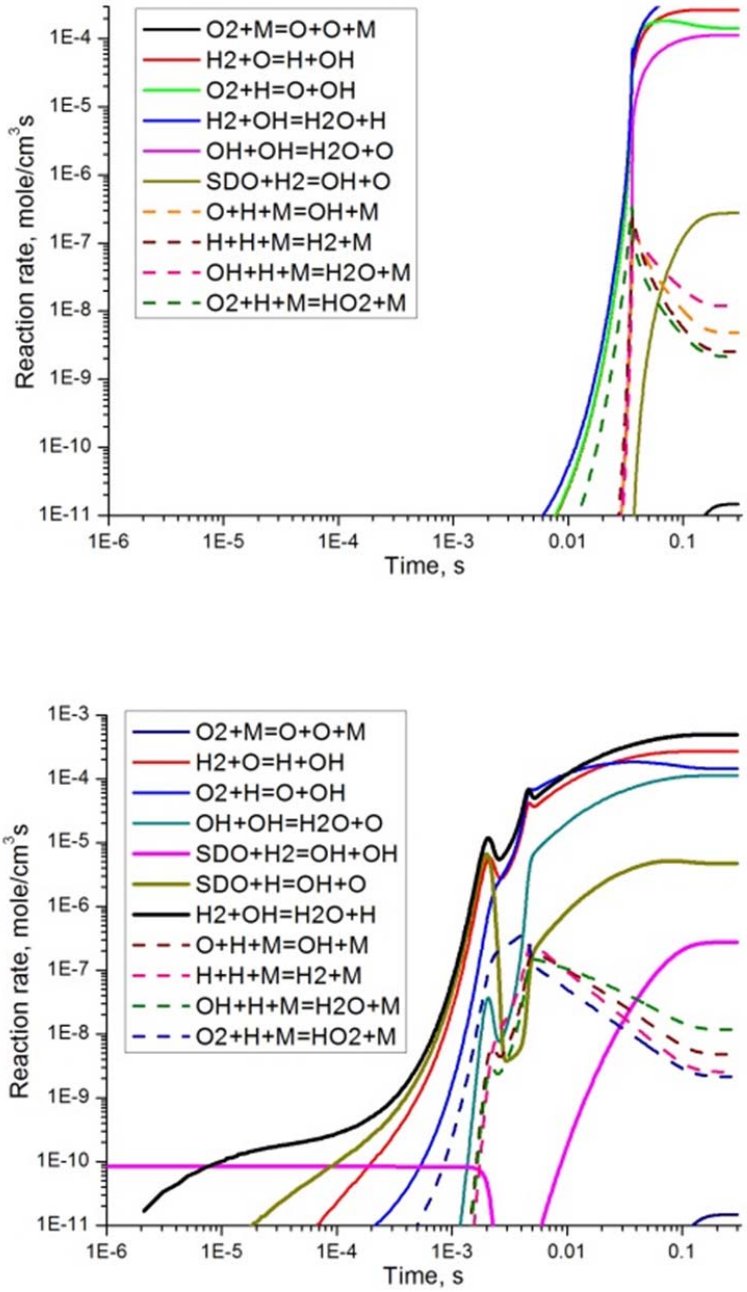

Figure 3.3 The evolution in time of the calculated rates of the main chemical reactions for autoignition (top) and ignition promoted by 6% of singlet delta oxygen (bottom).

Figure 3.4 shows the evolution in time of the mole fractions for the main components of the mixture during auto-ignition and plasma-assisted ignition, respectively. In the induction phase of auto-ignition, the density of atoms and radicals is low until ignition. For plasma-assisted ignition, the concentrations of H, O, and OH species increase rapidly during the initial 20 μs and initiate chain reactions, leading to a decrease in the ignition delay time.

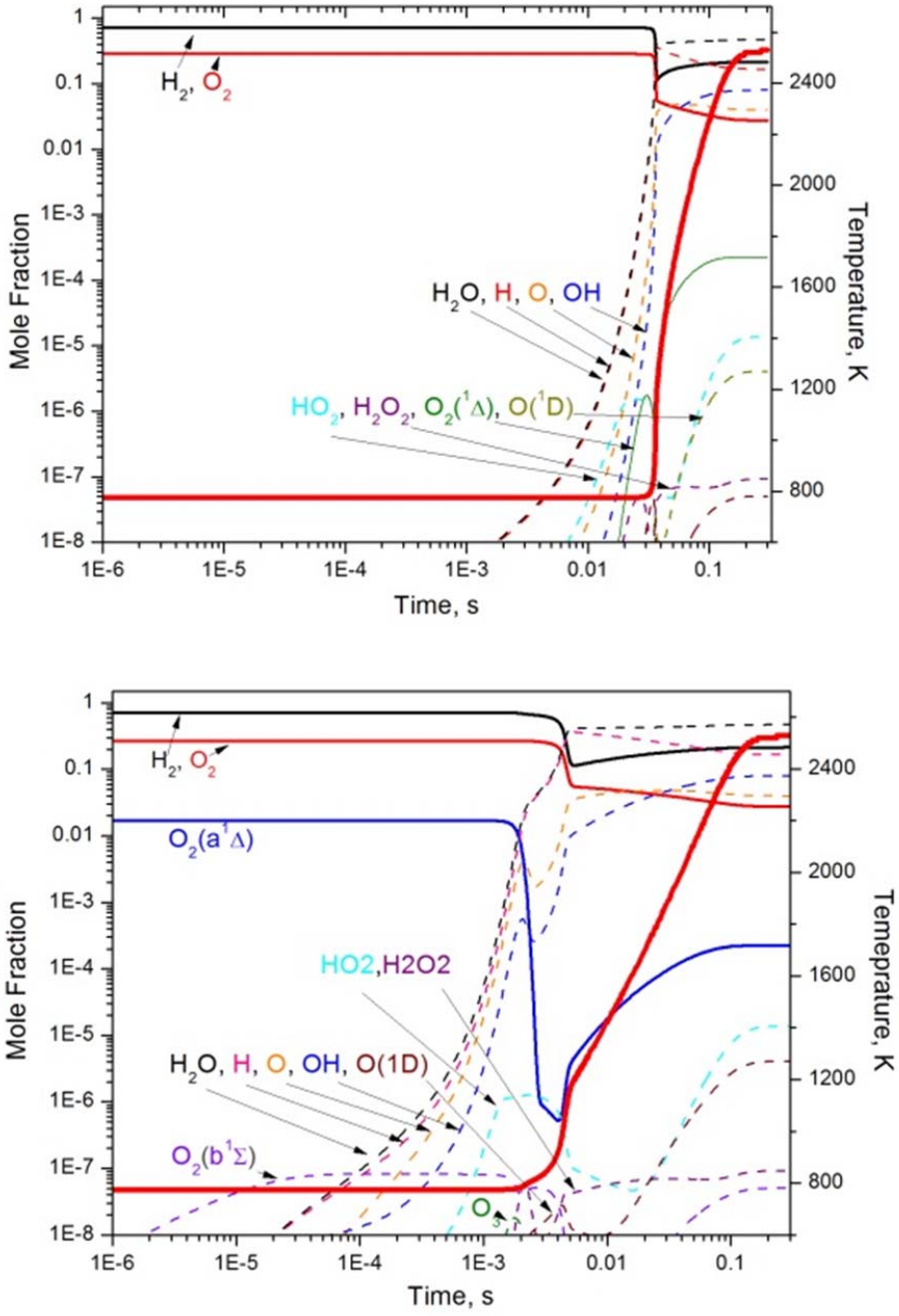

Figure 3.4 The evolution in time of the mole fractions of the main component for autoignition (left) and ignition with 6% singlet delta oxygen (right). The gas temperature evolution is represented by the solid red line.

The kinetics of the system can be described in several steps. At the beginning of the ignition phase, OH radicals are effectively produced through the reaction

$$O_2(a^1\Delta_g) + H_2 = OH + OH \quad (3.8)$$

This reaction leads to an increase in the OH concentration, which causes an increase in the rate of the reaction

$$H_2 + OH = H_2O + H \quad (3.9)$$

In other words, the efficiency of the production of H atoms rises significantly. Consequently, the rate of the reaction

$$O_2(a^1\Delta_g) + H = OH + O \quad (3.10)$$

increases immediately, which can be clearly seen in Figure 3.3. At approximately 80 μs after the process begins, reaction (3.3) of OH formation becomes more important than (3.1). As a result, these three reactions (3.1)-(3.3) create a new channel of chain initiation reactions, which plays the key role during the induction phase of SDO-assisted ignition.

The sensitivity analysis of the kinetic scheme was performed using mixtures with 0%, 1.2% and 6% singlet delta oxygen for ignition delay time. In order to perform this analysis, the rate constant of each reaction was in turn doubled two times and the ignition delay time was calculated separately for each case. The sensitivity coefficients were calculated as $(\tau_i - \tau_0) / \tau_0$, where τ_0 is the ignition delay time calculated using initial rate constants and τ_i is the ignition delay time calculated using the increased rate constant of the *i-th* reaction. The results of the calculations are given in Figure 3.5. The delay time for SDO-assisted ignition is less sensitive to the variation in the rates of the reactions of chain initiation

than that for auto-ignition. Due to the high concentration of active species at the beginning of the induction period, the recombination reactions demonstrate higher sensitivities in the SDO-assisted case than in the case of auto-ignition. At the same time, the role of chain branching reactions ($O_2 + H = OH + O$) decreases because the role of O_2 has been replaced by SDO, particularly during most important initial phase of the process.

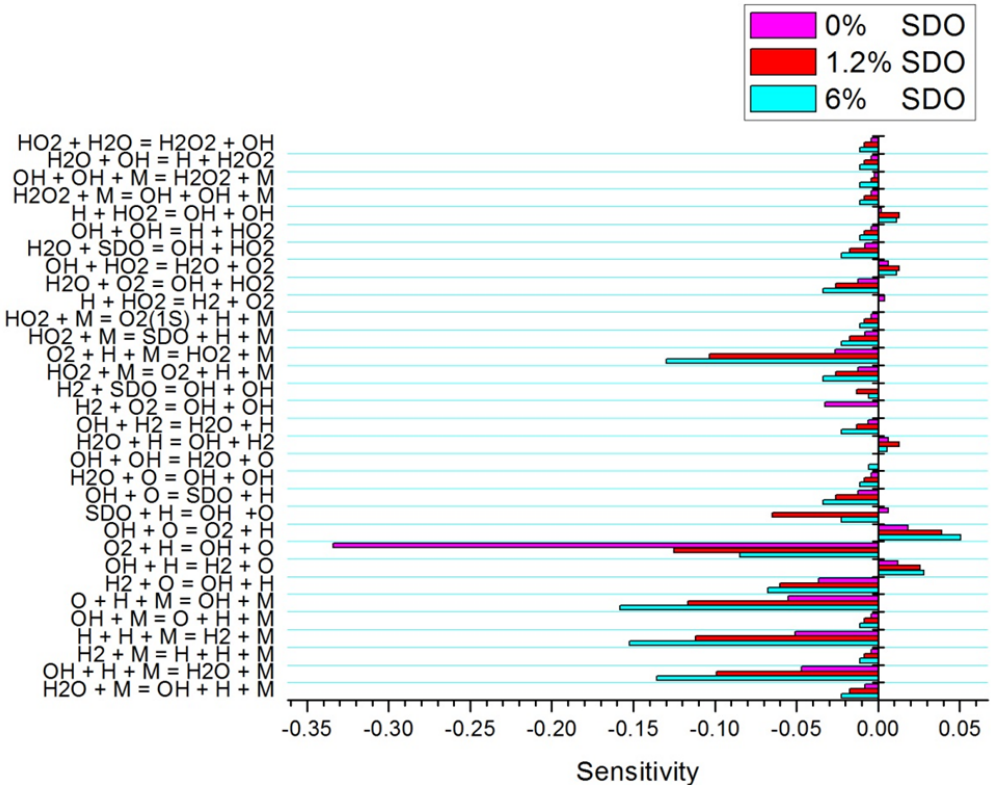

Figure 3.5 The sensitivity analysis for ignition with 0%, 1.2% and 6% of singlet delta oxygen mole fractions in oxygen respectively, at T=775 K and P=10 Torr in the H_2:O_2=5:2 mixture.

Thus, kinetic modeling gives us insight into the conversion of electronically excited oxygen into radicals, the initiation of the chain reactions, and ignition. To estimate the efficiency of plasma-assisted ignition at low reduced electric field conditions, it is necessary to estimate the relative consumption of SDO molecules in different reactions.

Figure 3.6 demonstrates the reaction rates related to SDO. Figure 3.6a shows the rate of SDO consumption, and Figure 3.6b shows the reverse reaction rates which lead to production of SDO. From the figure, it is clear that during initial stage of the process there is consumption only. No SDO molecules were produced during induction period. The main channels of SDO consumption are reactions (1) and (3). Reaction (1) leads to the generation of two radicals from one SDO molecule (200% efficiency) while reaction (3) gives only one radical per SDO consumed. Thus, the radical generation efficiency begins at about 200% ($O_2(a^1\Delta_g) + H_2 \rightarrow OH + OH$), but reduces to 100% ($O_2(a^1\Delta_g) + H \rightarrow OH + O$) after about 80 μs.

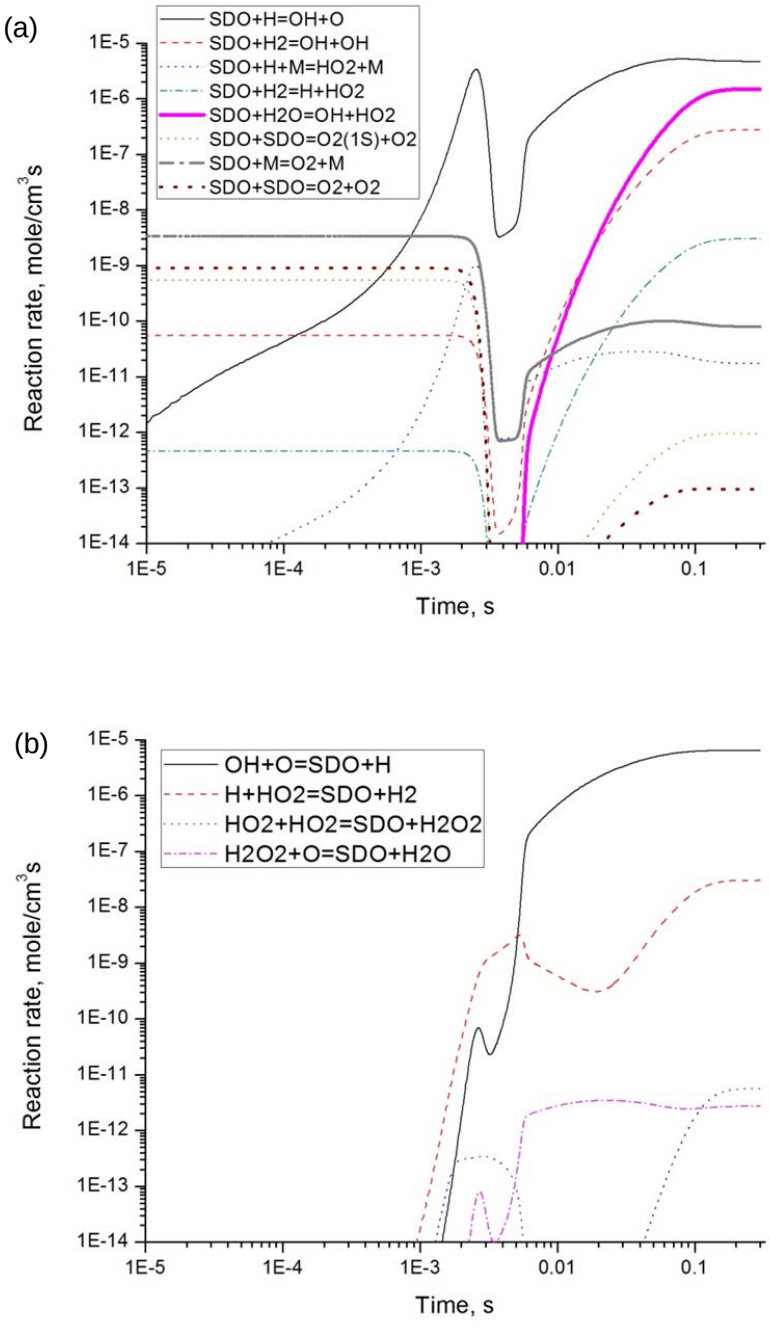

Figure 3.6 Main Reactions involving Singlet Delta Oxygen. (a) SDO Consumption; (b) SDO Production

During the initial stages, these processes compete with the quenching (Figure 3.6). The most important channel is collisional quenching

$$O_2(a^1\Delta_g) + M \rightarrow O_2 + M \qquad (3.11)$$

where M = H, H_2, C_xH_y, or $O_2(a^1\Delta_g)$. The quenching rate in the stoichiometric mixture H_2-O_2 is almost two orders of magnitude higher than the rate of the chain initiation reaction (3.1). Reaction (3.3) is initially very slow and becomes the main source of SDO consumption after 1 ms (Figure 3.6a). As a result, the efficiency of the conversion of SDO into radicals is much less than unity. This value depends on the mixture's composition, pressure and gas density. Overall value of the conversion efficiency is k = 0.1-0.3.

It is important to note that there is no SDO production during the induction period of ignition (Figure 3.6b). This means that the only source for SDO molecules is the discharge. The kinetic model described in this paper accurately reproduces the dependence of the ignition delay time on the SDO concentration of the mixture (Figure 3.2). This comparison gives experimental verification for chemical kinetic model in the discharge afterglow.

The efficiency of converting SDO molecules into radicals is relatively low due to fast quenching. Mechanisms of SO production during the induction period (such as energetic back-coupling) did not demonstrate any influence on the process and probably do not exist.

3.4 Closure

The multiple roles of singlet oxygen in nature were reviewed, and the role of singlet oxygen in PAI of hydrogen-oxygen mixtures is numerically analyzed. Results of kinetic modeling at low E/n values are compared with available experimental data and good agreement between experimental and computational results has been demonstrated. It was shown that the efficiency of radical production through oxygen singlet state excitation is limited by collisional quenching of singlet oxygen molecules in oxygen-fuel and by vibrational excitation of nitrogen in oxygen-nitrogen mixtures.

Chapter 4 Kinetic Studies of Non-thermal Plasma-assisted Ignition below Auto-ignition Threshold[§]

An investigation on kinetic mechanism of plasma-assisted ignition (PAI) above the auto-ignition threshold was presented in the previous chapter. This chapter will detail an investigation of the chemical kinetics of PAI below the auto-ignition threshold. After a brief introduction of the research background and the optical diagnostic techniques, the facility and the experimental methodology employed are described in detail. The results indicated that, after generation by the plasma, the hydroxyl radical (OH) persisted at significant concentrations for an extended period of time; a period that lengthened with increasing temperature. Measurements indicate that no significant temperature rise occurs. Therefore this is not likely to be a thermal effect and must be a result of "plasma induced" kinetics: whereby new reaction pathways are triggered by the creation of unique radicals by the plasma. Investigations described herein have paved the way to identify the pathways in this process.

[§] The results presented in this chapter can be found in the papers:

a. L. Wu, J. Lane, N.P. Cernansky, D.L. Miller, A.A. Fridman, A.Yu. Starikovskiy, "Plasma-assisted ignition below self-ignition threshold in methane, ethane, propane and butane-air mixtures", Proceedings of the Combustion Institute, 33 (2011) 3219–3224
b. L. Wu, J. Lane, N.P. Cernansky, D.L. Miller, A.A. Fridman, A. Yu. Starikovskiy, "Time resolved PLIF imaging of OH radicals in the afterglow of nanosecond pulsed discharge in combustible mixtures", IEEE Transactions on Plasma Science, 39 (11), 2604-2605
c. L. Wu, J. Lane, N.P. Cernansky, D.L. Miller, A.A. Fridman, A.Yu. Starikovskiy, "Time resolved PLIF and CRD diagnostics of OH radicals in the afterglow of plasma discharge in hydrocarbon mixtures", 7th US Combustion Meeting – Paper # 2H17, Atlanta, GA, 2011
d. Liang Wu, Jamie Lane, Michael Stichter, Nicholas Cernansky, David Miller and Alexander Fridman, "Effects of N2(v) and NO in Plasma-assisted Oxidation and Ignition below Auto-ignition Threshold", AIAA-Paper 2013-1051, 51st AIAA Aerospace Sciences Meeting, Grapevine, Texas, 2013

4.1 Background

The temperature of a gas mixture after compression in an engine often reaches the temperature range below or close to auto-ignition threshold of hydrocarbons (~800 K), whether they be reciprocating engines (< 600 K); gas turbines (600-700 K); or scramjets (650-800 K). This is why this critical temperature range attracts the attention of researchers. While the high flame-like temperature chemical kinetics of hydrocarbons have been studied for almost 100 years, chemical kinetics in this regime has only been considered for the last 3 decades. One problem lies in the lack of data for the validation of low temperature mechanisms. As an example, the methane combustion GRIMech-3.0 model was validated in the range of 1250-2500 K. The C_1-C_4 Konnov mechanism was validated down to ~910 K and Popov's hydrogen mechanism [86] was validated down to 880 K. The direct extrapolation of these models to room temperature conditions, or even to an intermediate temperature range below self-ignition threshold, is questionable. Thus, the task of investigation the kinetics in the low-temperature region becomes difficult and complex. One has to take into account the kinetics of the gas discharge and the plasma afterglow along with the almost unknown mechanisms of the initiation of chemical chains under low-temperature conditions.

4.2 Experimental Design and Setup

The plasma-assisted ignition experiments in this study were conducted in a newly developed flow reactor facility at Drexel University. A schematic of the experimental

installation is shown in Figure 4.1. The diagram illustrates the main components of the facility: the reaction chamber, the discharge system, the diagnostic system and the signal generator that synchronized the plasma and laser.

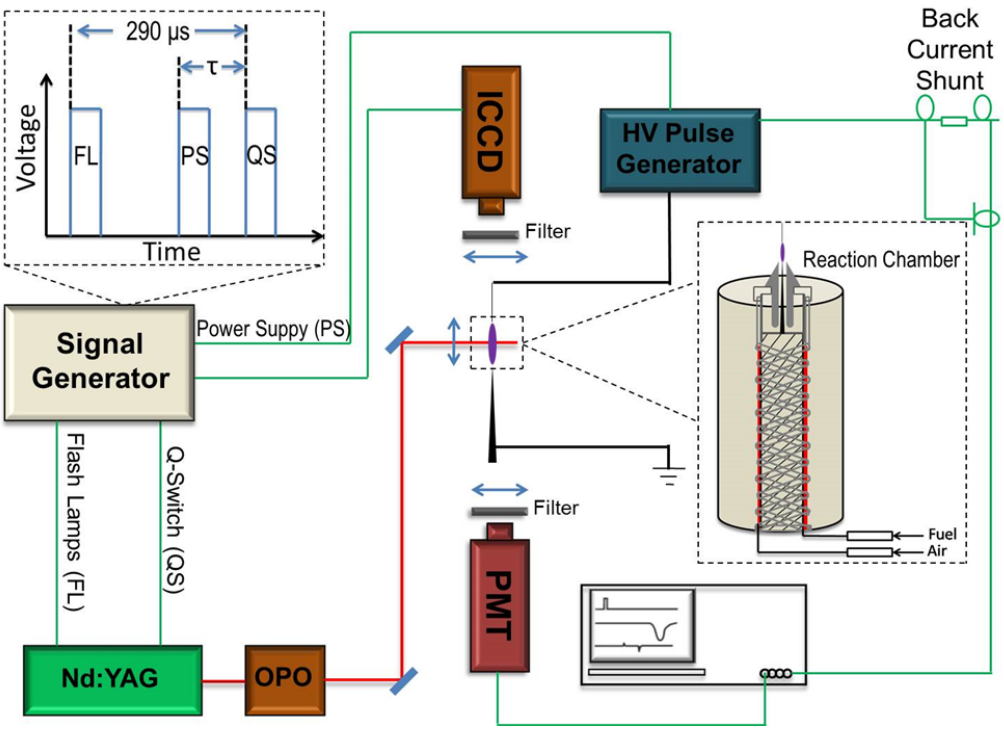

Figure 4.1 Experimental installation for plasma-assisted ignition analysis below auto-ignition temperature.

4.2.1 The Reaction Chamber

The design purpose of this plasma burner was to study chemical kinetics of the plasma treated fuel-air mixture below auto-ignition temperature threshold. Therefore, it was crucial to build the burner with the capability of controlling gas flow rate and temperature. In addition, the high voltage discharge system also needed to be incorporated into the

burner. As shown in Figure 4.2, the reaction chamber was about 20 inches in height, including the gas (fuel and air) supply system, the heating elements, the mixing chamber and the plasma nozzle.

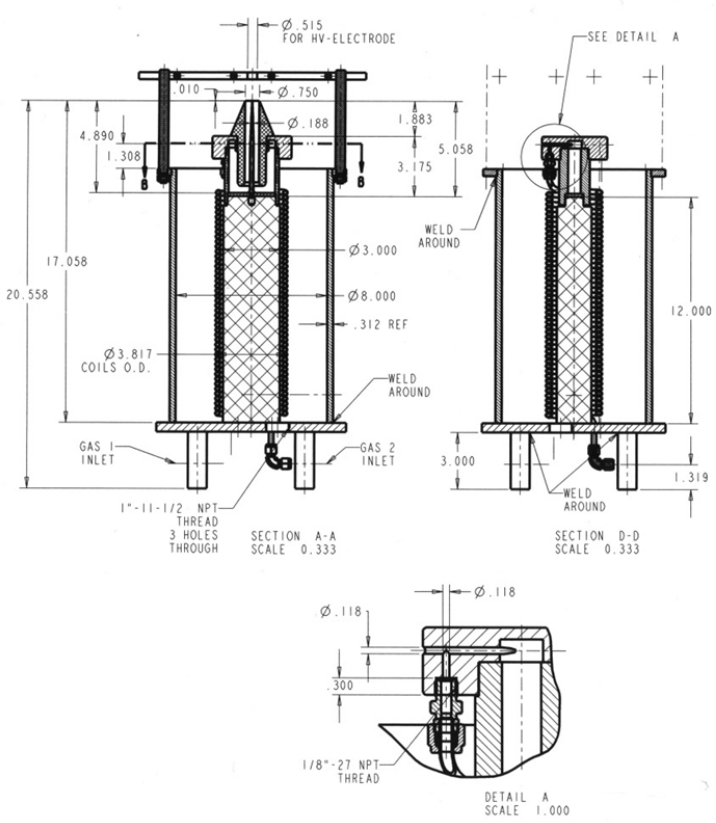

Figure 4.2 The engineering drawing of the reaction chamber.

To better describe the experimental setup, another figure is illustrated here (Figure 4.3). Gas flows enter from the bottom of the cylinder and were preheated in a thermally insulated region from 300 K up to 800 K. Two thermocouples were installed at the middle of the cylinder and the top of the mixing chamber to monitor to avoid overheating.

The spiral structure of the tubing ensured enough flow residence time to heat up the gases. The gas mixing was achieved at the mixing chamber after two rotating flows meet there. The mixing chamber and plasma nozzle were alumina ceramics for additional thermal and electrical insulation. The discharge gap was set directly above the nozzle along the axis of the premixed flow. For most experiments, the flow rate of the air was set at 5000 cm^3/s, while the flow rate of the fuel was set according to the equivalence ratio. The detailed parameters are shown in Table 4.1.

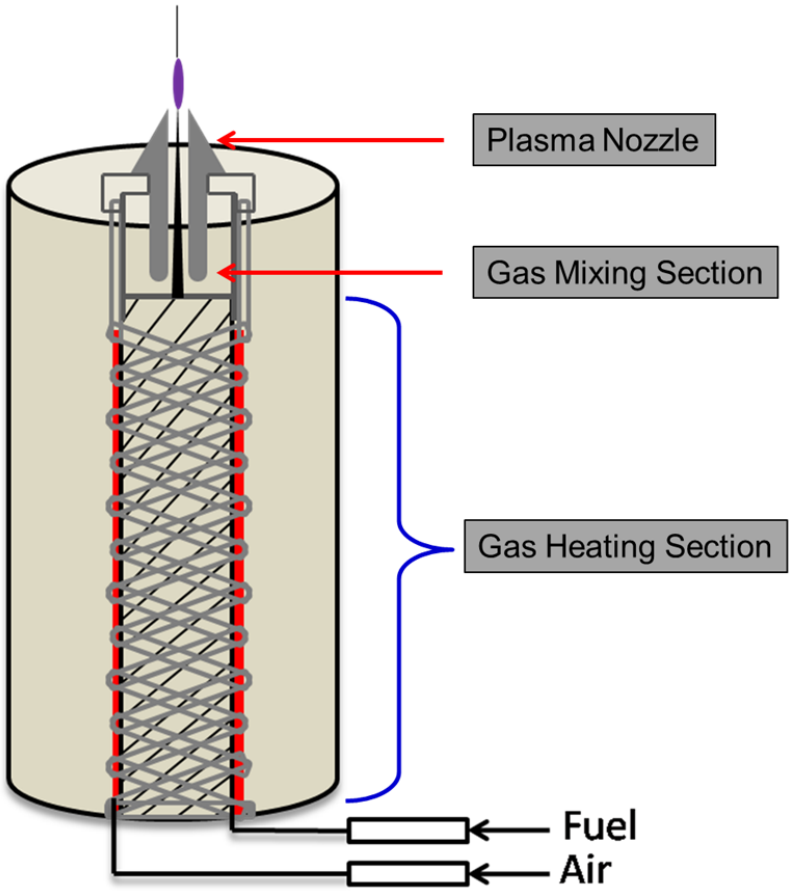

Figure 4.3 The schematic of the reaction chamber.

Table 4.1 Experimental parameters in plasma assisted ignition experiments

Fuel type	CH_4, C_2H_6, C_3H_8, C_4H_{10}, H_2
Equivalence Ratio	$\phi = 0.1$
Temperature	300 K – 800 K
Flow rate	~20 cm/s
Discharge Pulse rate	10 Hz
Electrodes diameter	200 μm (upper electrode) 500 μm (lower electrode)
Discharge gap	8 mm

4.2.2 The Discharge System

The discharge system was composed of the high voltage pulse generator (FPG 20-01NK10, FID GmbH), the coaxial cable and two electrodes. The diameters of the anode (high-voltage electrode) and cathode (grounded electrode) were 200 and 500 μm, respectively. The inter-electrode distance was 8 mm. The plasma was generated by positive pulses of ~20 kV with duration of about 10 ns. The rise time is less than 1 ns with a repetition rate of 10 Hz. The reactant flow rate was selected to be 20 cm/s to allow each discharge pulse to occur in a fresh gas mixture.

A calibrated back-current shunt was installed between the high-voltage generator and the discharge cell to measure the amplitude and the shape of the high-voltage pulse. The shunt was composed of low inductive resistances, soldered into the break of the cable shield. A Tektronix DPO4104 oscilloscope was used for registration of the electrical signals. The coaxial cable length was chosen to be long enough to separate the initial pulse generated by the generator and the pulse reflected from the discharge section or the generator due to the difference in impedances of various sections of the transmitting

circuit. The pulse energy W was calculated as $W = \int I^2 Z dt$, where I is the current in the line measured by the shunt and Z is the wave impedance of the line (equal to 50 Ω). The difference between incident and reflected pulse energies was regarded as the energy input in the discharge.

4.2.3 The Optical Diagnostic System

The optical diagnostic system consists of a Nd:YAG/optical parametric oscillator (OPO) (Continuum Powerlite 9010 YAG/Sunlite OPO) laser system, a photomultiplier tube (PMT) (Hamamatsu R562), an optical emission spectroscope (OES) (Acton Research SpectraPro 500i), and two fast gated ICCD cameras (Stanford Computer Optics, 4 Picos; Princeton Instruments, PI-MAX II).

The saturated LIF method was used to measure the concentration of OH radicals after the discharge. A BBO-based frequency doubling system generated the ultraviolet radiation at 282.92 nm needed for OH $Q_1(6)$ transition excitation. Quartz spherical lenses produced high power density at their focal point using the initial TEM_{00} mode of the laser beam. Fluorescence signals were obtained using a quartz lens and the PMT. The energy of the excitation laser was adjusted to E > 12 mJ/pulse to ensure that the measurements were made under saturation conditions for all experiments. The time evolution of OH radicals was tracked by adjusting the delay between the high-voltage pulse and the concentration measurement using the signal generator (upper left in Figure 4.1).

A planar laser-induced fluorescence (PLIF) method was used to visualize the OH distribution along the discharge channel. The schematic of the setup is illustrated in

Figure 4.4. The laser system was tuned to 282.92 nm for excitation of the Q1(6) transition of OH. Quartz cylindrical lenses were used to create a laser sheet across the whole discharge channel. Fluorescence images of OH were obtained using a band-pass filter (310 nm, 12 nm FWHM) with an ICCD camera (Princeton Instruments, PI-MAX II). All the images were taken with 20 accumulations in order to obtain a better resolution. The time evolution of OH dynamics was tracked by adjusting the delay between the high-voltage pulse and the laser using a signal generator.

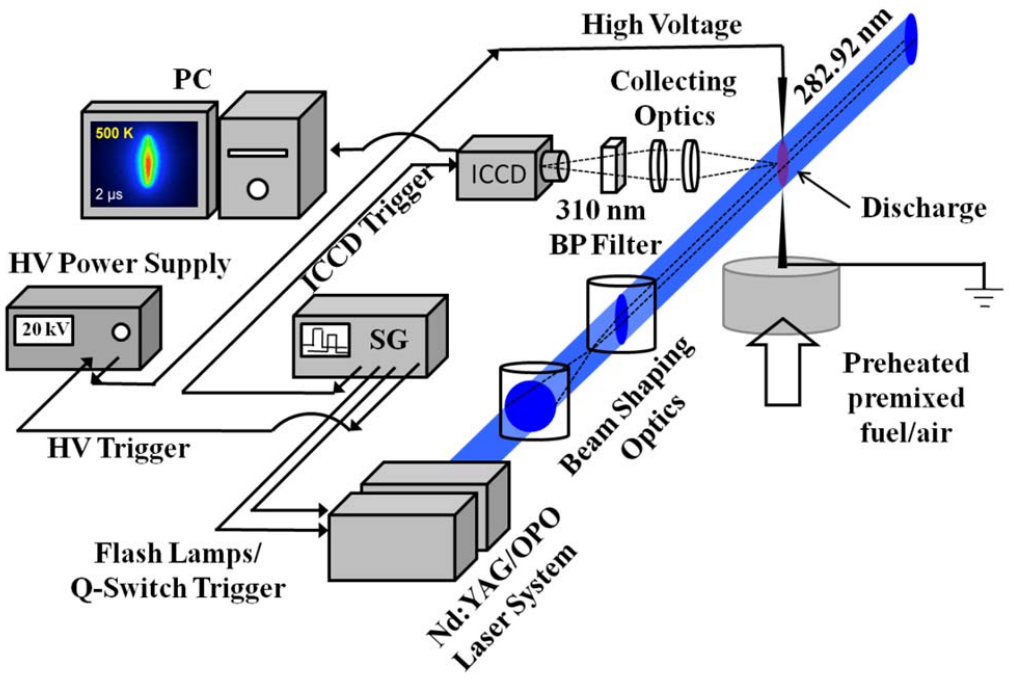

Figure 4.4 Experimental facility for time-resolved PLIF diagnostics of plasma assisted ignition analysis below auto-ignition temperature. HV: High voltage. SG: Signal generator. ICCD: Intensified charge-coupled device. BP: Band-pass.

The Cavity Ring-down Spectroscopy (CRDS) method used to make absolute OH concentration measurements is illustrated in Figure 4.5. The 50 cm optical cavity was constructed of two highly reflective plano-concave mirrors (Los Gatos, R = 99.95%). A 2:1 Keplerian telescope coupled with a 50 μm pinhole was implemented to mode match the laser beam with ring-down cavity. The Nd:YAG/OPO laser system was scanned over the $A^2\Sigma$ (υ = 0)←$X^2\Pi$ (υ = 0) Q1(1) absorption feature near 307.9 nm for each delay point. The exponential decay of light exiting the cavity was collected with a PMT (Hamamatsu R562) and averaged over 40 consecutive laser pulses on a 500 MHz digital oscilloscope (LeCroy LT342). The averaged ring-down signal was then sent to a LabView data acquisition program and fit to an exponential function. The ring-down time was extracted from the exponential fit and plotted versus wavelength. The details of the CRDS measurements will be discussed later.

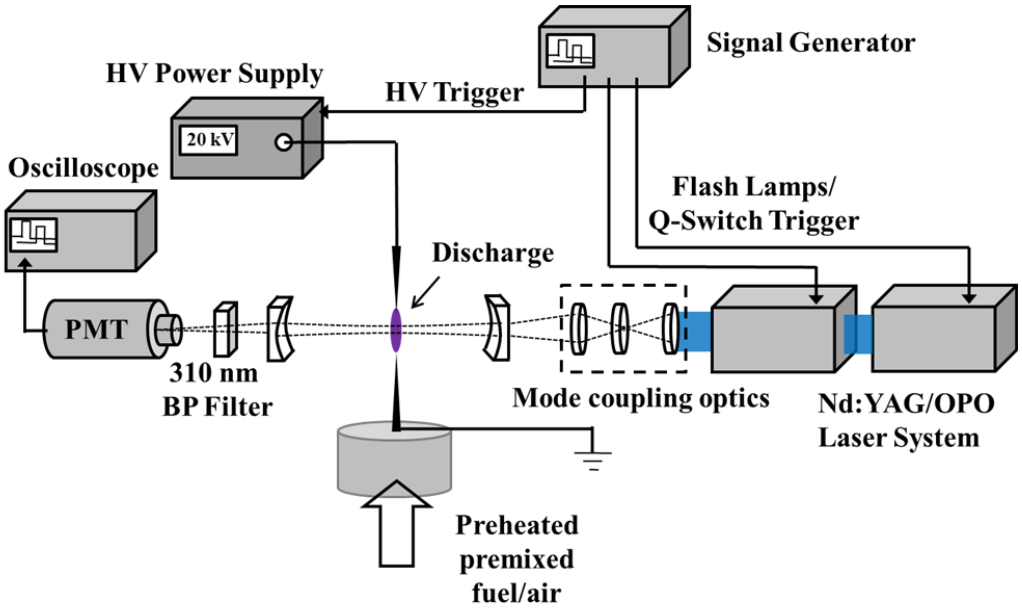

Figure 4.5 Schematic of the time resolved cavity ring-down spectroscopy of plasma-assisted ignition analysis below auto-ignition temperature.

Temperature measurements were performed via OES together with a thermocouple (Figure 4.6). OES recorded the rotational temperature in the discharge zone by capturing the emission of the second positive system of the N_2 molecule at 337.1 nm. The gas temperature was stable to within ±10 K in the discharge gap. Thus, all temperatures shown in the results section were the initial gas temperatures measured by the thermocouple.

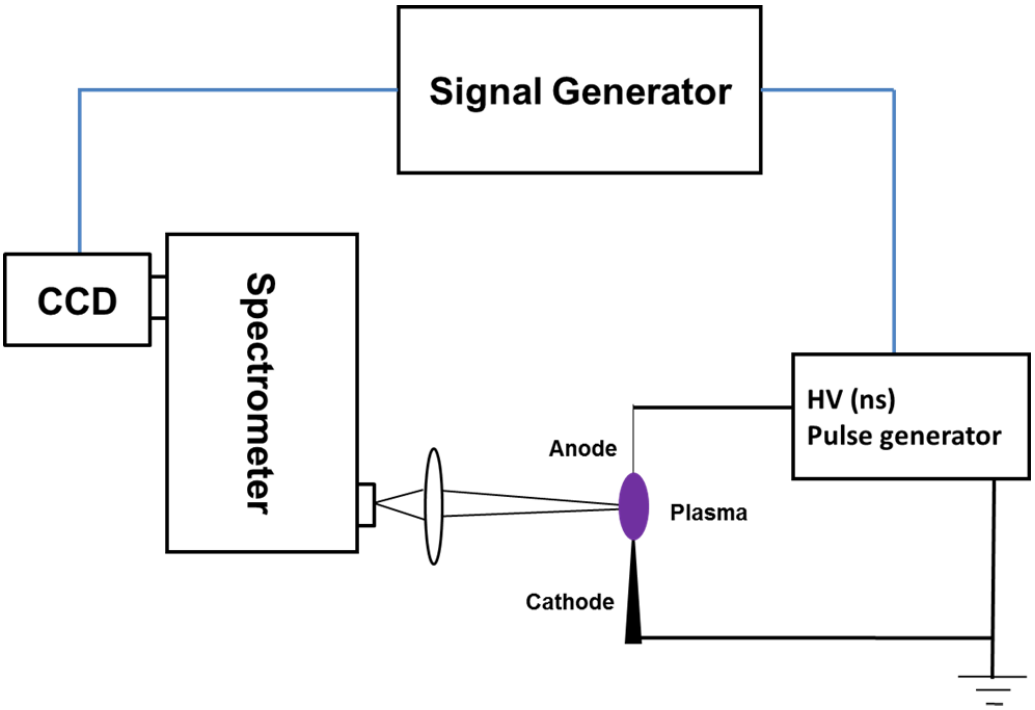

Figure 4.6 Illustration of the rotational temperature measurements via optical emission spectroscopy.

To enhance our knowledge of the discharge, an ICCD camera was used to record the plasma evolution (Figure 4.7). Through synchronization, this picosecond-gated camera was able to trace the entire streamer development.

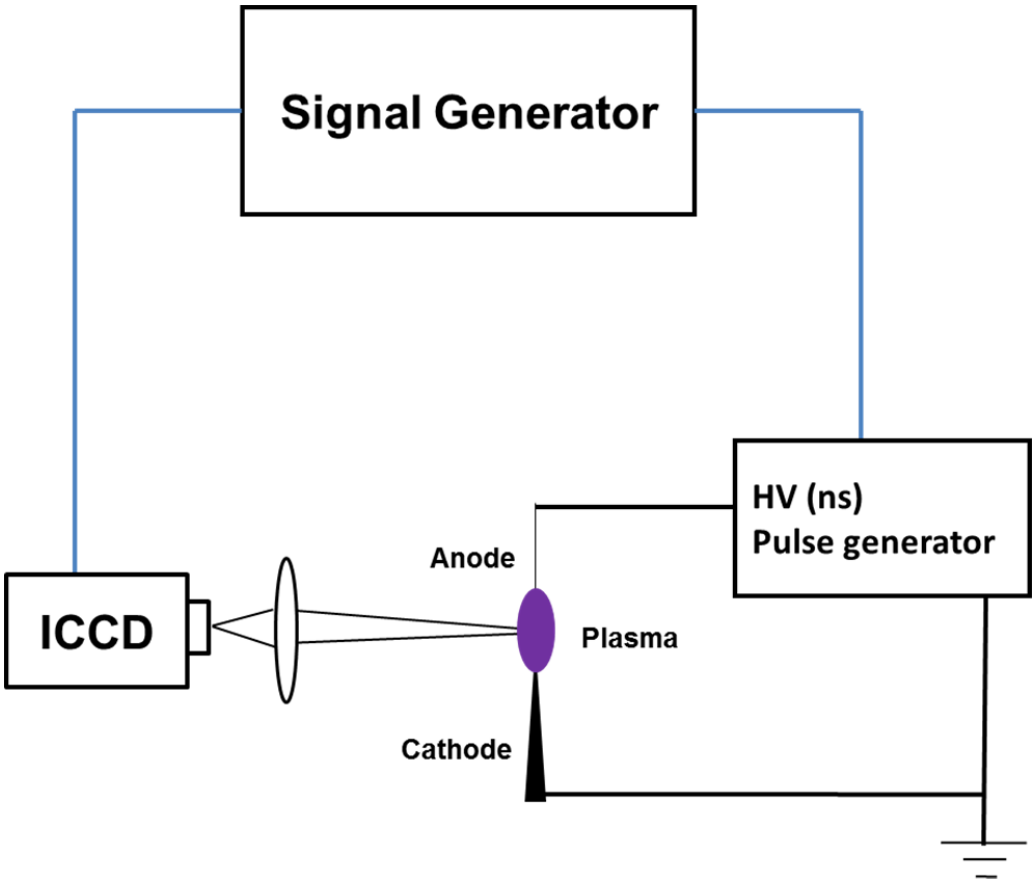

Figure 4.7 Schematic illustration of the time-resolved plasma discharge development measurement via fast gated ICCD camera.

4.3 Results and Analysis

4.3.1 Plasma Discharge Physics

Figure 4.8 shows the voltage waveform generated from the nanosecond power supply. It is clearly seen that the voltage pulse on the high-voltage electrode reaches its maximum in less than 1 ns. This ultra-short rise time leads to stable and repeatable plasma channel formation.

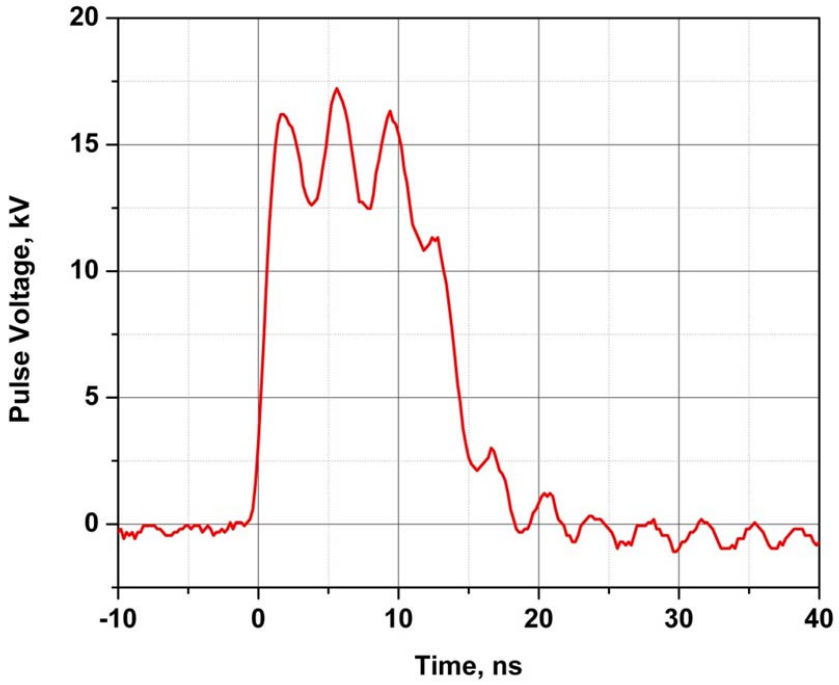

Figure 4.8 Discharge voltage waveform.

The discharge development is shown in Figure 4.9. ICCD camera gate was 200 ps and spectral response range was 190–750 nm. In nanosecond time scale the main emission source is second positive system of molecular nitrogen ($N_2(C^3) \rightarrow N_2(B^3)$ transition, radiative life time ~40 ns). Figure 4.9 presents false-color pictures. Typical emission profile is shown for 5.2 ns image.

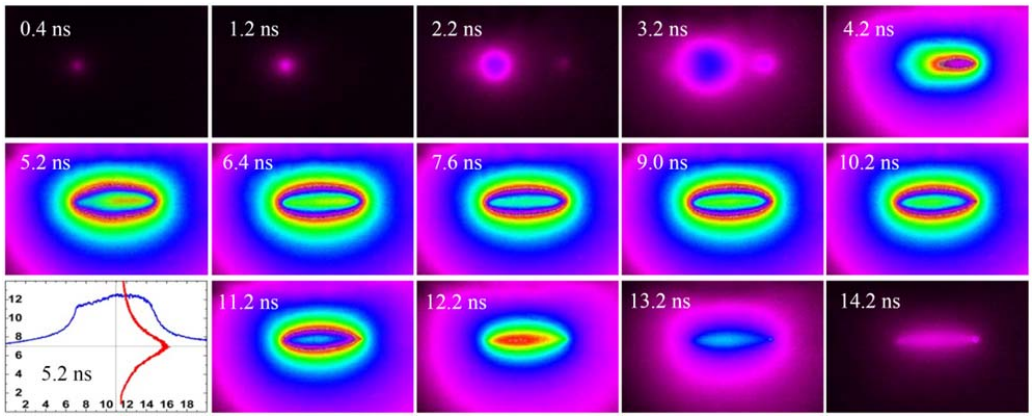

Figure 4.9 Sequenced ICCD images of plasma discharge development between two electrodes, camera gate is 200 ps. Air, P = 1 atm, U = 20 kV. High-voltage electrode on the left, grounded on the right. Inter-electrode distance 8 mm. Image size is 20 × 14 mm.

The discharge starts at the high-voltage electrode, and after about 4 ns, the streamer channel bridges the discharge gap. The redistribution of the potential along the gap has a form of ionization wave, propagating in the opposite direction – from low-voltage to high-voltage electrode (return stroke). Subsequently, the reduced electric field in the plasma channel becomes lower than the breakdown field (E/n ~ 120 Td (1 Td = 10^{-17} Vcm^2) for room-temperature air), and slow plasma recombination begins. The typical time of the plasma degradation in this field is several microseconds, and this degradation does not affect the discharge current, gas excitation or dissociation during the pulse (~ 10 ns). It should be noted that the discharge during the high-current stage decreases the effective plasma channel diameter (compare pictures 3.2 and 5.2 ns). The boundary of the emitting channel remains within the initial streamer channel but the excitation becomes less uniform.

When the potential decreases, the fast quenching of the main emitting state begins.

At this time, the plasma channel becomes invisible. During the discharge between the two needle electrodes, the streamer channel remains uniform, which is beneficial for our experiments.

4.3.2 Time-resolved OH LIF Measurements in the Afterglow of the Plasma Discharge

To confirm LIF saturation, OH signals from the stoichiometric methane–air flame were recorded by varying the power of the laser beam. Figure 4.10 shows that once the laser power exceeds 12 mW, LIF is in saturated mode.

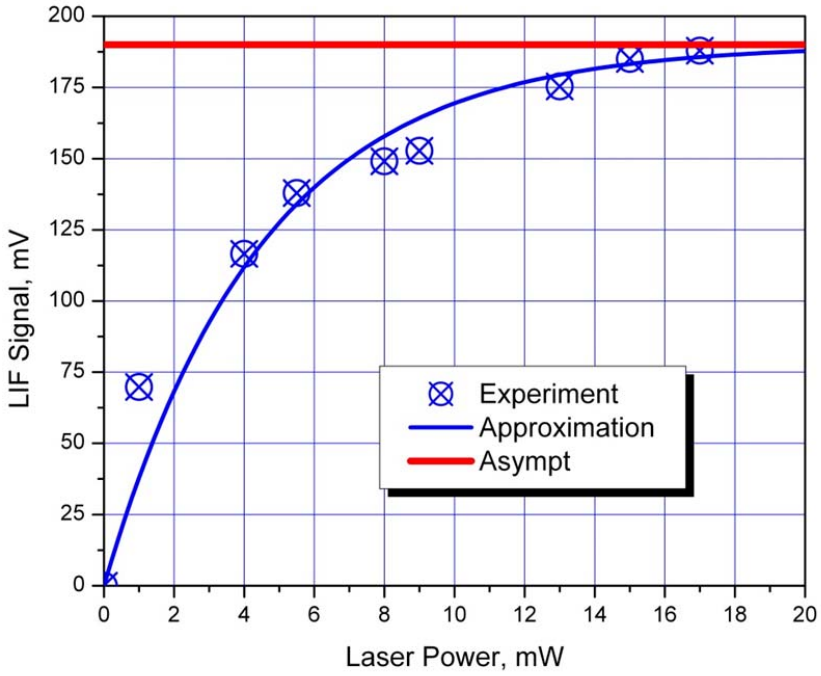

Figure 4.10 PMT LIF signal (315 nm) with increased laser power. Methane–air flame, P = 1 atm.

The ICCD camera with a 310-nm filter was used to capture the image of the OH LIF. Figure 4.11 shows that the OH LIF image appears upon activating the laser beam. The discharge channel shows a very weak OH signal at 310 nm from the discharge. When the laser is on, the fluorescence is induced in the middle of the discharge gap where the mixture is refreshed with the flow between the voltage pulses, and the discharge is rather uniform (axis of the discharge channel is vertical in Figure 4.11).

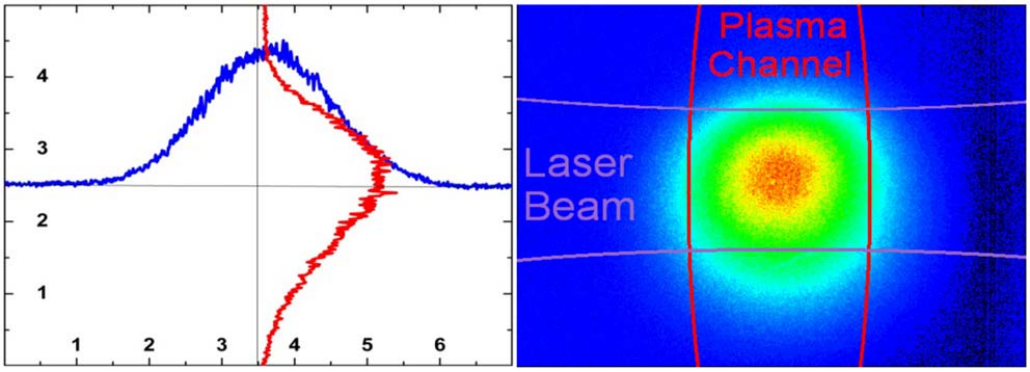

Figure 4.11 OH excitation LIF image. ICCD camera gate is 20 ns.
Image size is 7 × 5 mm.

The production of atomic oxygen in process (4.2) by direct electronic impact leads to the formation of a channel with very high initial concentration of radicals [87].

$$N_2(C^3) + O_2 = N_2(X^1) + O + O \quad \text{(R4.1)}$$

$$O_2 + e = O + O + e \quad \text{(R4.2)}$$

Important additional processes are those of fuel dissociation due to collisions with electrons and of the quenching of electronically-excited states of N_2 and O_2 [87]:

$$C_xH_y + e = C_xH_{y-1} + H + e \quad \text{(R4.3)}$$

$$C_xH_y + e = C_xH_{y-2} + H_2 + e \quad \text{(R4.4)}$$

…

$$C_xH_y + N_2^* = C_xH_{y-1} + H + N_2 \quad \text{(R4.5)}$$

$$C_xH_y + O_2^* = C_xH_{y-1} + H + O_2 \quad \text{(R4.6)}$$

Radical formation in the near-afterglow of the plasma channel initiates the chain reaction. The rates of chain propagation and chain branching reactions increase with increasing temperature. At low-temperature conditions, the chain termination and recombination reactions are prevalent.

The dynamics of time evolution of OH radicals is shown in Figure 4.12 and 4.13, where the abscissa is on a logarithmic scale. The OH LIF signal was integrated over the same volume as indicated in Figure 4.11. The calibration with ICCD camera (Figure 4.11) allows us to determine the volume of excited gas and to calculate absolute OH concentration. For these measurements, calibration was performed with a stoichiometric methane–air flame using the same PMT-based system. To accurately quantify the OH concentration, CRDS measurements have been performed and the results will be discussed in the following section.

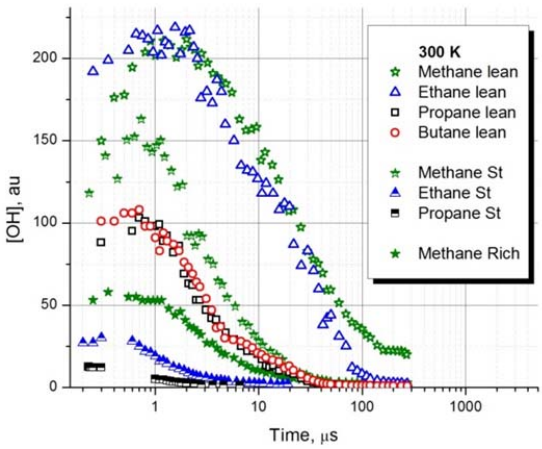

Figure 4.12 OH evolution over time at 300 K in hydrocarbon-air mixture. P = 1 atm. ϕ (lean) = 0.1, ϕ (st) = 1, ϕ (rich) = 4.

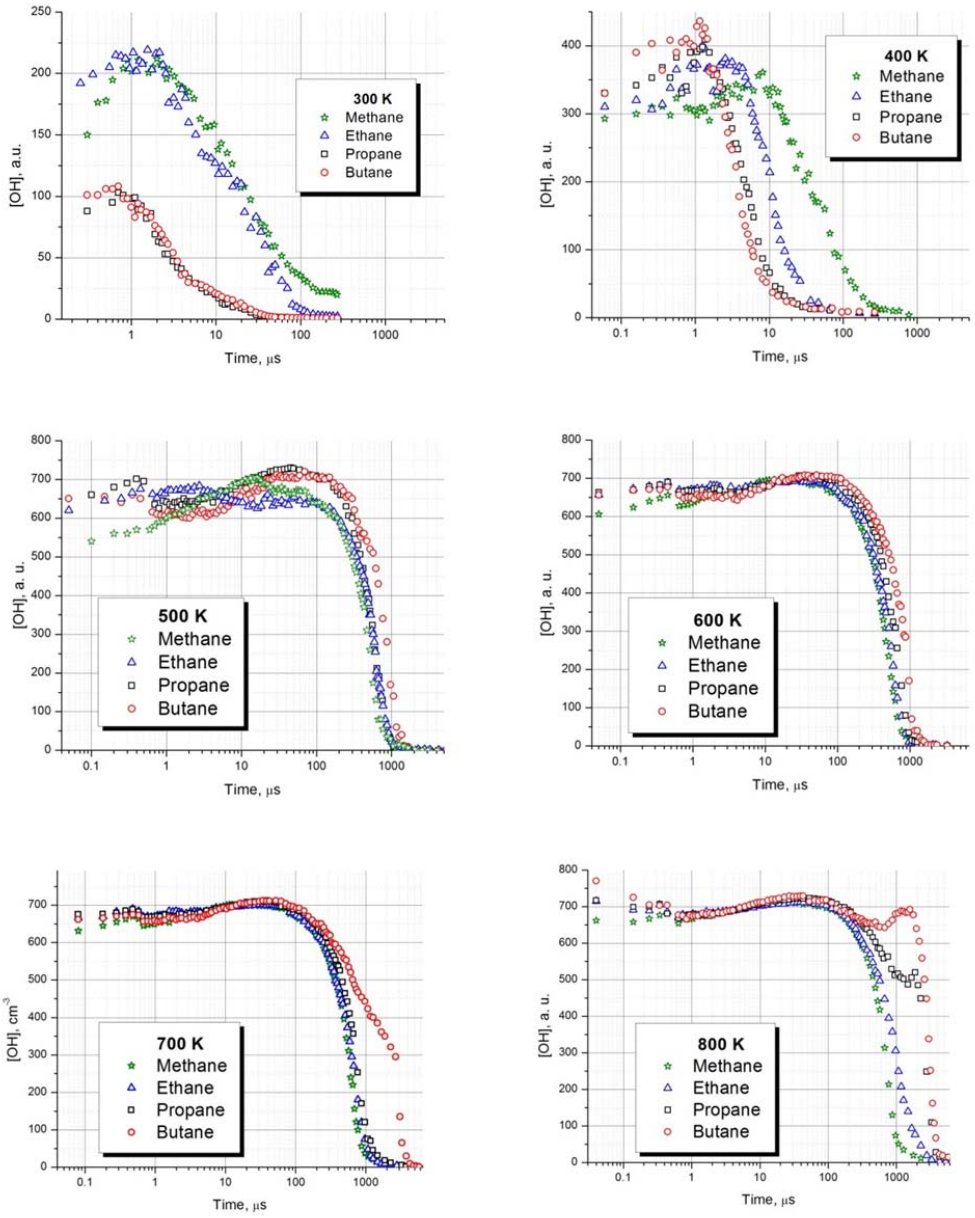

Figure 4.13 OH evolution over time at six temperature points (T = 300 – 800 K) in hydrocarbon-air mixture. P = 1 atm. $\phi = 0.1$

At 300 K, three different equivalence ratios were used (ϕ = 0.1, 1.0 and 3.0, Figure 4.12). The results can be easily interpreted. During the first microsecond, the electronically-excited species and ions are converted into radicals [87]. The rest of the process mostly consists of the recombination of the initial radicals. By comparing the [OH] degradation times among all curves, the methane curves (for all ϕ) are the longest, while those for butane appear to be the shortest. This behavior is related to the increasing reaction rate constants of $C_xH_y + OH = C_xH_{y-1}+H_2O$ for larger hydrocarbons. Moreover, by shifting a portion of fuels from lean to rich conditions, the [OH] degradation rate proportionally increases ($\tau_{0.1}/\tau_{3.0} \sim 8$).

The graph significantly alters when the temperature increases to 400 K. The methane curve shows that the time for [OH] to reach its maximum increases to about 10 μs. It should be noted that this value significantly exceeds the time of plasma recombination under atmospheric pressure conditions [87]. Thus, some chain propagation/ branching reactions may occur even at 400 K. The [OH] degradation order among the four fuels remains the same as at 300 K.

A drastic change occurs when the temperature rises to 500 K. The time of maximal [OH] remains in the range of 30–70 μs for all hydrocarbons under investigation. This major increase clearly demonstrates the chain development processes and OH generation continuation after the plasma channel recombination. The [OH] is depleted after approximately 1 ms, which is likely due to the rate increase of OH consumption reactions with accumulated intermediate products. Another noticeable change is the [OH] degradation order, which is now reversed compared to the previous figures.

At 600 K, the overall trend remains unchanged. The [OH] maximum becomes more pronounced in the time range of 30–80 μs. The graph begins to change again when the temperature reaches 700 K. A third stage of [OH] increase is observed at s > 1 ms. The third stage becomes clear at 800 K, where three maxima in [OH] concentration appear in a single curve.

The first peak may be related to the initial OH formation in the discharge, the second is likely due to chain reactions below the self-ignition threshold limited by the accumulation of intermediate species, and the third may correspond to the cool flame kinetics because it was only observed in butane and propane mixtures.

4.3.3 Time-resolved CRDS measurements of OH dynamics in the afterglow of the discharge

In the CRDS experiments, absolute concentrations of OH were calculated by relating the measured CRDS ringdown times (τ) to the molecule's (*A*) absorption coefficient (equation (4.1)) (Note: See Table 4.2 for a compilation of all the parameters used to calculate OH concentrations in equation (4.1)).

$$\alpha = [A]\sigma = (R_L/c)[1/\tau_R - 1/\tau_0] \quad (4.1)$$

R_L is the ratio of cavity length (L) to absorber length (ι), τ_o is the off resonance ring-down time, τ_R is the ring-down time on resonance, and c is the speed of light. The absorption cross section (σ) of the Q1(1) transition was calculated from the Einstein *B* coefficient [12] and was determined to be 5.08 x 10^{-16} cm^2 at 295 K. The absorption cross section

was then temperature corrected for experimental conditions (Table 4.3) by multiplying the molecule's known absorption cross section ($\sigma(T_R)$) by a continued product of the ratios of all temperature dependent terms (Eq. (4.2) & (4.3)). The Q's are the corresponding temperature dependent partition functions, SE is a stimulated emission correction, and $F''(J, K)$ is the rotational term value.

$$\sigma(T_F) = \sigma(T_R)\left[\frac{Q_{vib}(T_R)Q_{rot}(T_R)b_D(T_R)SE(T_F)}{Q_{vib}(T_F)Q_{rot}(T_F)b_D(T_F)SE(T_R)}\right]e^{\left[F''(J,K)\left(\frac{1}{T_R}-\frac{1}{T_F}\right)\frac{hc}{k_B}\right]} \quad (4.2)$$

Table 4.2 Molecular information used to temperature correct σ.

Radical	Vibrational Frequencies, (ν_n)		Rotational Constants		Rotational Term Value ($F''(J, K)$, cm^{-1})*, and Abs. Cross Section ($\sigma(T_R)$, cm^2)
	Mode	cm^{-1}	Term	cm^{-1}	
Hydroxyl (OH)	-	3735	B''	18.87	$F''(1) = 37.74$ $\sigma(295\ K) = 5.08\times10^{-16} cm^2$

$$^{*}F''(J,K) = J(J+1)\frac{(B''+C'')}{2} + \left[A'' - \left(\frac{B''+C''}{2}\right)\right]K^2$$

The exponential term in eq. (4.2) is a Boltzmann correction for a symmetric top molecule, which accounts for changes in the rotational population of a molecule with changes in temperature. Simplifying eq. (4.2) by factoring out all common terms yields eq. (4.3) for correcting a rovibrational absorption cross section for changes in temperature. All terms used to temperature correct σ (eq. (4.3)) are summarized in

$$\sigma(T_F) = \sigma(T_R) \frac{\prod_n \left[1 - e^{-\nu_n hc/k_B T_R}\right]^{-d_n}}{\prod_n \left[1 - e^{-\nu_n hc/k_B T_F}\right]^{-d_n}} \left[\frac{T_R}{T_F}\right]^2 \left[\frac{1 - e^{-h\omega_0/k_B T_F}}{1 - e^{-h\omega_0/k_B T_R}}\right] e^{\left[F''(J,K)\left(\frac{1}{T_R} - \frac{1}{T_F}\right)\frac{hc}{k_B}\right]} \quad (4.3)$$

Table 4.3 Parameters used in equation (4.2) to calculate OH concentrations in the afterglow of the plasma discharge. The on (τ_R) and off (τ_o) resonance ring-down times were extracted from a Gaussian fit of the data.

Plasma Discharge				
Temp. (K)	300		500	
σ (cm^2)	4.84 x 10^{-16}		1.76 x 10^{-16}	
L **(cm)**	50		50	
ι **(cm)**	0.2		0.2	
Delay (μs)	**τ_o (sec)**	**τ_R (sec)**	**τ_o (sec)**	**τ_R (sec)**
1	3.95 x 10^{-7}	1.47 x 10^{-7}	4.18 x 10^{-7}	1.89 x 10^{-7}
2	3.83 x 10^{-7}	1.53 x 10^{-7}	4.06 x 10^{-7}	1.89 x 10^{-7}
4	3.88 x 10^{-7}	1.63 x 10^{-7}	4.05 x 10^{-7}	1.75 x 10^{-7}
10	3.97 x 10^{-7}	1.89 x 10^{-7}	4.06 x 10^{-7}	1.74 x 10^{-7}
20	4.07 x 10^{-7}	2.27 x 10^{-7}	4.08 x 10^{-7}	1.87 x 10^{-7}
50	4.14 x 10^{-7}	2.95 x 10^{-7}	4.12 x 10^{-7}	2.74 x 10^{-7}
100	4.14 x 10^{-7}	3.55 x 10^{-7}	4.11 x 10^{-7}	3.45 x 10^{-7}
200	4.17 x 10^{-7}	3.94 x 10^{-7}	-	-

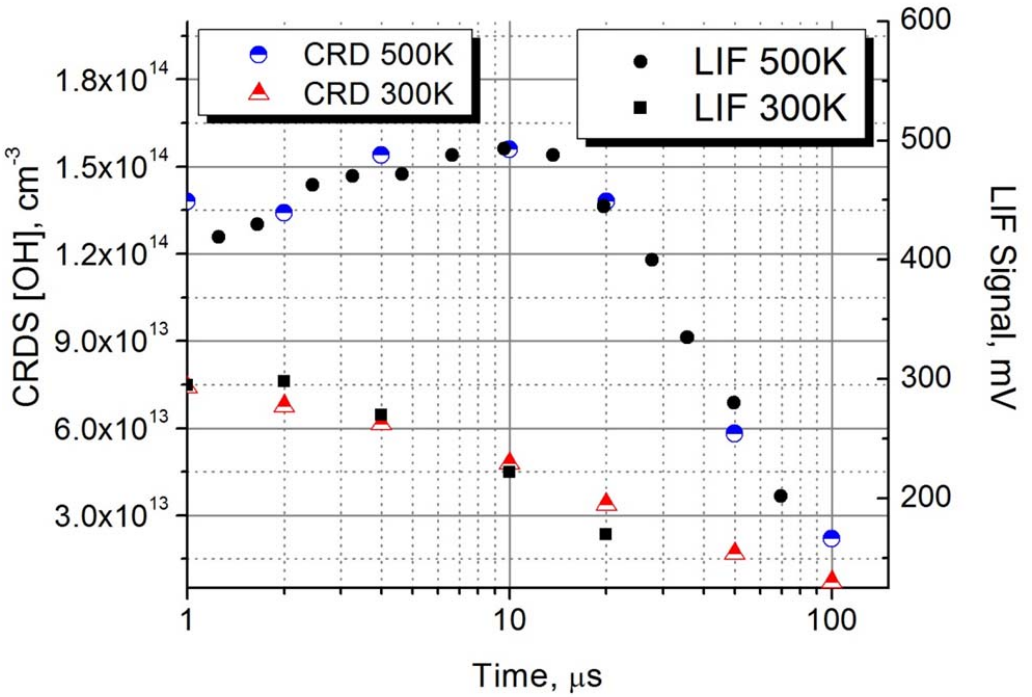

Figure 4.14 The comparison between experimental results from CRD spectroscopy and LIF at both 300 K and 500 K. The abscissa axis of time is in logarithmic scale.

The results from the CRDS were then compared with our previous saturated LIF results (Figure 4.14). The relative profile dynamics in LIF has an accuracy of ~5%, and the absolute accuracy of [OH] from CRDS measurement has a much better accuracy ~1%. The data from these two techniques are in very good agreement in predicting the dynamics of OH, confirming the validity of our previous results using saturated LIF. Moreover, the CRDS technique provides an accurate means of measuring absolute concentrations of OH in the afterglow of the discharge, which is essential for developing

accurate chemical kinetic models that can predict the enhanced combustion reactivity due to the plasma discharge.

4.3.4 Time-resolved PLIF measurements of OH dynamics in the afterglow of the discharge

With the PLIF technique, a spatially resolved OH distribution has been demonstrated. Figure 4.15 shows the false color PLIF images of OH dynamics at two temperatures, 300 K and 500 K. These spatially resolved OH images appear quite uniform along the discharge gap, which has been clearly illustrated by the intensity curve. By comparing this with the discharge emission dynamics in our previous work, we found the spatial similarity between the emission of excited nitrogen and OH radicals. This correspondence indicates that the excitation of nitrogen accounts for the production of atomic oxygen (O) and in turn formation of hydroxyl radical (OH). As demonstrated in [35, 87], the dissociative quenching of molecular oxygen through $N_2(C)$ and $N_2(B)$ is an important mechanism of production of atomic oxygen in nitrogen containing mixtures:

$$N_2(X^1) + e = N_2(B^3, C^3) + e \quad \text{(R4.7)}$$

$$N_2(B^3, C^3) + O_2 = N_2(X^1) + O + O \quad \text{(R4.8)}$$

In the afterglow of the plasma channel, the formation of radicals (particularly OH) initiates the chain reactions. The rates of chain propagation and chain branching reactions increase with increasing temperature, which can be shown through the comparison of results at 300 K and 500 K.

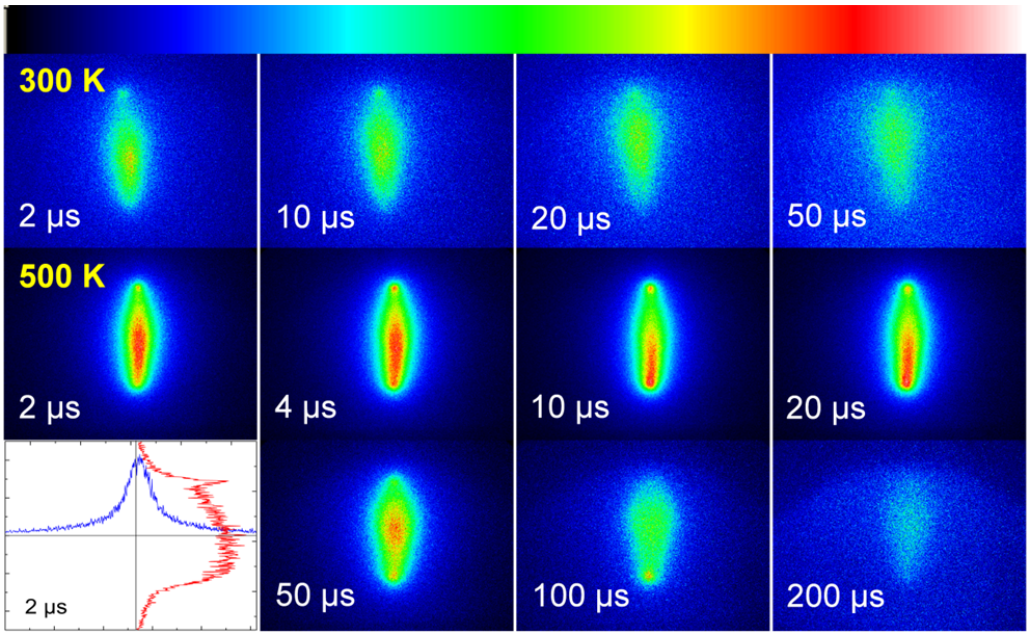

Figure 4.15 False-color sequenced PLIF images (PI-MAX ICCD camera) of OH dynamics in the afterglow of nanosecond pulsed discharge. The images in first row were taken at 300 K, and the others were at 500 K. The lower left is an intensity curve at 2 μs delay after the discharge. The number on each image stands for the delay between the discharge and the ICCD camera.

4.3.5 OH radical dynamics in H_2:air and H_2+CO:air mixtures

In the results of the previous section, the laser induced fluorescence (LIF) technique was employed to measure the time resolved hydroxyl (OH) radical in hydrocarbon-air mixtures in the afterglow of nanosecond pulsed plasma discharge. As hydrogen (H_2) and carbon monoxide (CO) oxidation mechanisms lie in the base of all hydrocarbon mechanisms, similar experiments have been performed in H_2:air and H_2+CO:air mixtures under similar conditions.

The dynamics of time evolution of OH radicals is shown in Figure 4.16, where the abscissa is on a logarithm scale. At 300 K, the whole curve can be divided into two parts. During the first microsecond, the electronically-excited species and ions are converted into radicals [87]. The rest of the process mostly consists of the recombination of the initial radicals. The difference between the two curves is due to the initial concentration of H_2 in the mixtures. However, the slopes of both decay curves appear very similar, which indicates the existence of CO does not affect the rate of OH degradation.

The drastic change occurs in H_2- and H_2/CO- air mixtures when the temperature rises to 400 K, comparing to 500 K, the transitional temperature for C_1-C_4 alkanes. The time of maximal [OH] remains in 20 to 50 μs for both gases under investigation. Unlike the OH dynamics in hydrocarbons as we presented before, the curves here could be clearly divided into three portions. The first part within 1 μs is the "plasma region", where the OH was generated from the quenching of electronically excited species and ions. The second regime is between 1 μs and ~30 μs, where OH increases monotonically to reach the maximum. This increase demonstrates the chain development process and OH generation continuation after the plasma channel recombination. The third part is the decay process of OH which lasts approximately 1 millisecond.

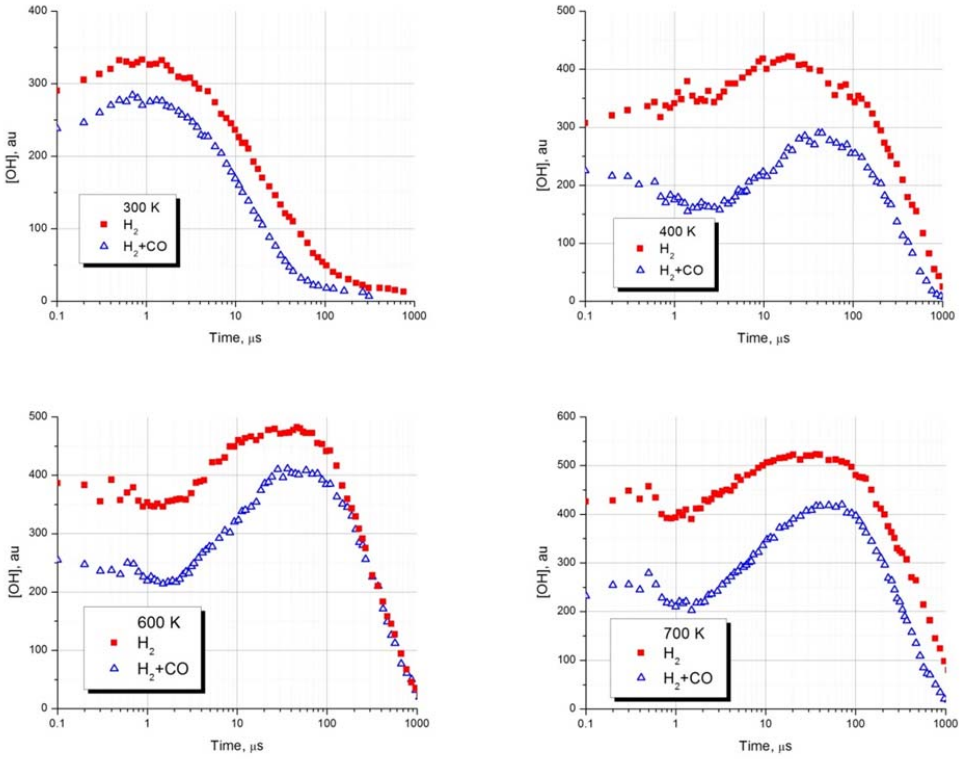

Figure 4.16 OH evolution over time at four temperature points (T = 300 – 700 K) in hydrogen-air and hydrogen/carbon monoxide-air mixture.
P = 1 atm. $\phi = 0.1$

Noticeably the shape and the lifetime almost remain the same among 400 K, 600 K and 700 K graphs, while [OH] levels differ.

4.4 Underlying Mechanism Study of Plasma Effect at Low Temperatures Below the Auto-ignition Threshold

Due to the lack of validated kinetic models in this temperature range, it is not possible to quantitatively explain all of the experimental data. All attempts with current available models fail to predict the aforementioned results.

Therefore, in order to reveal the key reaction pathways in low temperature regime, several questions need to be answered. First of all, the phenomena of the persistence of OH at low temperatures were observed in several different combustible mixtures, it is necessary to determine whether it is mainly due to the temperature increase (thermal effect) or enhanced chemical reactivity (chemical effect). Second, OH dynamics data in both hydrocarbon-air and hydrogen-air mixtures have a transitional temperature range (400 – 500 K for hydrocarbon-air, 300 – 400 K for hydrogen-air), where the OH lifetime increased one order of magnitude. For further numerical modeling, it is necessary to provide detailed experimental data in the transitional temperature range. Third, if the plasma thermal effect is eliminated, it will be crucial to identify the possible suspects of individual species playing the potentially crucial role in low temperature plasma-assisted ignition process.

4.4.1 Key Mechanism Investigation: Thermal Effect Study

In kinetic studies of almost all plasma assisted combustion research, local gas heating is always an important factor which cannot be neglected. Therefore, the plasma induced temperature increase was measured in this study as well.

Figure 4.17 shows the temperature results from optical emission spectroscopy (OES) and the thermocouple. By recording the emission of the second positive system of nitrogen molecules at 337.1 nm, the OES gives similar results to those obtained from the thermocouple data. At 300 K, the temperature measured by OES is approximately 342 K, which is roughly 40 K higher than the initial temperature. This shows that the non-thermal plasma does not raise the temperature of the fuel mixture significantly. Within the range of our experiments, the temperature increase does not exceed the auto-ignition threshold. The proposed experimental procedure can thus investigate the dynamics of OH formation and degradation in preheated chemically-active mixtures under strong non-equilibrium excitation in the temperature range below the auto-ignition threshold.

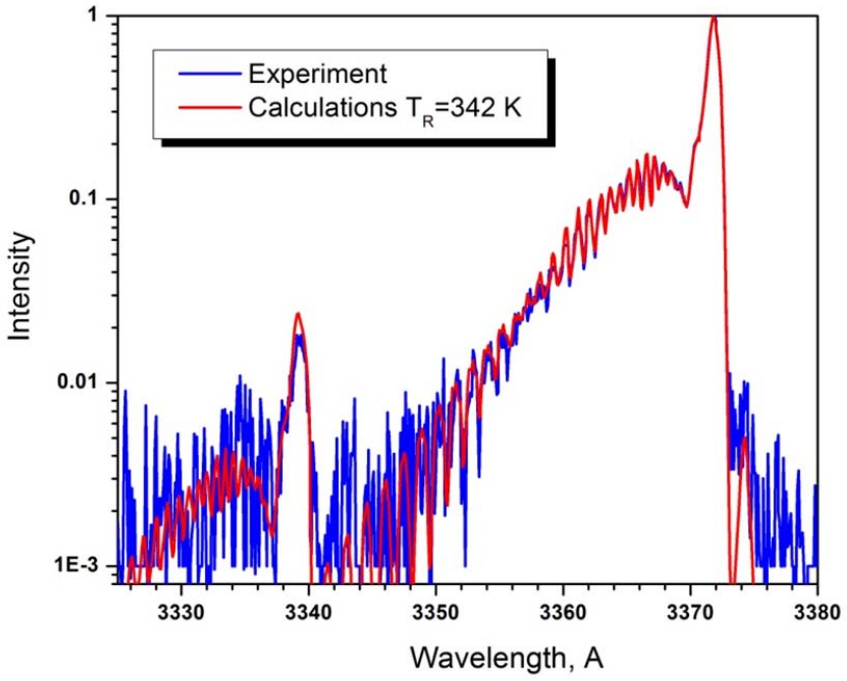

Figure 4.17 Rotational temperature measurement using emission of second positive system of N_2 molecules at 337.1 nm, T = 300 K (measured by thermocouple).

4.4.2 Detailed Measurements of OH radical dynamics

As shown in Figure 4.13 and Figure 4.16, apparently for all the mixtures there exists a "transitional range", which is 300 – 400 K for hydrogen-air and 400 – 500 K for C_1 to C_4 alkanes. Thus, Figure 4.18 is presented in order to compare the OH lifetime among multiple gas mixtures investigated. Here the OH lifetime is defined as the time when [OH] reaches 50% level as the maximum concentration. Three different gases have been

included, which are hydrogen, methane and butane. In addition, the calculated OH lifetime in hydrogen-air mixture based on the GRI-Mech 3.0 model, is presented for comparison.

The transitional threshold for all the gases is clearly demonstrated in Figure 4.18. Therefore, to further analyze the phenomena, additional measurements with fine temperature control around the threshold have been conducted, as seen in Figure 4.19 - Figure 4.21. For hydrogen, measurements have been accomplished between 300 K and 400 K; for butane, measurements were completed from 400 K to 500 K; for methane, measurements were conducted from 300 K to 500 K.

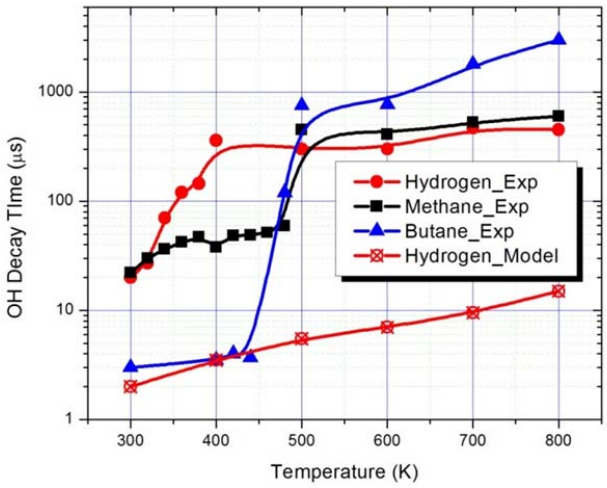

Figure 4.18 OH life time comparison among three different fuels, including hydrogen, methane and butane. The additional line presented here is from calculation based on current available chemical model of hydrogen.

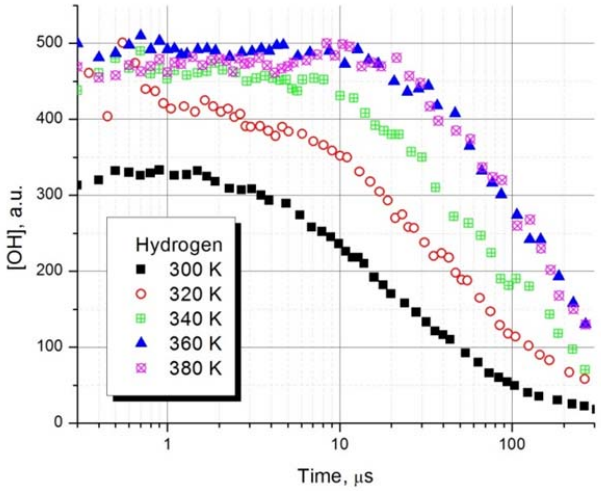

Figure 4.19 Detailed measurements of OH radical dynamics in H_2-air (ϕ = 0.1) mixture with small-temperature-step increase (T = 300 – 380 K).

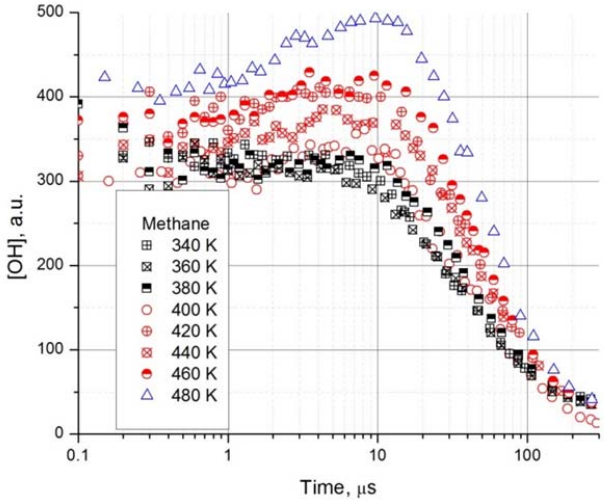

Figure 4.20 Detailed measurements of OH radical dynamics in CH_4-air ($\phi = 0.1$) mixture with small-temperature-step increase (T = 340 – 480 K).

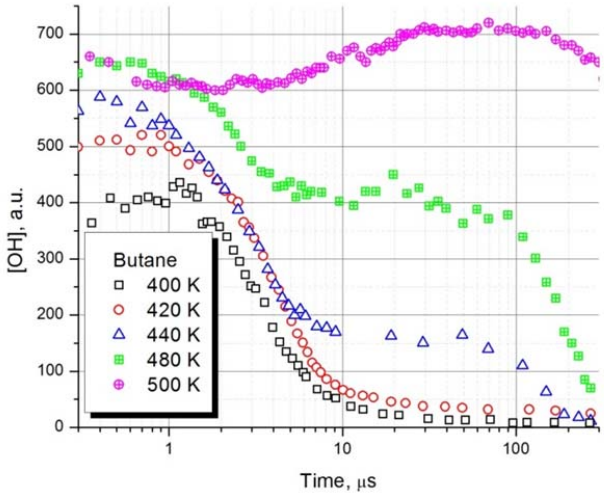

Figure 4.21 Detailed measurements of OH radical dynamics in n-C_4H_{10}-air ($\phi = 0.1$) mixture with small-temperature-step increase (T = 400 – 500 K).

Figure 4.19 - Figure 4.21 show a series of [OH] dynamics measurements with the temperature step of 20 K. Among the three graphs, one could easily tell the different behavior among these three gases. For hydrogen, the slope of OH decay curve gradually increases together with the temperature, and the same behavior was observed for methane. However, for butane, three dramatic increases appear between T = 400 K and 500 K. This may indicate that several reaction channels for OH production have been turned on with increasing temperature. Moreover, in Figure 4.19, for hydrogen-air mixture at temperature 340 K and above, the maximal [OH] peak appears at around 10 μs. In methane-air mixture, the [OH] peak shifts from 5 μs to 10 μs when temperature increases from 340 K to 480 K.

4.4.3 Chemical Effect Study: Role of Nitric Oxide in Plasma-assisted Ignition Below Auto-ignition Threshold

The results of the previous two sections have suggested that the major underlying mechanism is associated with plasma enhanced chemical reactivity. Thus, it becomes quite crucial to find out the major species and key reaction pathways which lead to the unique phenomena.

Whenever PAI is discussed the effect of nitric oxide (NO) generated in the plasma is raised. Approximately 20 years ago, researchers [88] found that the presence of small concentrations of nitric oxide (5-50 ppm) could significantly alter oxidation of hydrocarbons like butane in a flow reactor. This was also shown to be true in an engine

study of 1-pentene [89]. Increased NO production has indeed been detected in a methane-air mixture by a repetitive nanosecond pulsed discharge, and has been attributed to electronically excited metastable species reactions [46], [90]:

$$O + N_2^* \rightarrow NO + N \qquad \text{(R4.9)}$$

The effect of NO is a result of the competition between its promoting effect through reaction with HO_2 radicals and its retarding effect through reaction with OH radicals.

$$HO_2 + NO \rightarrow NO_2 + OH \qquad \text{(R4.10)}$$

$$NO + OH + M \rightarrow HONO + M \qquad \text{(R4.11)}$$

To study the effect of NO, a small amount of NO (50-100 ppm) was added into the gas mixtures to compare the OH production with previous results. If the promoting reaction with HO2 is dominant, the added NO will accelerate the reaction (4.10) and correspondingly OH will be further produced. On the other hand, the same level of OH production will indicate the role of NO is not significant in the plasma system.

By adding a small fraction of NO into the gas mixtures, [OH] measurements were made in two mixtures; CH_4-air and CH_4-air-NO at temperatures below the auto-ignition temperatures. Figure 4.22 shows OH concentration measurements in two sets of gas mixtures (CH_4-Air and CH_4-Air-NO) under two different temperature points (T = 300 K and 500 K). In room temperature, the two curves are almost the same, which indicates that NO does not have a noticeable effect at the doping concentrations evaluated. This situation remains when the temperature is raised to 600 K. Without major differences

among the two curves as observed in the graphs, NO seems unlikely to be the major species in enhancing the fuel oxidation and producing OH at low temperatures.

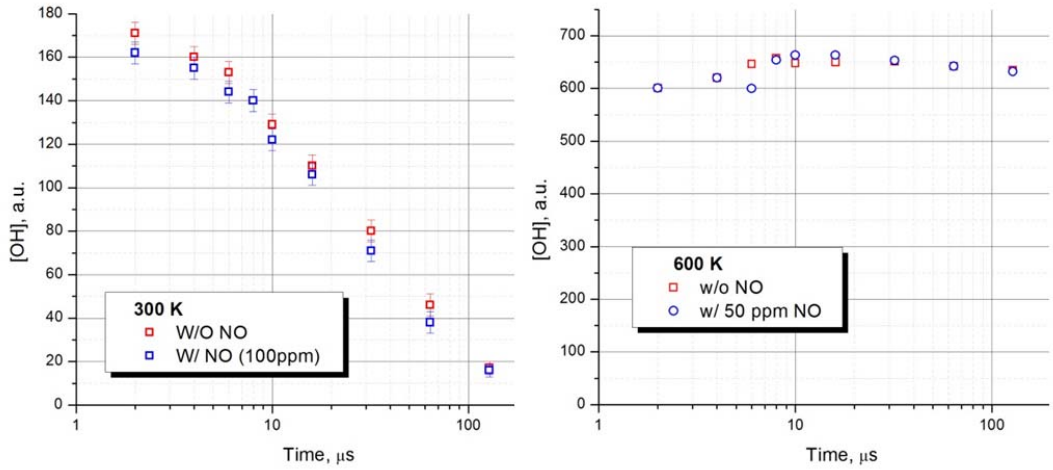

Figure 4.22 The comparison between experimental results from CH_4-air and CH_4-air-NO mixtures at 300 K (left) and 600 K (right). The abscissa axis of time is in logarithmic scale.

4.4.4 Chemical Effect Study: Role of $N_2(v)$ in Plasma-assisted Ignition Below Auto-ignition Threshold

A recent paper [91] has suggested that the key to the PAI at low temperatures is a mechanism that enhances the conversion of chemically dominant, but ultimately chain terminating, hydroperoxy radical (HO_2) to H, O, or OH. The author hypothesized that in an extremely non-equilibrium plasma system, the vibrational temperature of N_2 is far from equilibrium with the rest of the mixture $T_v > T_0$. Especially at under-critical reduced electric field (E/n ~ 80-100 Td), the main energy release occurs through vibrational excitation of the gas molecules. While vibrational relaxation of hydrocarbons is fast,

vibrationally excited hydrocarbons cannot accelerate chemical reaction. However, vibrationally excited nitrogen (N_2 $X^1\Sigma$ ($v > 0$), represented as $N_2(v)$) is particularly efficient at this E/n, which can induce an extended vibrational relaxation time of up to ~1ms in lean mixtures at ~500 K.

One possible path [2] involves a vibrationally excited N_2 molecule that accelerates the branching reaction of atomic hydrogen and molecular oxygen

$$H + O_2 + N_2(v) \rightarrow OH + O + N_2 \quad \text{(R4.12)}$$

The study [91] also proposed a model whereby $N_2(v)$ alters the oxidation chemistry at low-temperature via the sequence:

$$N_2(v = 1) + HO_2 \rightarrow N_2(v = 0) + HO_2(v2+ v3) \quad \text{(R4.13)}$$

$$HO_2(v2 + v3) \rightarrow H + O_2 \quad \text{(R4.14)}$$

Using a rough estimate of the rate parameters the author was able to reproduce the enhanced and extended plateau of previous experimental data, as shown in Figure 4.23. While the simulations are tantalizing exercises, further work is required before considering the case resolved.

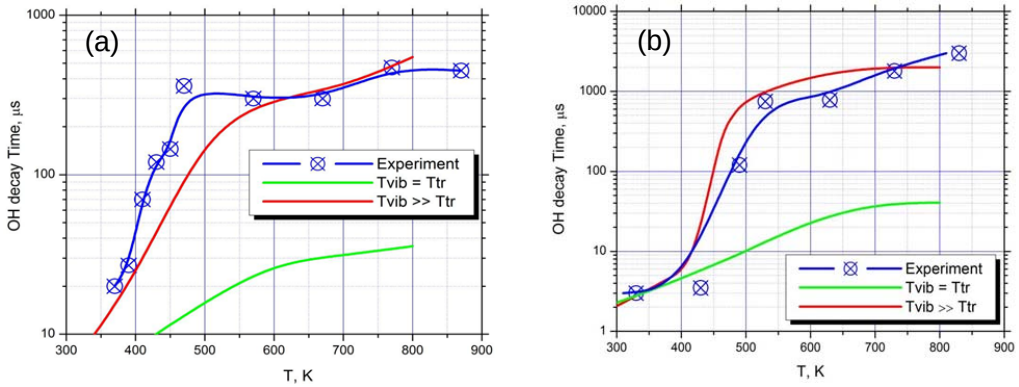

Figure 4.23 Measured and calculated OH decay time. a) 3%H_2 + air; b) 0.3%C_4H_{10} + air.

To investigate the hypothesis proposed based on simulations by Starikovskiy [91], experiments were conducted in the plasma reactor repeating measurements of OH in lean methane-air mixtures treated with the same nanosecond pulsed discharge; however, the N_2 was replaced in the air with CO_2, forming the synthetic air (20% O_2, 80% CO_2). The concentration and lifetime of OH radicals was measured with LIF and compared with our previous results. These comparisons provide an indication of whether or not $N_2(v)$ is the main cause for the long lifetime of OH (~1 ms) below the auto-ignition threshold. While simple to describe it is important to carefully match the previous conditions so that if negative results occur we can definitively rule out PAI from vibrationally excited molecular nitrogen.

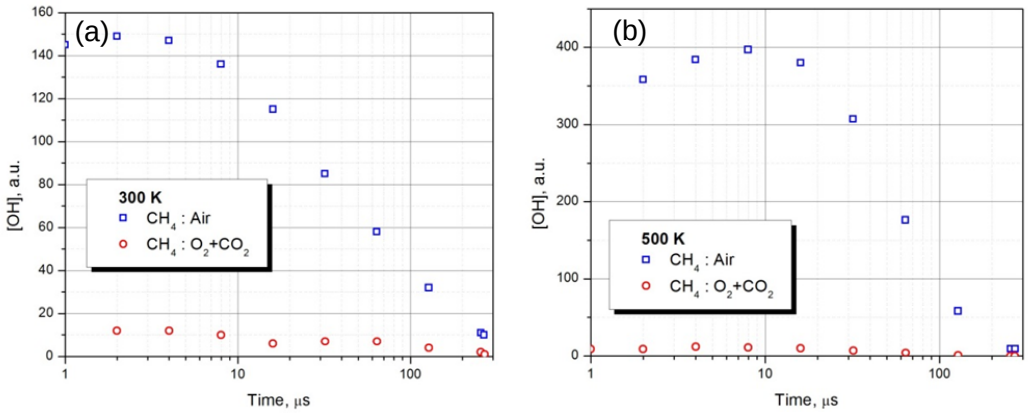

Figure 4.24 The comparison between experimental results from methane-air and from methane-synthetic air mixtures at 300 K (a) and 500 K (b). The abscissa axis of time is in logarithmic scale.

Results shown in Figure 4.24 show two sets of [OH] measurements under different temperatures in two lean mixtures (CH_4:N_2+O_2 (air) and CH_4:CO_2+O_2). At T = 300 K in CH_4:CO_2:O_2 mixtures, the [OH] profile starts at a surprisingly low concentration and quickly decays. In contrast, significant [OH] has been detected when the gas is switched to CH_4:air. The difference in [OH] is at least one order of magnitude. A similar result is observed when the temperature is increased to 500 K. In methane-air mixtures, a major increase in [OH] was observed, while [OH] continues to maintain at low levels without the presence of N_2.

The experimental data suggests that the role of N_2 seems to be critical in both producing the initial OH inside the plasma and sustaining the OH in the afterglow of the plasma. As seen from the graph, without N_2 in the gas mixture, the [OH] starts at an extremely low level. The drastic difference in [OH] has an obvious relationship with N_2. Of course, another interpretation of the results may associate CO_2 as an inhibiting species for OH production. Without available plasma chemical models, it is hard to separate the effect of

CO_2 and N_2 in the mixtures. However, the initial low OH production after the discharge with in the CH_4:O_2:CO_2 mixture can be explained through in lack of the key channels of atomic oxygen production, as shown in reaction (4.15).

$$N_2(B, C) + O_2 \rightarrow N_2 + O + O \qquad \text{(R4.15)}$$

These results have provided support of the kinetic analysis in reference [91]. The key mechanism of PAI below auto-ignition temperature is likely related to excited nitrogen species.

4.5 Closure

An experimental setup for plasma-assisted ignition kinetic analysis below the auto-ignition threshold was developed. The preheated gas mixture flow rate was in the range of 20–30 cm/s and guaranteed full mixture replacement between high-voltage pulses. Gas excitation was provided with the help of a pulsed nanosecond discharge in point-to-point geometry with a slightly-below-critical electric field. The OH concentration formed in the afterglow of a positive nanosecond discharge in the preheated hydrocarbon–air flow was measured via laser-induced fluorescence. Evidence was obtained for the existence of substantial oxidation chain lengths with discharge chain initiation by radical production from combustible mixtures at temperatures as low as 400–800 K. The extended OH lifetime was discovered at temperatures below auto-ignition threshold, while all the available combustion models failed to predict.

The results from the planar laser-induced fluorescence (PLIF) study confirmed the unique phenomena and also demonstrated uniform OH radical distribution along the discharge

channel. Comparison of OH radical emission dynamics with discharge emission dynamics from excited nitrogen revealed a close similarity in spatial distribution and allowed to clarify the mechanisms of atomic oxygen formation.

The cavity ring-down spectroscopy, a type of absorption spectroscopy, presented consistent results and further validated the unexpected experimental data.

Further investigation was focused on identification of the key underlying mechanisms of the phenomena. [OH] measurements were focused in the transitional range (300-400 K for hydrogen, 400-500 K for alkanes), where the OH lifetime increased by one to two orders of magnitude. The results reveal the distinguished behavior for different fuels due to the intrinsic differences of the fuel structure. On the other hand, temperature measurement was performed through optical emission spectroscopy of second positive nitrogen systems. The results ruled out the possibility of thermal effect being the major cause. Followed by this, the roles of both nitric oxide (NO) and vibrationally excited nitrogen ($N_2(v)$) were studied, respectively. The results reveal that $N_2(v)$ could be the key species affecting the major mechanism of plasma-assisted ignition below auto-ignition threshold.

Chapter 5 Summary, Conclusions and Recommendation

5.1 Research Summary and Conclusions

The research in this dissertation has focused on the study of fuel oxidation and ignition kinetics after the treatment by non-equilibrium plasma. Specifically, the physics and chemistry of plasma discharges have been studied both numerically and experimentally.

The numerical study of plasma discharges has compared the energy cost of active species generation by plasma under different conditions, and has demonstrated the optimal plasma parameters for discharges in different gas mixtures. Based on the analysis of chemical models, the role of singlet oxygen has been identified.

The experimental study has focused on the chemical kinetics of PAI below the auto-ignition threshold. Fast gated ICCD images were taken to show the uniform discharge development in air plasmas. Three types of laser diagnostics (laser induced fluorescence, planar laser induced fluorescence and cavity ring-down spectroscopy) have been applied to measure time-resolved [OH] dynamics in the afterglow of the nanosecond pulsed discharge. The unique phenomena of extended OH lifetime were observed in all the combustible mixtures (C_1 to C_4 alkanes, H_2, and H_2/CO) tested. All the currently available models failed to predict this behavior.

Additional efforts were directed towards identifying the key pathway in this low temperature regime. The results from temperature measurements through optical emission spectroscopy of second positive nitrogen system eliminated the possibility that the plasma raised the temperature of the mixture thus promoting this effect.

The impact of NO and $N_2(v)$ on PAI were explored in two series of experiments. In the first, OH profiles were monitored in mixtures of either CH_4-air or CH_4-air-NO (~1000 ppm) after plasma treatment. The OH profiles of these experiments were identical indicating that NO did not change the reactivity. In the second set of experiments, N_2 was replaced by CO_2 and the OH profiles were measured after plasma treatment. The OH concentration plateau disappeared indicating the critical role of N_2 in promoting reactivity. Further experiments are needed to identify the major pathways of OH production through reactions with excited nitrogen molecules.

5.2 Recommendations for Future Work

To further investigate the major reaction pathways of the plasma-assisted ignition below auto-ignition threshold, additional diagnostic techniques could be implemented to monitor the key radicals. For example, atomic oxygen (O) could be measured through Two-Photon Absorption Laser Induced Fluorescence (TALIF); atomic hydrogen (H) would be another candidate which can also be monitored by TALIF; vibrationally excited nitrogen molecules ($N_2(v)$), which could be the most important and interesting species in this study, may be measured via Coherent Anti-Stokes Raman spectroscopy (CARS). The measurement of these additional species should go a long way towards identifying the cause of this phenomenon. Such data could also be used to more fully develop and validate the chemical kinetics that controls the PAI. In addition, the future-developed chemical models could be validated with the detailed experimental data measured in this study.

List of References

[1] Yu.P. Raizer, Gas Discharge Physics, Springer-Verlag, Berlin, 1991.

[2] A. Fridman, Plasma Chemistry, Cambridge, 2008.

[3] A. Fridman and L. A. Kennedy, Plasma Physics and Engineering, New York: Taylor and Francis, 2004.

[4] S. M. Starikovskaia, "Plasma Assisted Ignition and Combustion", Journal of Physics D: Applied Physics, 39, 265-299, 2006.

[5] A. Starikovskiy, N. Aleksandrov, "Plasma-Assisted Ignition and Combustion", Progress in Energy and Combustion Science, 39, 61-110, 2013.

[6] A. Bourig, "Combustion Modification by Non-Thermal Plasma", PhD Thesis, Otto-von-Guericke University, 2009.

[7] Roth, J. R., Industrial Plasma Engineering, Volume 1: Principles, Taylor & Francis, 1995.

[8] W. Siemens, Ann. Phys. Chem. (Poggendorff's) 102, 66 (1857).

[9] U. Kogelschatz, "Dielectric-barrier Discharges: Their History, Discharge Physics, and Industrial Applications", Plasma Chemistry and Plasma Processing, 23, 1-46, 2003.

[10] J.J. Thomson, Recent researches in electricity and magnetism, Oxford: Clarendon, p.115, 1893.

[11] D.L. Carroll, J.T. Verdeyen, D.M. King, J.W. Zimmerman, J.K. Laystrom, B.S. Woodard, G.F. Benavides, K. Kittell, D.S. Stafford, M.J. Kushner, and W.C. Solomon, "Continuous-Wave Laser Oscillation on the 1315 nm Transition of Atomic Iodine pumped by O2(a1Δg) Produced in an Electric Discharge", Applied Physics Letter, 86, 111104, 2005.

[12] D.L. Carroll, J.T. Verdeyen, D.M. King, J.W. Zimmerman, J.K. Laystrom, B.S.Woodard, G.F. Benavides, K.W. Kittell, and W.C. Solomon, "Path to the Measurement of Positive Gain on the 1315-nm Transition of Atomic Iodine Pumped by O2(a1Δ) Produced in an Electric Discharge", IEEE Journal of Quantum Electronics, vol. 41, 2005, pp. 213-223.

[13] M. Nishihara, J.W. Rich, W.R. Lempert, I.V. Adamovich, and S. Gogineni, "Low-Temperature M=3 Flow Deceleration by Lorentz Force", Physics of Fluids, 18(8), p. 086101, 2006.

[14] G. Lou, A. Bao, M. Nishihara, S. Keshav, Y. G. Utkin, and I. V. Adamovich, "Ignition of Premixed Hydrocarbon-Air Flows by Repetitively Pulsed, Nanosecond Pulse Duration Plasma", AIAA Paper 2006-1215, 2006.

[15] D. Galley, G. Pilla, D. Lacoste, S. Ducruix, F. Lacas, D. Veynante, C. O. Laux, "Plasma-enhanced combustion of lean premixed air-propane turbulent flame, using a nanosecond repetitively pulsed plasma", AIAA Paper 2005-1193, 2005.

[16] W.S. Choi, Y. Neumeier, J. Jagoda, "Stabilization of a combustion process near lean blow off (LBO) by an electric discharge", AIAA Paper 2004-982, 2004.

[17] D. Han, M.G. Mungal, "Simultaneous measurement of velocity and CH layer distribution in turbulent non-premixed flames", Proc. Combust. Inst., 28, p. 261-267, 2001.

[18] L. Muñiz, M.G. Mungal, "Effects of heat release and buoyancy on flow structure and entrainment in turbulent nonpremixed flame", Combustion and Flame, 126(1-2): p. 1402-1420, 2001.

[19] C.D. Carter, J.M. Donbar, J.F. Driscoll, "Simultaneous CH-PIV imaging of turbulent nonpremixed flames", Appl. Phys. B, 1998. 66(1): p. 129-132.

[20] S. Prakash, S. Nair, T.M. Muruganandam, Y. Neumeier, T. Lieuwen, J. Seitzman, B.T. Zinn, "Acoustic sensing and mitigation of lean blow out in premixed flames", AIAA Paper 2005-1420. 2005.

[21] S. Tachibana, S. Zimmer, Y. Kurosawa, K. Suzuki, "The effects of location of secondary fuel injection on the suppression of combustion oscillation", 2nd Asian Joint Conference on Propulsion and Power. 2005: Kitakyushu, Japan.

[22] R.W. Schefer, M. Namazian, J. Kelly, "Velocity measurements in a turbulent nonpremixed bluff-body stabilized flame", Combust. Sci. Technol., 1987. 56(4-6): p. 101-138.

[23] D.T. Yegian, R.K. Cheng, "Development of a lean premixed low swirl burner for low NOx practical applications", Combust. Sci. Technol., 1998. 139(1-6): p. 207-227.

[24] S. Archer, A.K. Gupta, "The role of confinement on flow dynamics under fuel lean combustion conditions", 2nd International Energy Conversion Engineering Conference, 2004.

[25] H.F. Calcote, “Electrical properties of flames: burner flames in transverse electric fields”, Proc. Combust. Inst., 1949. 3(1): p. 245-253.

[26] H.F. Calcote, C.H. Berman, “Increased methane-air stability limits by a DC electric field”, in Fossil Fuel Combustion Symposium. 1989, p.25-31: Houston, Texas.

[27] M.L. Polanyi, G.H. Markstein, “Phenomena in electrically and acoustically disturbed flames”, in Project SQUID Technical Report, Laboratory Cornell Aeronautical, Editor. 1947.

[28] G.P. Tewari, J.R. Wilson, “Experimental study of the effects of high frequency electric fields on laser-induced flame propagation”, Combustion and Flame, 1975. 24(2): p. 159-167.

[29] C.S. Maclatchy, R.M. Clements, P.R. Smy, “An experimental investigation of the effect of microwave radiation on a propane-air flame”, Combustion and Flame, 1982. 45: p. 161-169.

[30] S.H. Won, M.S. Cha, C.S. Park, S.H. Chung, “Effect of electric fields on reattachment and propagation speed of tribrachial flames in laminar coflow jets”, Proc. Combust. Inst., 2007. 31: p. 963-970.

[31] F.J. Weinberg, K. Hom, A.K. Oppenheim, K. Teichman, “Ignition by plasma-jet”, Nature, 1978. 272: p. 341-343.

[32] F.B. Carleton, I.M. Vince, F.J. Weinberg, “Structure and extinction of near-limit flames in a stagnation flow”, Proc. Combust. Inst., 1983. 19: p. 1523-1531.

[33] A.J.J. Lee, F.J. Weinberg, “A novel ignition device for the internal combustion engine”, Nature, 1984. 311: p. 738-740.

[34] S.A. Bozhenkov, S.M. Starikovskaia, A.Yu. Starikovskii, “Nanosecond gas discharge ignition of H2 and CH4 containing mixtures”, Combustion and Flame, 2003. 133: p. 133-146.

[35] E.I. Mintoussov, S.V. Pancheshnyi, A.Y. Starikovskii, “Propane-air flame control by nonequilibrium low temperature pulsed nanosecond barrier discharge”, AIAA Paper 2004-1013, 2004

[36] D. Galley, G. Pilla, D. Lacoste, S. Ducruix, F. Lacas, D. Veynante, C.O. Laux, “Plasma enhanced combustion of a lean premixed air-propane turbulent flame using a nanosecond repetively pulsed plasma”, AIAA Paper 2005-1193. 2005.

[37] S. Pancheshnyi, D. Lacoste, A. Bourdon, C.O. Laux, “Propane-air mixtures ignition by a sequence of nanosecond pulses”, in European Conference for Aerospace Sciences. 2005: Moscow, Russia.

[38] S.M. Starikovskaia, I.N. Kosarev, A.V. Krasnochub, E.I. Mintoussov, A.Y. Starikovskii, “Control of combustion and ignition of hydrocarbon-containing mixtures by nanosecond pulsed discharges”, AIAA Paper 2005-1195, 2005.

[39] A.Yu. Starikovskii, “Plasma supported combustion”, Proc. Combust. Inst., 2005. 30(2): p. 2405-2417.

[40] E.I. Mintoussov, A.A. Nikipelov, S.M. Starikovskaia, A.Yu. Starikovskii, “Rapid Combustion Achievement by Nanosecond Barrier Discharge”, AIAA Paper 2006-614, 2006.

[41] G. Lou, A. Bao, M. Nishihara, S. Keshav, Y.G. Utkin, I.V. Adamovich, “Ignition of ethylene–air and methane–air flows by low-temperature repetitively pulsed nanosecond discharge plasma”, in 44th AIAA Aerospace Sciences Meeting and Exhibit. 2006: Reno, NV.

[42] N. Chintala, A. Bao, G. Lou, I.V. Adamovich, “Measurements of combustion efficiency in nonequilibrium RF plasma-ignited flows”, Combustion and Flame, 2006. 144(4): p. 744-756.

[43] S.M. Starikovskaia, N.B. Anikin, I.N. Kosarev, N.A. Popov, A.Yu. Starikovskii, “Analysis of ignition by nonequilibrium sources. Ignition of homological series of hydrocarbons by volume nanosecond discharge”, in 44th AIAA Aerospace Sciences Meeting and Exhibit. AIAA 2006-616. 2006: Reno, NV.

[44] E.I. Mintoussov, E.Y. Svetlana, A.A. Nikipelov, S.S. Starikovskaia, A.Yu. Starikovskii, “Plasma chemical processes in plasma-assisted combustion”, AIAA Paper 2007-1354. 2007.

[45] N.A. Popov, I.A. Kossyi, “Effect of nonequilibrium excitation of hydrogen-oxygen mixture on ignition”, AIAA Paper 2007-1031. 2007.

[46] W. Kim, H. Do, M.G. Mungal, M.A. Cappelli, “Investigation of NO production and flame structure in plasma enhanced premixed combustion”, Proc. Combust. Inst., 2007. 31(2): p. 3319-3326.

[47] W. Kim, H. Do, M.G. Mungal, M.A. Cappelli, “Plasma-discharge stabilization of jet diffusion flames”, IEEE Trans. Plasma Sci., 2006. 34(6): p. 2545-2551.

[48] W. Kim, H. Do, M.G. Mungal, M.A. Cappelli, “Optimal discharge placement in plasma assisted combustion of a methane jet in cross flow”, Combustion and Flame, 2008. 153: p. 603-615.

[49] A.M. Warris, F. Weinberg, “Ignition and flame stabilization by plasma jets in fast gas streams”, Twentieth Symposium (International) on Combustion, 1984: p. 1825-1831.

[50] C. Laux, G. Pilla, S. Pancheshnyi, D. Pai, L. Caillault, D. Lacoste, A. Bourdon, D. Veynante. “Plasma-assisted combustion using nanosecond repetitively pulsed discharges”, in Proceedings of the XXVIII International Conference on Phenomena in Ionized Gases. 2007. Czech Republic.

[51] G. Pilla, D. Galley, D. Lacoste, F. Lacas, D. Veynante, C. Laux, “Stabilization of a turbulent premixed flame using a nanosecond repetitively pulsed plasma”. IEEE Transactions on Plasma Science, 2006. 34(1): p. 2471-2477.

[52] S.A. Bozhenkov, S.M. Starikovskaia, A.Y. Starikovskii, “Deflagration-to-detonation control by non-equilibrium gas discharges and its applications for pulsed detonation engine”, in Moscow Institute of Physics and Technology Reports, Dolgoprudny, Russia.

[53] A. Klimov, V. Brovkin, V. Bityurin, V. Vinogradov, D. VanWie, “Plasma assisted combustion”, AIAA Paper 2001-0491, 2001.

[54] A.Y. Starikovskii, “Initiation of ignition by the action of a high-current pulsed discharge on a gas”. Combustion, Explosion and Shock Waves, 2003. 39(6): p. 619-626.

[55] V.P. Zhukov, V.A. Sechenov, A.Y. Starikovskii, “Spontaneous ignition of methane-air mixtures in a wide range of pressures”. Combustion, Explosion, and Shock waves, 2003. 39(5): p. 487-495.

[56] N. Chintala, R. Meyer, A. Hicks, B. Bystricky, J.W. Rich, W.R. Lempert, I.V. Adamovich, Non-thermal ignition of premixed hydrocarbon-air and CO-air flows by nonequilibrium RF plasma, in 42nd AIAA Aerospace Sciences Meeting and Exhibit, AIAA 2004-0835. 2004: Reno, Nevada.

[57] G. Lou, A. Bao, M. Nishihara, S. Keshav, Y.G. Utkin, J. William, W.R. Lempert, I.V. Adamovich, “Ignition of premixed hydrocarbon-air flows by repetitively pulsed, nanosecond pulse duration plasma”. Proc. Comb. Inst., 2007. 31: p. 3327-3334.

[58] L.A. Rosocha, D.M. Coates, D. Platts, S. Stange, “Plasma-enhanced combustion of propane using a silent discharge”. Physics of plasmas, 2004. 11(5).

[59] S. Pancheshnyi, D. Lacoste, A. Bourdon, C. Laux, "Ignition of propane-air mixtures by a repetitively pulsed nanosecond discharge". IEEE Transactions on Plasma Science, 2006. 34(1): p. 2478-2487.

[60] A.V. Krasnochub, E.I. Mintoussov, M.M. Nudnova, A.Y. Starikovskii, "Flame blow-off velocity control: the importance of proper organization of nanosecond barrier discharge". XXVIIth ICPIG, Eindhoven, the Netherlands, 2005.

[61] J. J. Dutton, "A survey of electron swarm data", Phys. Chem. Ref. Data, 4, 577, 1975.

[62] L.G.H. Huxley, R.W. Crompton, The Diffusion and Drift of Electrons in Gases New York: Wiley-Interscience, 1974.

[63] Babich L.P. "Analysis of a new electron runaway mechanism and record-high runaway electron currents supposedly achieved in dense gas discharges". Sov. Phys. Usp., vol. 48 (10), 2005.

[64] L.C. Pitchford, B.V. McKoy, A. Chutjian, S. Trajmar, Swarm Studies and Inelastic Electron-Molecule Collisions, Springer-Verlag, New York, 1987, pp.167–187.

[65] A.A Ionin, I.V. Kochetov, A.P. Napartovich, N.N. Yuryshev, "Physics and engineering of singlet delta oxygen production in low-temperature plasma", Journal of Physics D: Applied Physics, 40, R25-R61, 2007.

[66] K. Tachibana, "Excitation of the 1s5,1s4, 1s3, and 1s2 levels of argon by low-energy electrons", Physics Review A, 34, 1007-1015, 1986.

[67] L.S. Polak, Yu A Lebedev, Plasma chemistry, Cambridge International Science Publishing, 1998.

[68] E.A. Kovach, S.A. Losev, A.L. Sergievskaia, N.A. Khrapak, "Models for physical-chemical processes. 3. Thermally-equilibrium and nonequilibrium chemical reactions". Physical and Chemical Kinetics in Gasdynamics MSU; 2010.

[69] I.V. Adamovich, S.O. Macheret, J.W. Rich, C.E. Treanor, A.A. Fridman, "Molecular physics and hypersonic flows". Kluwer Academic Publishers, 1996.

[70] S.O. Macheret, A.A. Fridman, I.V. Adamovich, J.W. Rich, C.E. Treanor, "Mechanisms of nonequilibrium dissociation of diatomic molecules". AIAA-Paper 1994-1984. 1994.

[71] C. Park, “Two-temperature interpretation of dissociation rate data for N_2 and O_2”, AIAA-Paper 1988-0458, 1988.

[72] Losev SA, Sergievskaia AL, Rusanov VD, Fridman AA, Macheret SO. Reports of Russian Academy of Science 1996;346(2):192.

[73] G.J.M. Hagelaar and L.C. Pitchford, "Solving the Boltzmann equation to obtain electron transport coefficients and rate coefficients for fluid models", Plasma Sources Sci. Technol. 14 722-733 (2005).

[74] V.V. Smirnov, O.M. Stelmakh, V.I. Fabelinsky, D.N. Kozlov, A.M. Starik, N.S. Titova, “On the influence of electronically excited oxygen molecules on combustion of hydrogen-oxygen mixture”, Journal of Physics D: Applied Physics, 41, 192001 (6 pp.), 2008.

[75] A.U. Khan, M. Kasha, “Direct spectroscopic observation of singlet oxygen emission at 1268 nm excited by sensitizing dyes of biological interest in liquid solution”, Proceedings of the National Academy of Sciences, 76, 6047-6049, 1979.

[76] C.W. McCluskey, “The search for metastables and molecular ions in discharges”. Ph.D thesis, University of Texas at Austin. 2002.

[77] C. Yamabe, A.V. Phelps, “Excitation of the O_2(a1Δg) state by low energy electrons in O_2-N_2 mixtures”. J. Chem. Phys, 78(6): p. 2984-2989, 1983.

[78] L.R. Martin, R.B. Cohen, J.F. Schatz, “Quenching of laser induced fluorescence of $O_2(b^1\Sigma^+_g)$ by O_2 and N_2”. Chemical Physics Letters, 41(2): p. 394-396, 1976.

[79] L.T. Cupitt, G.A. Takacs, G.P. Glass, “Reaction of hydrogen atoms and $O_2(a^1\Delta_g)$”, International Journal of Chemical Kinetics, 14: p. 487-497, 1982.

[80] A. A. Ionin, Y. M. Klimachev, A. A. Kotkov, I. V. Kochetov, A. P. Napartovich, L. V. Seleznev, D. V. Sinitsyn, and G. D. Hager, “Non-self-sustained electric discharge in oxygen gas mixtures: singlet delta oxygen production”. J. Phys. D : Appl. Phys., 2003. 36: p. 982-989.

[81] A. Bourig, V. Lago, J.P. Martin, K. Pliavaka, F. Pliavaka, S. Gorbatov, Generation of singlet oxygen in HV pulsed + DC crossed discharge at atmospheric pressure for oxygen-enhanced combustion. International Journal of Plasma Environmental Science and Technology, 2007. 1(1): p. 57-63.

[82] A.M. Starik, N.S. Titova, B.I. Loukhovitski, “Laser-induced excitation of target molecules as an efficient approach to control the combustion and technological chemical processes”, International Conference on Lasers, Applications and Technologies. Proceedings of SPIE, 2005. 6053: p. 1-10.

[83] S.N. Foner, R.L. Hudson, “Metastable oxygen molecules produced by electrical discharges”. J. Chem. Phys., 1956. 25(3): p. 601-602.

[84] A. P. Napartovich, A. Deryugin, and I. Kochetov, “Discharge production of the singlet delta oxygen for an iodine laser”. J. Phys. D: Appl. Phys., 2001. 34: p. 1827-1833.

[85] A.M. Starik, N.S. Titova, “Kinetics of Detonation Initiation in the Supersonic Flow of the H2 + O2 (Air) Mixture in O2 Molecule Excitation by Resonance Laser Radiation”. Kinetics and Catalysis, 44 (1) (2003) 28–39.

[86] Popov N.A. “Effect of a Pulsed High-Current Discharge on Hydrogen–Air Mixtures”. Plasma Physics Reports, 2008, vol. 34, No. 5, pp. 376–391.

[87] N.L. Aleksandrov, S.V. Kindysheva, I.N. Kosarev, S.M. Starikovskaia, A.Yu. Starikovskii, “Mechanism of ignition by non-equilibrium plasma”, Proc. Comb. Inst. 32 (2009) 205–212.

[88] J.H. Bromly, F.J. Barnes, R. Mandyczewsky, T.J. Edwards, B.S. Haynes, “An experimental investigation of the mutually sensitised oxidation of nitric oxide and n-butane,” Proc. Comb. Inst., 1992. 24: p. 899-907.

[89] S.K. Prabhu, R.K. Bhat, D.L. Miller, N.P. Cernansky, “1-Pentene oxidation and its interaction with nitric oxide in the low and negative temperature coefficient regions,” Combustion and Flame, 104, 377-390.

[90] M. Uddi, N. Jiang, I.V. Adamovich, W.R. Lempert, “Nitric oxide density measurements in air and air/fuel nanosecond pulse discharges by laser induced fluorescence,” J. Phys. D: Appl. Phys., 075205.

[91] A. Yu. Starikovskiy, “Kinetics of plasma-assisted oxidation and ignition below self-ignition threshold,” AIAA-paper 2012-0244

[92] K.C. Smyth and D.R. Crosley, “Detection of Minor Species with Laser Techniques”, in Applied Combustion Diagnostics, K.K. Hoinghaus and J.B. Jeffries, Editors, Taylor and Francis, NY, 2002.

[93] A. C. Eckbreth, Laser Diagnostics for Combustion Temperature and Species, Gordon and Breach Publishers, the Netherlands, 1996.

[94] A. O'Keefe, D.A.G. Deacon, “Cavity ring-down optical spectrometer for absorption measurements using pulsed laser sources”, Rev. Sci. Instrum., 59:2544 -2551, 1988.

[95] J.J. Scherer, J.B. Paul, A. O'Keefe, R.J. Saykally, “Cavity ring-down laser absorption spectroscopy: history, development, and application to pulsed molecular beam”, Chem. Rev., 97:25-51, 1997

[96] C. Laux, "Radiative and Non-Equilibrium Collisional-Radiative Models," in von Karman Institute Special Course on Physico-chemical Modeling of High Enthalpy and Plasma Flows, Rhose-Saint-Genesem Belgium, 2002.

[97] A. Chelouah, E. Marode, G. Hartmann, and S. Achat, "A New Method for Temperature Evaluation in a Nitrogen Discharge," J. Phys. D: Appl. Phys., vol. 27, pp. 940-945, 1994

Appendix: Optical Diagnostics

Laser-induced Fluorescence (LIF)

Laser-induced fluorescence is a classic spectroscopic technique used for detection of selective species. The atom or molecule is excited with an appropriate narrowband laser from a specific quantum (rotational, vibrational, electronic) state into an energetically higher quantum state. The wavelength is often selected to be the one at which the species has its largest cross section. Subsequently, usually after a few nanoseconds, the excited species will emit fluorescence radiation at a wavelength longer than the excitation wavelength. This fluorescent light is typically recorded with a photomultiplier tube (PMT). LIF is exceedingly flexible and has been used, for example, for detection of more than thirty trace combustion radical species.

Focusing on the energy level diagram for hydroxyl (OH) radical, shown in Figure A-1, the absorption of single photon at 283 nm results in excitation of a fraction of the total number of radicals from the initial ground $X^2\Pi$ electronic state to the excited $A^2\Sigma$ state (1st excited upper electronic state), a fraction of which subsequently decay to the ground electronic state either by fluorescence or by quenching. LIF signal results from radiative relaxation, where the excess energy is released in terms of fluorescent photons. Non-radiative relaxation pathways compete with LIF, and their magnitude and impact are of great importance for quantitative interpretation of the signal. Vibrational levels are shown in Figure A-1 with horizontal lines in each electronic state, and the rotational manifold

attached to relevant v'=1 vibrational state are magnified in the right green dotted box. Once the OH radical is excited to a specific rovibrational energy level in the upper electronic state, it can migrate to neighboring energy levels or back down to the lower electronic state via several energy transfer pathways. The relevant energy transfer mechanisms are indicated with arrows and include absorption, stimulated emission, spontaneous emission, collisional quenching also known as electronic energy transfer, rotational energy transfer (RET) and vibrational energy transfer (VET).

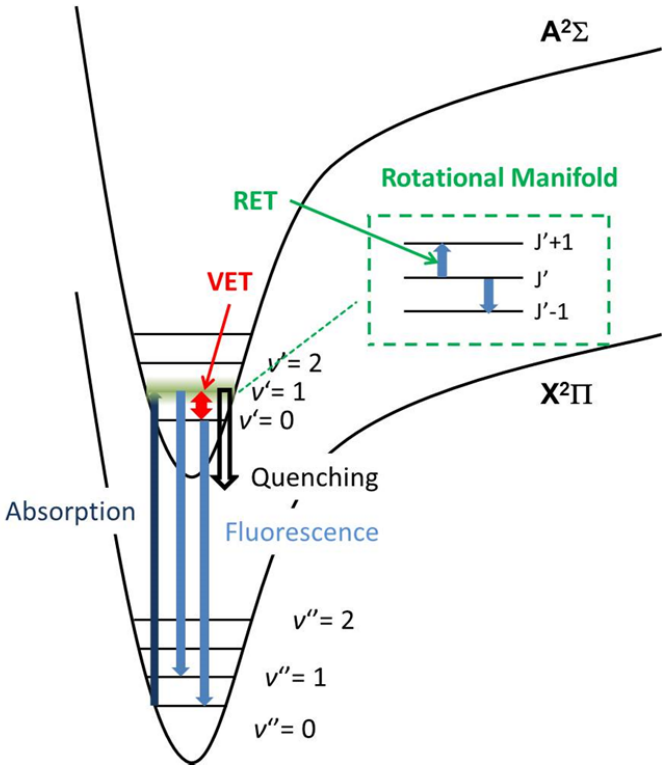

Figure A-1 Schematic diagram of energy transfer processes in the OH radical. Rotational manifold for the *v*'=1 vibrational level is magnified in the green dotted box.

Absorption and stimulated emission are excitation and de-excitation mechanisms directly coupled with the laser/molecule interaction. Population in the ground state is initially excited to an upper state through absorption of the incident photons. Simultaneously, stimulated emission by the laser induces a reverse, deactivation process which causes the excited molecules in the upper state to relax down to the ground state. The absorption rate, W_{12} (sec^{-1}) is linearly dependent on the Einstein B_{12} coefficient ($m^3/J \cdot s^2$) and can be represented as

$$W_{12} = \frac{B_{12} I_\nu}{c} \tag{A-1}$$

where I_ν is the incident laser irradiance per unit frequency interval (spectral irradiance in units of $W/cm^2 \cdot sec^{-1}$) and c is the speed of light. The stimulated emission rate W_{21} (sec^{-1}) is given in terms of the Einstein B_{21} coefficient ($m^3/J \cdot s^2$) as

$$W_{21} = \frac{B_{21} I_\nu}{c} \tag{A-2}$$

Absorption and stimulated emission are coupled by the Einstein coefficients, which are related to each other as

$$g_1 B_{12} = g_2 B_{21} \tag{A-3}$$

where g_1 and g_2 are the degeneracy of states 1 and 2, respectively.

OH radical is spontaneously relaxed from an excited upper state to other states i in the lower electronic state by emitting fluorescence. This radiative decay process constitutes the main mechanism for LIF signal production. The fluorescence rate is given by the

Einstein A_{21} coefficient (sec^{-1}), and the total fluorescence rate A is the sum of fluorescence rates over all individual transitions,

$$A = \sum_i A_{2i} \tag{A-4}$$

Spontaneous emission and stimulated emission are related by the Einstein coefficients,

$$\frac{A_{21}}{B_{21}} = 8\pi h\nu \tag{A-5}$$

where h is the Planck constant and ν is the wavenumber of the individual transition.

OH radical in specific rovibrational levels in the excited upper state can migrate to neighboring rotational or vibrational states by internal energy transfer processes during collision with other molecules. RET is typically very fast and particularly important in LIF dynamics of short pulse nanosecond lasers. As the laser pumps population from specific rotational levels in the ground electronic state to those in the excited upper state, thermal equilibrium is perturbed. RET is responsible for refilling (or depleting) the relevant energy levels in an effort to re-establish thermally equilibrated distributions. The rate of RET, Q_{RET}(sec^{-1}) induced by collisions with all other species j in the system is given by

$$Q_{RET} = \frac{p}{kT}\sum_j x_j \nu_j \sigma_j \tag{A-6}$$

where x and ν are the mole fraction of species j and elative velocity of the colliding particles ($\nu = \sqrt{8kT/\pi\mu}$ where μ is reduced mass, $\mu = m_1 m_2/(m_1 + m_2)$),

respectively. The parameter σ (cm^2) is the effective rotational cross section for collisions with species j. VET is conceptually identical to RET, but for the fact that energy transfer occurs to neighboring vibrational levels.

OH radical in the excited upper electronic state can relax down to a lower electronic energy state by collisions with other molecules. The overall rate of quenching Q_{21} (sec^{-1}) induced by collisions with all other species j in the system is usually given in the same way as RET,

$$Q = \frac{p}{kT}\sum_j x_j \nu_j \sigma_{Q,j} \qquad \text{(A-7)}$$

The term $\sigma_{Q,j}$ (cm^2) is the quenching cross sections upon collisions with the species j. RET and VET maintain the molecule in the upper electronic state, thereby retaining the possibility of fluorescence. On the other hand, quenching forces the molecule back down to the lower electronic state. Therefore, quenching directly competes with the LIF process. It also can be seen from Equation (A-7) that quenching is linearly dependent on pressure. Therefore, the impact of quenching becomes an important consideration particularly in high-pressure experiment.

In addition to the energy transfer processes described above, other mechanisms can play significant roles in the analysis of LIF. Absorption of additional photons for molecules in the excited upper state can result in photoionization of the molecule. Excitation of the molecule into a rovibrational level of a bonding state above the dissociation energy or onto a potential surface crossing to an anti-bonding state can also result in dissociation of

the molecule. This effect is known as pre-dissociation. Additional details regarding molecular energy levels and laser spectroscopy can be found in the literature [92, 93].

LIF Equation: Two-level derivation

A simple two energy level model is used to understand the basic physics of excitation and relaxation processes involved in LIF. The LIF equation, which captures the key physics involved in the LIF process, can be derived from a steady-state analysis of the two-level model. In theory, this type of simplified modeling is appropriate for atomic species and molecular systems with fully equilibrated rotational level manifolds. In practice, such models can be effectively used as a first approximation in actual LIF experiments. More complex models will be considered later. The basic transitions involved in the two-level model are shown in Figure A-2. Absorption and stimulated emission rates are shown using W_{12} and W_{21}, respectively. Quenching rates are shown as Q_{21}, and spontaneous emission rates are shown using A_{21}. The total number density is $n_T = n_1 + n_2$, where n_1 and n_2 represent the population number density of states 1 and 2, respectively.

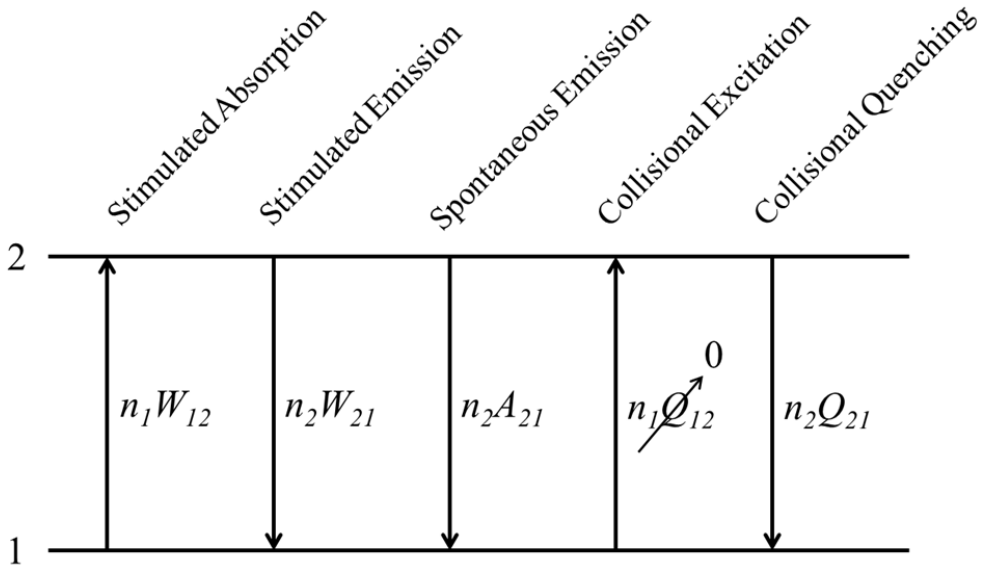

Figure A-2 Simple two energy level diagram for LIF model.

In a steady-state approach, we assume a constant laser intensity and therefore constant W_{12} and W_{21} (Eq. (A-1)) and W_{21} (Eq. (A-2)). Ignoring losses due to chemical reactions or pre-dissociation, rate analysis can be performed to determine the rate of change of the population of molecules in level 2 as

$$\frac{dn_2}{dt} = n_1 W_{12} - n_2(W_{21} + Q_{21} + A_{21}) \tag{A-8}$$

At steady-state, $dn_2/dt=0$, the population number density of states 2 can be represented as

$$n_{2,ss} = \frac{W_{12}}{W_{21} + Q_{21} + A_{21}} n_1 \tag{A-9}$$

Two limits of operation can be envisioned using this type of steady state analysis. When laser energies are sufficiently high ($I_\nu \gg I_\nu^{sat}$), absorption and stimulated emission balance and the population of the two energy states are determined by the ratio of the degeneracies in a two-level model: otherwise known as 'saturation'. In this limit, the fluorescence signal is independent of laser intensity. The other mode of operation is weak excitation ($I_\nu \ll I_\nu^{sat}$), which occurs when the laser energy is below saturation threshold. In this regime, the fluorescence signal is linearly proportional to laser intensity. Generally, this "linear LIF" is preferred since laser non-uniformities and attenuation effects pose practical problems in applying LIF in the saturated regime. When the induced emission from level 2 is much weaker than the sum of collisional and spontaneous decay processes, i.e.,

$$W_{21} = \frac{B_{21} I_\nu}{c} \ll Q_{21} + A_{21} \tag{A-10}$$

then $n_1 \gg n_2$, and $n_1^0 \approx n_1$. The population number density of state 2 in Eq. (A-9) can be written as,

$$n_2 = \frac{W_{12}}{Q_{21} + A_{21}} n_1^0 \tag{A-11}$$

As for a general description of the total LIF signal, it can be experimentally verified that the fluorescence signal is proportional to the population of level 2, the rate of spontaneous emission A_{21} and the solid angle of collection Ω. An expression for the fluorescence signal can be written as,

$$\text{LIF} = n_2 V A_{21} \frac{\Omega}{4\pi} \quad \text{(photon/sec)} \tag{A-12}$$

In actual practice, the fluorescence signal is mostly quantified by using LIF intensity, S_F (W/m^2). The population density of level 2 (n_2) also be replaced by a function of the initial ground state population (n_1^0) using Eq. (A-11). For more accurate modeling, we diverge from the strict concept of a two-level model and assume that the lower energy level has a manifold of rotational levels in thermal equilibrium. The population in these lower energy levels maintains a Boltzmann distribution and the population of a specific rotational level can be written as $n_1^0 \times f_B$, where f_B represents the Boltzmann fraction of the individual energy level. Based on these arguments and by using equations (A-2), (A-11) and (A-12), the LIF intensity can be written as

$$S_F = \varepsilon \times I_\nu \times n_1^0 \times f_B \times B_{21} \times V \times \Gamma \times \frac{\Omega}{4\pi} \times \frac{A_{21}}{A_{21} + Q_{21}} \tag{A-13}$$

where ε is the fluorescence collection efficiency, V is the volume of excited molecules, I_ν is the spectral intensity of the probing laser, and Γ is the dimensionless overlap function. The term A_{21} / (A_{21} + Q_{21}) in (A-13) is called the fluorescence quantum yield, Φ, which is the ratio of the spontaneous emission rate to all excited state de-excitation rates. It is a direct representation of how much of the excited population will actually fluoresce.

Cavity Ring-Down Spectroscopy (CRDS)

Cavity ring-down spectroscopy (CRDS) is a laser diagnostic technique used for quantitative analysis of gaseous samples. It was developed for the purpose of increasing the sensitivity of standard absorption methods, allowing a direct absorption measurement to be made for species that interact weakly with electromagnetic radiation [94]. The principle of CRDS is to increase the interaction path length of the laser beam with the sample being analyzed. This is accomplished by coupling the laser beam into a high finesse optical cavity composed of two highly-reflective dielectric mirrors, allowing the beam to be reflected through the sample hundreds to thousands of times (depending on the reflectivity of the mirror set), subsequently, increasing the interaction path length.

CRDS is capable of measuring sub-ppm (per pass fractional absorption) absorbers at visible and near-IR wavelengths and species absorbing on the 1 x 10^{-7} level in the infrared [95]. This high sensitivity combined with simple experimental and data quantification procedures has made CRDS the state-of-the-art absorption spectroscopic technique. This choice is particularly true for pulsed laser systems, where large pulse-to-pulse energy fluctuations negate the use of the traditional absorption technique of inferring a sample's transmittance by measuring the attenuation of a beam of light passed through that sample. Cavity ring-down primarily measures the exponential time constant (called the ring-down time) of a pulse of light injected into an optical cavity formed by two highly reflective mirrors (typically > 99.5%), and is therefore not dependent on the initial intensity of the light pulse. Reference [95] presented a review article describing the theory and advantages of the technique along with a survey of its successful applications.

Dielectric mirror sets used in CRDS experiments have a reflectivity ranging from 99.5% to 99.9995 %, depending on the desired wavelength range. CRDS mirrors are most often plano-concave with a specified radius of curvature, with the most commonly available ROC being, but not limited to, 1 and 6 m. Optical resonators constructed with mirrors that have a concave geometry reduce the effect of beam walk-off and improve the spatial resolution of the cavity.

Optical Emission Spectroscopy (OES)

In thermally non-equilibrium plasmas, because of their very nature, there are at least five temperatures T_{trans}, T_{rot}, T_{vib}, T_{elec}, T_e. These temperatures cannot be assumed to be equal nor can they be assumed the same from species to species. Even the often assumed conditions such as $T_{vib} = T_{elec} = T_e$ should not be assumed and in some cases have been directly shown to be incorrect [96]. The modeled spectra are sensitive to T_{rot}, T_{vib}, T_{elec} because the upper states of the emission transition have different electronic excitation energies, vibrational energy, and/or rotational energies. The population of the upper states is given by equation (A-14) [96] which assumes the internal energy levels follow Boltzmann distributions at T_{elec}, T_{vib}, and T_{rot} respectively, n is the population of the upper state (denoted by ') with a given electronic excitation (e), vibrational (v) and rotational (J) quantum level. g_e and $(2J+1)$ are the degeneracy (or statistical weighting) of the electronic excitation and rotational internal energy levels respectively, the vibrational level degeneracy is one. L is a line alteration factors due to nuclear spin and σ is 2 for homo-nuclear molecules and 1 for hetero-nuclear molecules, ε is the energy of the

respective level. The summation in the denominator represents the combined rotational, vibrational and electronic excitation partition function.

$$n_{e'v'J'} = n_{total}\frac{L}{\sigma}\frac{g_e(2J+1)\exp\left[-\frac{\varepsilon_{e'}}{T_{elec}}-\frac{\varepsilon_{v'}}{T_{vib}}-\frac{\varepsilon_{J'}}{T_{rot}}\right]}{\sum_{e,v,J} g_e(2J+1)\exp[-\frac{\varepsilon_e}{T_{elec}}-\frac{\varepsilon_v}{T_{vib}}-\frac{\varepsilon_J}{T_{rot}}]} \quad \text{(A-14)}$$

The term exp(-ε/T) in equation (A-14) represents the Boltzmann distribution. However, it is not always correct to assume that within a given internal energy mode the energy distribution function is Boltzmann. For rotational energy the assumption of a Boltzmann distribution with T_{rot} is accurate because the energy levels are closely spaced, and the characteristic temperature of the rotational energy mode is significantly less than the typical rotational temperature. For most species it can be assumed that the T_{rot} is close to T_{trans} and is effectively considered T_{gas} of the mixture because rotational-to-translational relaxation is fast at atmospheric pressure [96].

For vibrational and electronically excited states the temperature of the mode is on the order of the characteristic energy of the mode and assumption of a Boltzmann distribution can be inaccurate since the quantization of the states becomes important and the rates of specific paths of energy transfer from state-to-state need to be considered. The deviation from Boltzmann can occur in several ways. For example in certain vibrational systems Treanor distributions have been measured [3] due to preferential energy transfer to the higher vibrational states. A deviation from Boltzmann can also be due to the fact that OES only probes the states of electronically excited species. It is possible that the distribution functions are altered by the electronic excitation. For T_{rot} it

has been shown the rotational distribution of the upper state is sufficiently similar to that of the lower state to have equal temperatures even with small changes due to the excitation [97]. For the T_{vib} and T_{elec} collisional-radiative models attempt to take into account such processes but were not used in our modeling. Another complication is that in atmospheric pressure plasma the de-excitation time of the electronically excited states is non-negligible in comparison to the time between collisions. For N_2 C-B transitions the de-excitation time is a few tens of nanoseconds and at atmospheric pressure the time between collisions is about one ns. For these reasons it is only possible to speak of an apparent T_{vib} and T_{elec}. Although in practice when comparing the experimental rotational and vibrational line structure with Boltzmann computed distributions of the upper state there is fairly good superposition as shown later in Figure 4.17. In those cases the good superposition indicates that the Boltzmann assumption may be valid.

In summary these "temperatures" describe the relative population of different vibrational and rotational levels of C state of molecular nitrogen. Rotational distribution of C^3 state reflects the rotational population of ground state and gives information on the translational temperature of the gas. Vibrational spectra of second positive system cannot be directly associated with vibrational or translational temperatures of molecules. This distribution reflects interplay between the population by electron impact from different lower states and depopulation due to collisional quenching and radiative processes. Thus the vibrational distribution is a qualitative indicator for electron's temperature in the discharge region.

Vita

Liang Wu was born in Jiangxi Province, P. R. China, where he attended elementary, middle and high school. In the fall of 2001, Liang Wu enrolled at Tsinghua University in Beijing, China as an undergraduate student majoring in Electrical Engineering. Liang graduated from Tsinghua in 2005 with a Bachelor of Science degree.

In the fall of 2007, Liang Wu decided to come to the United States to pursue his graduate studies in mechanical engineering at Drexel University, where he received Provost Fellowship and Dean's Fellowship. He received his M.S. in September of 2009. He has co-authored 4 technical refereed papers (4 first-authors) and 15 additional conference papers in plasma assisted ignition and combustion while his study at Drexel. One of his conference papers in the 20th International Symposium on Plasma Chemistry (ISPC 20) entered as the finalist for the best student paper. After receiving his Ph.D. degree, Liang Wu plans to work in academia or industry, engaging in combustion or plasma research.